ARMA Letters

AMERICAN ROCK MECHANICS ASSOCIATION • FALL 2019 • ISSUE 28

In this issue

Editor's Note

Roughly a year ago we announced a new ARMA Letters initiative: a series of Special Issues, each dedicated to a subject of great interest to a large section of ARMA membership. The first proposal for a Special Issue came from one of the most active members of ARMA Publications Committee, Azra Tutuncu. Her suggestion was for a Special Issue on "The Role of Geomechanics in Unconventional Reservoir Characterization". Once the decision was made to accept her suggestion and designate her topic as the first one in the series, Azra undertook her responsibility with the enthusiasm for which she was known. She contacted potential contributors to the Special Issue, made sure that appropriate articles were submitted, provided her own introductory article and a co-authored an article with one of her associates.

Unfortunately, not everything went as planned. It is with great sadness and sorrow that I have to announce the untimely death of Azra Tutuncu just weeks before the Special Issue of ARMA Letters on Geomechanics and Unconventional Reservoirs saw the light of day. To honor Azra's contributions to ARMA and to the Publications Committee, and in particular to the present issue of ARMA Letters, we designate the issue "The Azra Tutuncu Volume".

Bezalel Haimson

The Contribution of Geomechanics to Unconventional Resource Development

Azra N. Tutuncu, Petroleum Engineering Department and Unconventional Natural Gas and Oil Institute (UNGI), Colorado School of Mines.

Significant amounts of hydrocarbons are locked in gas shale and tight oil formations. When a well is drilled in these reservoirs, the flow of hydrocarbons toward the wellbore is significantly limited, due to their nanopore scale complexities and their compatibility with the native fluids in the formation. This can result in uneconomical production unless selected advanced technologies such as hydraulic fracturing, re-fracturing, or Enhanced Oil Recovery (EOR) methods are implemented.

The first economically successful production from shale reservoirs was carried out by Mitchell Energy in 1998 through the coupled use of horizontal drilling and hydraulic fracturing in Barnett shale. This gave rise to the "unconventional revolution" in the U.S., transforming the country from an oil and gas importer to gradually becoming, in the past decade, a net exporter. The contribution of the tight unconventional formations to total crude oil production has grown rapidly from 2.5 MMbbl/d in 2012 (EIA 2014) to about 4.3 MMbbl/d in 2018 (EIA 2018). It is anticipated that the tight oil production will continue to increase, reaching 6 MMbbl/d in 2029 (EIA 2018). Geomechanics is one of the most essential disciplines contributing to the success of the unconventional reservoir development in the U.S. since it involves all aspects of operations from exploration to drilling, completions and production as well as many other interrelated topics including environmental protection and sustainable development.

The variation of stress and temperature during the maturation of shale gas reservoirs results in micro- and macro-fracturing. These natural fractures render the coupled geomechanics and fluid flow studies to be rather complicated and more challenging than similar studies in conventional reservoirs. Shale rock laminated structures give rise to unconventional reservoirs, and the properties of which should be incorporated in any design and reserve analysis (Al Qahtani and Tutuncu, 2017; Tutuncu and Bui, 2016; 2019).

The main differences between conventional and unconventional geomechanics involve the elasticity, the stress sensitivity in geomechanical, acoustic and transport properties, the permeability, the rock-fluid interactions, the natural fracture presence, and the anisotropy of mechanical characteristics. The interactions taking place between rock and fluid in conventional reservoirs are much less significant compared to the observed interactions taking place in unconventional reservoirs. The relatively larger pore sizes and higher permeability of conventional reservoirs allow the fluid to move in or out of the pore space, quickly reaching a steady state when stress changes. On the other hand, the movement of the fluid in the pore space is at much lower velocity in unconventional reservoirs because of low permeability, resulting in transient interactions in addition to strong stress dependence of the transport and storage properties (Bui and Tutuncu, 2015; Tutuncu et al., 2016). Moreover, high surface energy of the shale complicates the interactions taking place between rock and fluid, increasing the role of fluid electrochemical properties in shale deformation, and further enhancing the role of geomechanics in many aspects of shale development projects

Due to the presence of micro-fractures and bedding lamination, shale mechanical properties may significantly be altered as a function of bedding direction. The mechanical properties of shales are often anisotropic and experimental results indicate this anisotropy can be simplified as transversely anisotropic. The distribution of clay and organic matter in shale reservoirs also impacts the level of elastic anisotropy. The kerogen maturity and bedding orientation are among the key parameters controlling shale's mechanical anisotropy. In addition, the stress and fluid sensitivity of shale formations have been well recognized since the early days of conventional reservoir development as a key data for wellbore integrity analysis.

The presence of natural micro- and macro-fractures makes the study of geomechanics for unconventional reservoirs more challenging. The hydraulic fracture propagation path is highly affected by the interactions between the natural fractures and hydraulic fractures, fracturing fluid, and proppant and fluid selection. Local anisotropic rock properties, reservoir mineralogy, and natural fractures are the key parameters determining fluid transport and proppant

placement, associated in situ stress alterations during fracturing process, and production in unconventional tight oil and shale gas reservoirs.

Conventional and unconventional geomechanical approaches have greatly contributed to the success of the unconventional resource developments. Geomechanical data and models are indispensable in unconventional reservoir projects. They have been used intensively in all aspects of formation characterization, well construction, completions, hydraulic fracturing and reservoir modelling, in addition to environmental assessment and social responsibility. In reservoir characterization, mechanical anisotropy, natural fractures, and in-situ stresses are extensively investigated in the literature. In addition to natural fractures, bedding characteristics, the inelastic and anisotropic mechanical properties of shale, the coupled transport and rock-fluid interactions have received more attention in well construction.

The focus of geomechanics in well stimulation, particularly hydraulic fracturing, is on optimizing the wellbore and hydraulic fracture spacing, as well as the long term behavior of proppant and fracture interaction. In reservoir modeling and management, multiple coupled modeling and integration of seismic data into reservoir simulation are active areas of research with the focus on simplified approaches to reduce the computational cost and time, as well as allow better selection of EOR technologies for customized applications (Bui and Tutuncu, 2019).

The physical phenomena that have profound effects on unconventional reservoir production such as capillary condensation and fluid-rock interaction are also important to understanding how the mechanical aspect at nano-scale can affect reservoir long-term performance. In addition, predicting micro-seismic events such as induced earthquakes are an important contribution of geomechanics to environmental protection and sustainability development.

In this Special Issue of ARMA Letters, we focus on the unique aspects of Unconventional Reservoirs and emphasize the role of geomechanics in unconventional resource development.

References

Al-Qahtani A.A. and Tutuncu A.N. 2017. Qualitative and Quantitative Impact of Thin Rock Lamination on Acoustic and Geomechanical Properties of Organic-Rich Shale, SPE-183806, Proc. SPE Middle East Oil & Gas Show and Conference, Manama, Bahrain.

Bui B.T. and Tutuncu A.N., 2019, A Multi-Physics Model for Water Injection Improve Oil Recovery in Liquid-Rich Shale Formations, ARMA 2092, Proc. 53rd US Rock Mechanics/Geomechanics Symposium.

Bui B.T. and Tutuncu A. N., 2018 a, Modeling the Swelling of Shale Matrix in Unconventional Reservoirs. Journal of Petroleum Science and Engineering, 165: 596–615.

Bui B.T. and Tutuncu A.N. 2018 b. A Coupled Geomechanical and Flow Model for Evaluating the Impact of Drilling Fluid Imbibition in Reservoir Shale Formations. ARMA-2018-075, Proc. 52nd U.S. Rock Mechanics/ Geomechanics Symposium, Seattle, Washington, USA.

Bui B.T. and Tutuncu A. N., 2015, Effect of Capillary Condensation on Geomechanical and Acoustic Properties of Shale Formations. Journal of Natural Gas Science and Engineering, 26: 1213-1221.

EIA. 2014. Annual Energy Outlook 2014 with Projections to 2040. Technical report, U.S. Energy Information Administration.

EIA. 2018. Annual Energy Outlook 2019 with Projections to 2050. Technical report, U.S. Energy Information Administration.

Tutuncu A.N. and Bui B.T. 2019. A Comparative Study of Organic Richness and Maturity Impact on Anisotropic Geomechanical Properties in Shale Reservoirs, URTEC-19-428 Proc. Unconventional Resources Technology Conference, Denver, Colorado, USA.

Tutuncu Tutuncu A.N., Katsuki D., Bui B., Padin A. and McDowell B. 2016. Coupling Geomechanics and Petrophysical Measurements for Production Enhancement in Organic-Rich Shales. Paper SPE-2461986, Proc. Unconventional Resources Technology Conference, San Antonio, Texas, USA.

Tutuncu A.N. 2010. Anisotropy, Compaction and Dispersion Characteristics of Reservoir and Seal Shales. ARMA-10-344, Proc. 44th US Rock Mechanics/Geomechanics Symposium and 5th U.S.-Canada Rock Mechanics Symposium, Salt Lake City, Utah, USA.

Geomechanics in Unconventional Reservoir Stimulation: Brittleness, Stimulation Mechanisms, Hydraulic Fracture Clusters, and "Frac Hits"

Submitted by Ghassemi A., Hu L., Li Y., Kumar D., Sesetty V., Ye Z.; Reservoir Geomechanics & Seismicity Research Group, University of Oklahoma.

1. Introduction

Unconventional petroleum and geothermal reservoirs have ultra-low permeability and heterogeneous geomechanical characteristics that pose challenges to economic petroleum production. For example, in the case of gas shale, fracture conductivities of 10 mD/ft. or higher appear to be necessary for economic gas production (Roberto-Suarez and Ghassemi, 2014). For EGS permeability and surface area should be sufficiently high to yield over 50kg/ sec of water at temperatures higher than 150 C. Such a production rate requires a highly permeable fracture network with sufficient surface area. Economic production in nano-Darcy permeability reservoirs relies on creating a fracture network by stimulation via hydraulic fracturing, preferably without excessive demand on water, chemical additives, and proppants, and without the risk of felt seismicity. This is often achieved by multiple hydraulic fracturing. But hydraulic fracturing results are often poorly predictable, in part because of the resulting complex fracture geometry that arises from intact rock and rock mass textural characteristics and the in-situ stress. This complexity not only impacts permeability enhancement but also the containment of the stimulated volume within the zone of interest (with significant environmental consequences). At times simple variations in depth interval appear to yield completely different fracturing styles, resulting in different stimulation outcome and containment response. This phenomenon is often attributed to in-situ stress contrast heterogeneity or rock brittleness, shear reactivation of mineralized fractures, and textural variations.

Geomechanics is key to a number of technical challenges in well completion and stimulation design, including cluster spacing, heal bias, high net pressure, fracture complexity and the likelihood of the occurrence of fracture cluster. The nature of the simulated volume, and the role of mixed-mode fracture propagation and hydraulic fracture/natural fracture interaction, seismic/aseismic slip and permeability enhancement, multi-segmented fractures, and poroelastic effects in re-fracturing and hydraulic fracture interference is key. In this paper we describe the results of advanced geomechanical modeling and laboratory experiments to shed light on a number of these issues.

2. Stimulation Process and Conceptual Models and Issues

There have been different conceptual models proposed and implemented for enhancing reservoir permeability via creation of a fracture network -- namely multiple, somewhat planar hydraulic fractures from horizontal wells, and/or shear stimulation of natural fractures. The latter is based on the knowledge that in shear, the fractures dilate and become more permeable as the rough fracture surfaces tend to self-prop. Many hydraulic fracturing jobs have shown shear failure to be the main source of permeability enhancement, particularly where natural fractures are pervasive. In the Barnett shale, for example, micro-seismic events caused by shear-slip have been observed over a large region (Rutledge and Phillips, 2002). It has been suggested that increased viscosity promotes tensile failure and can lower complexity (Cipolla et al. 2008) and in water fracture treatments shear failure is anticipated to dominate (Chipperfield, S.T., Wong, J.R., Warner, D.S. et al. 2007). In fact, some shale fracture jobs have been completed without proppants with surprisingly good results. The results are reminiscent of field experiences in some tight gas sand reservoirs (Rutledge and Phillips, 2002; Mayerhofer et al. 1997) that led to the concept self-propping water fracs with minimal proppant use (7-10% of the usual amount). However, laboratory experiments, modeling and analysis (Min et al., 2010; Jung, 2012; Kamali and Ghassemi, 2017; Zhi and Ghassemi, 2016; 2018) as well as field data (Cornet et al., 2007) have shown that stimulation by shear slip may not be limited to the dilation effect and that slip can cause propagation of natural fractures to form tensile wing cracks and/or shear cracks.

A critical matter in optimizing reservoir stimulation either by multi-stage fracturing or by the shear stimulation concept (or a combination thereof) is knowing how multiple fractures form and interact, how the permeability of the fractures changes with slip, and how the resulting conductivity evolves as the stresses (shear and normal) on the fractures change during production.

Additionally, stimulation of ultra-low permeability reservoirs is often accompanied by micro-seis-

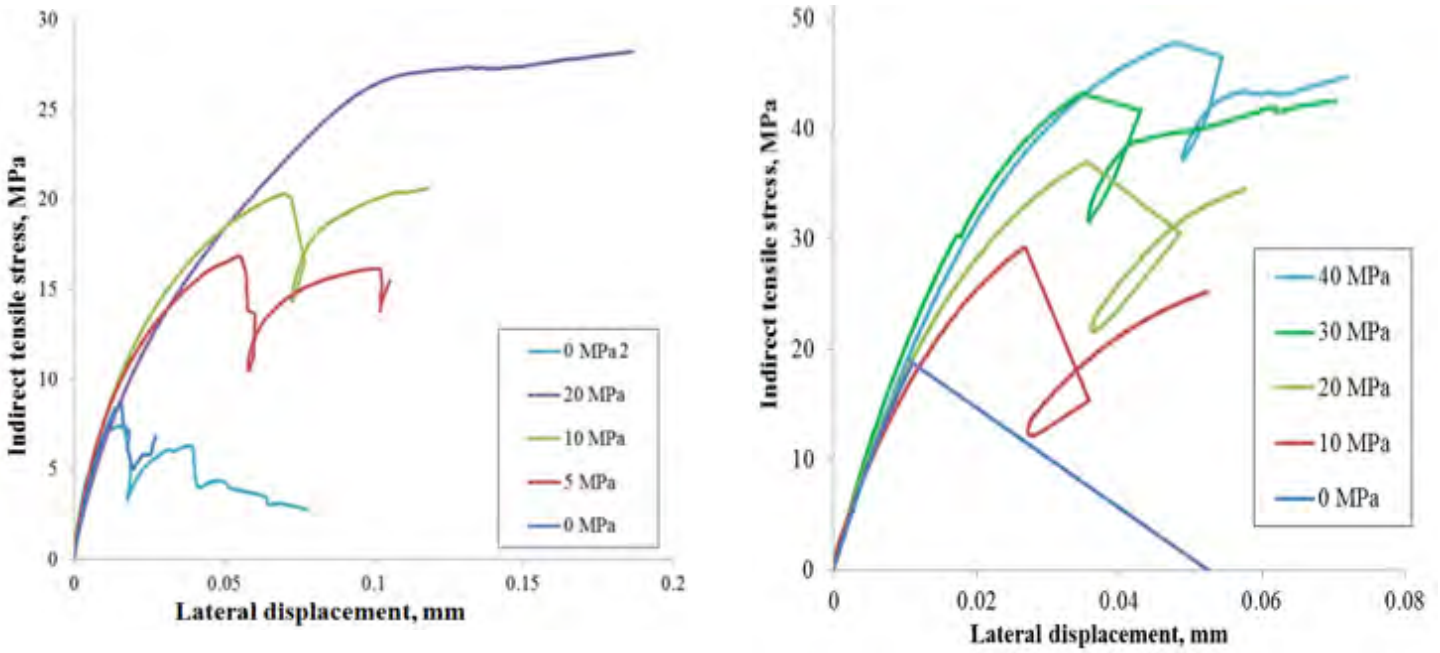

Figure 1. Stress-lateral displacement curves for Barnett shale (left) in the confined Brazilian test. Stress-lateral displacement curves for Eagle Ford shale (right) in the confined Brazilian test.

micity. The micro-seismic signals associated with stimulation by water injection contain information about the sources of energy that can be used for understanding the hydraulic fracturing process (e.g., Foulger et al., 2006; Warpinski, et al., 1997) and the created reservoir properties. Detection and interpretation of microseismic events is useful for seismicity-based reservoir characterization that aims to estimate the stimulated volume, created reservoir permeability and fracture growth (Lu and Ghassemi, 2018; Warpinski et al., 2001). Maximizing facture permeability generation and retention and minimizing risk of seismicity, understanding how seismicity distribution is related to injection rate and volume, how shear stimulation enhances fracture permeability, and how the unpropped fractures in the network evolve with production are key components of optimum stimulation design that can minimize costs and the environmental foot-print, including induced seismicity. Particularly, for geothermal reservoirs, maximizing facture permeability generation and retention and minimizing risk of seismicity is a highly desirable goal. This can be better achieved if the seismic response of the formation to fluid injection and the contribution of rock failure and fracture to network permeability can be reasonably quantified. Geomechanical concepts, experiments, modeling, and analyses are critical to reaching this objective. The focus of this paper is unconventional petroleum resource development; however, many of the concepts are directly applicable to enhanced geothermal systems (EGS).

3. Rock Brittleness

Rock brittleness is a parameter often used to delineate favorable stimulation zones in unconventional petroleum reservoirs. There are many brittleness definitions with different measurement methodologies proposed in the literature. Andreev (1995), Jin (2015), Rybacki (2016) and Zhang (2016) have reviewed various rock brittleness definitions in the literature. Often, a certain index is used for a given application because of its relevance. An inherent problem with some proposed brittleness measures is their empirical nature and inability to follow the expected trend when varying parameters such as the confining pressure. Furthermore, many indices are derived from compression tests while subsurface hydraulic fractures are tensile events at high confining pressure. Although it has been suggested that shear failure under compression is inherently tensile at the micro-level (Horii and Nemat-Nasser, 1985; Petit and Barquins, 1988), nevertheless, brittleness indices derived from compression test may not be representative so that brittleness evaluation in tensile mode is more appealing. Recently, Li and Ghassemi (2017) have proposed a new approach for brittleness evaluation, which is based on a damage-controlled Brazilian test. The experimental data show that the crack opening displacement (COD/lateral displacement) can be used as a brittleness index. The authors carried out damage-controlled (lateral displacement control) Brazilian tests on a number of shale rocks such as Eagle Ford shale, Marcellus shale, and Barnett shale. The shale samples were cored perpendicular to bedding.

(a)

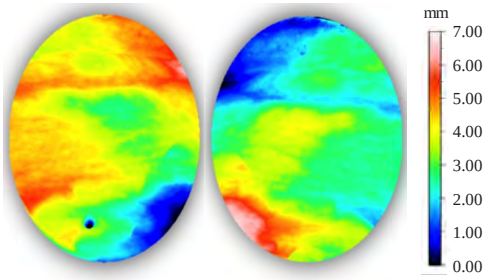

(b)

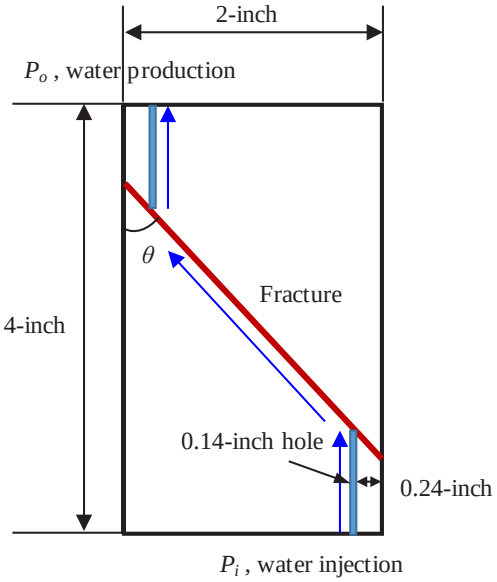

(c)

Figure 2. Sample set up and fluid flow path: (a) the natural Eagle Ford shale fracture, (b) fracture surface characterization (maximum surface relief is ~7 mm, and JRC=12.35), (c) sketch of fluid flow during injection.

The experimental results show the failure of Eagle Ford and Marcellus shale discs to be characterized by a sudden increase of lateral displacement at failure; this is manifested by the straight post-peak line and sudden unloading and reloading cycle, which is a characteristic of brittle response. This sudden failure even occurred at 40 MPa confining pressure (Figure 1).

The failure behavior of Barnett discs is relatively more ductile; there is no sudden increase of lateral displacement at failure. Inspection of Barnett discs reveals that the failure of discs is due to splitting along bedding plane and plastic deformation at the contact point. There are no extension cracks along σ_1 direction at the center of the discs; this is due to the strong ductile and anisotropic nature of tested Barnett discs. The mineralogical content of the three shale samples correlates well with their stress-displacement curves. The more quartz and calcite a sample contains, the more brittle it is. The results show that the proposed technique based on damage-controlled Brazilian test, and the use of the Crack Opening Displacement (COD) can be used as an objective measure of brittleness.

4. Shear Stimulation and Permeability Increase

Shear slip on natural fractures and bedding planes resulting from increased pore pressure by fluid injection has long been recognized to occur during reservoir stimulation, contributing to permeability increase. The reactivation of critical or near critical pre-existing fractures causes them to slip and dilate and perhaps further propagate to generate a conductive fracture network at treatment pressures below minimum principal stress. However, the fundamental mechanisms have not been studied under reservoir conditions and their contributions to permeability increase are not well understood. In this paper some experimental results are presented to shed light on the issues. Both injection-induced fracture slip and fracture propagation are studied under triaxial conditions.

4.1 Injection-induced shear test on shale

An injection-induced shear test was conducted on a 2-inch diameter and 4-inch long core plug containing a single natural fracture. Two 0.14-inch diameter boreholes were drilled from each sample end to touch the fracture and to form a flow path (Figure 2). During the test, a 30 MPa (4350 psi) confining pressure was initially applied on the sample, and the production pressure in top borehole was set to constant as 5 MPa (725 psi). The initial injection pressure was set to 5 MPa (725 psi). After increasing the differential stress to a near-critical level (70 MPa/10150 psi), the test was switched to a constant displacement control mode. Next, the injection pressure was increased in steps at a rate of 0.03 MPa/s (5 psi/s) to induce fracture slip. After each step, salt water (7% KCL) was circulated from the bottom borehole to the top borehole through the fracture and the steady-

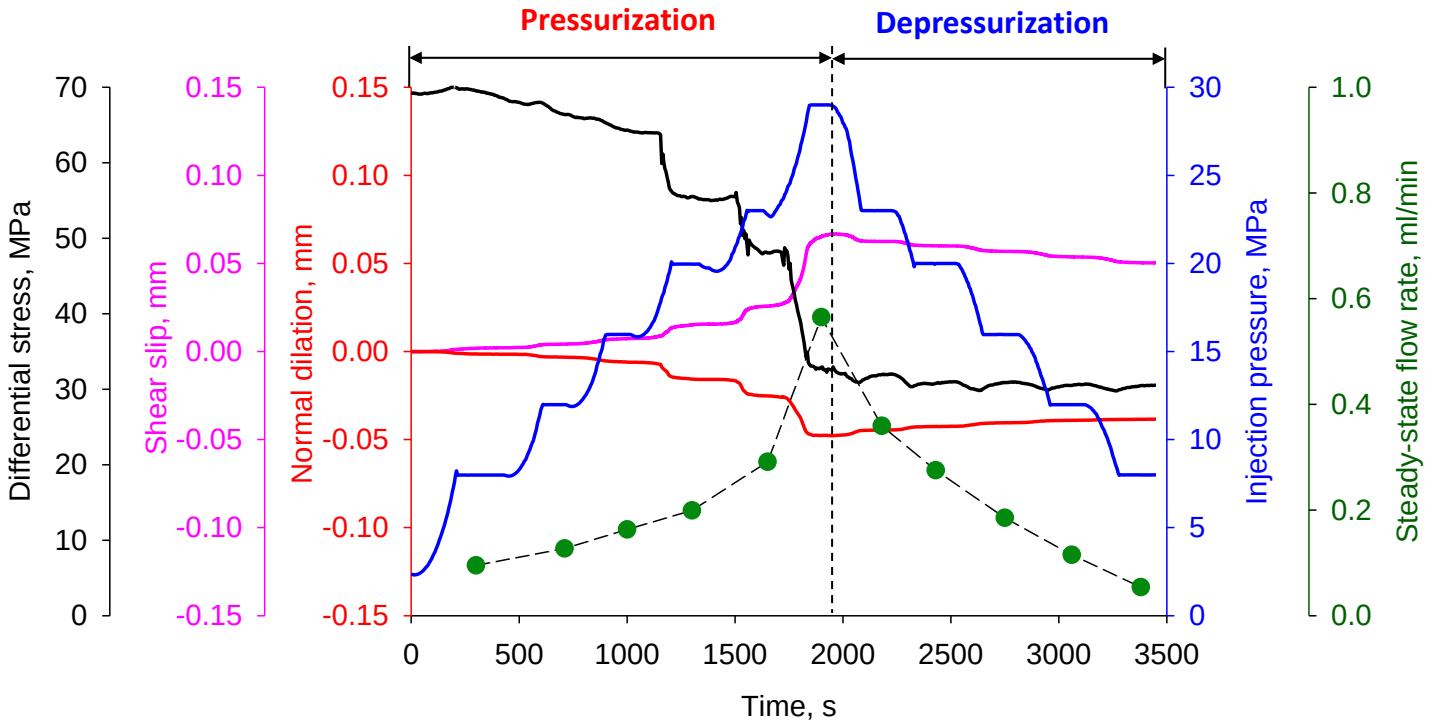

Figure 3. The temporal evolution of the differential stress (black), the shear slip (pink), the normal dilation (red, the negative values indicate dilation under rock mechanics sign convention), the injection pressure (blue) and the steady-state flow rate (dark-green dot) during the injection-induced slip test on an Eagle Ford shale fracture.

state flow rate in fracture was measured. To ascertain if the permeability increase would be retained after the fracture slip, the injection pressure was lowered in steps after the shear slip at a rate of -0.03 MPa/s (-5 psi/s) with the circulation procedure repeated.

The hydro-mechanical measurements of the fracture slip test are shown in Figure 3. The injection pressure, the differential stress, the shear slip and normal dilation (on the fracture plan) all gradually change during the pressurization-depressurization of water injection. The flow rate at each steady-state regime, achieved by injection pressure hold, was measured to investigate permeability evolution. In the pressurization stage, the pressure curve shows that in the last pressure build-up stage (from 23 MPa to 29 MPa), a sudden shear slip was induced along with a large differential stress drop and flow rate increase. The flow rate was enhanced 6 times to 0.565 ml/min from the base flow rate of 0.095 ml/min. Only relatively small fracture sliding and dilation (both are less than 0.1 mm or 0.004-inch) were induced on the fracture plane. The average sliding rate was around 3×10-7 m/s (1.18×10-5 inch/s). The differential stress dropped from 70 MPa to 30 MPa during slip, capturing the similar phenomenon of stress relaxation during shear slip on real faults and fractures. In the depressurization stage, a permeability hysteresis is observed (Figure 4). As can be seen, the enhancement of flow rate caused by fracture shearing

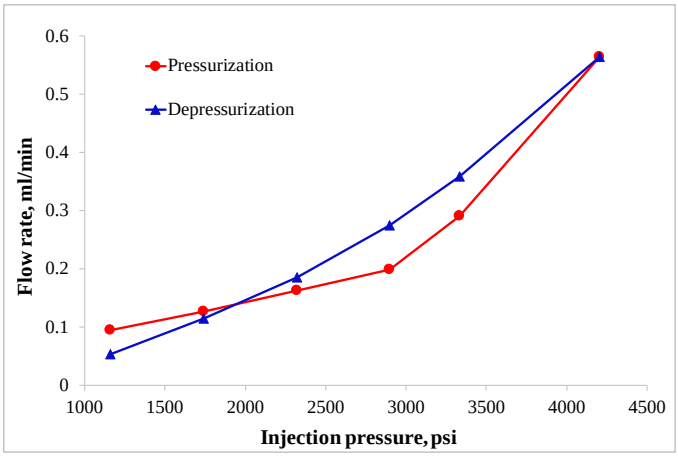

Figure 4. Flow rate/permeability hysteresis under pressurization-depressurization path of injection pressure.

is retained until the injection pressure drops to 16 MPa where the flow rate becomes even smaller than during the pressurization stage. This is likely related to the high effective compression under low fluid pressure conditions and the gauge produced during fracture sliding.

4.2 Fracture network generation by slip on discontinuities

The generation of new cracks can be an integral part of shear stimulation mechanism as shear slip increases the stress-intensity at the fracture tips, potentially leading to fracture propagation. Until recently, aside from modeling, this process had not been clearly

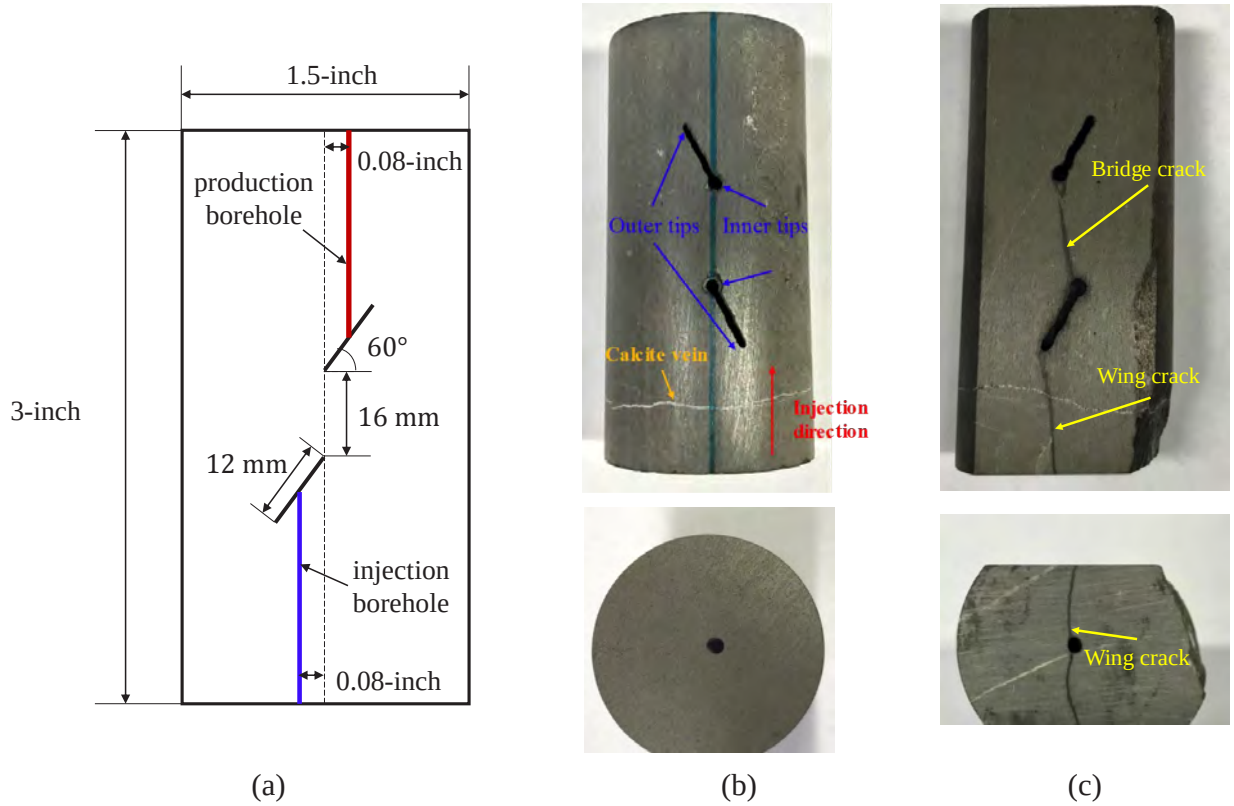

Figure 5. (a) The geometry of the sample and the pre-existing flaws, (b) the double-flawed Eagle Ford shale sample before testing, (c) induced cracks on the sample after the injection test.

demonstrated in laboratory-scale experiments. To our knowledge, no experiments have been completed that directly induce fracture propagation and coalescence by injection at pressures below the confining pressure under triaxial stress conditions. In a recent novel experimental study injection-induced fracture propagation tests have been conducted on shale and granite samples (Ye and Ghassemi, 2018; 2019). A test on Eagle Ford shale sample (1.5-inch diameter by 3-inch length) containing two pre-existing flaws is described here. The geometry of the cylindrical sample with a pair of pre-existing flaws is shown in Figure 5(a). The two flaws have an inclination angle of 60° with respect to the short axis of the sample, and are 12 mm (0.47-inch) long. The saw-cut flaws are about 1.4 mm (0.05-inch) wide. It is observed that each pre-existing flaw has one keyhole caused by the drill bit (Figure 5(b)). For injection and production during the test, two boreholes with 2 mm (0.08-inch) diameter are drilled from the two sample ends to meet the upper flaw and the lower flaw, respectively. The boreholes are situated 2 mm (0.08-inch) from the central axis of the sample (Details of the test conditions can be found in Ye and Ghassemi (2019).

The hydro-mechanical responses during the fracture propagation test are shown in Figure 6. For the most part of the 1st pressurization stage (0 to ~140 seconds), the injection flow rate stably oscillates with the elevation of injection pressure, since the injection pump was in a pressure control mode. A slight decrease of differential stress and a small increase of the radial displacements were observed. This means that macro-cracks were not propagate yet, but the micro-cracks nucleation around the tips of the pre-existing flaws may have occurred. Near the end of the 1st stage and the early part of the 2nd stage (~130 to ~240 seconds), both axial and radial displacements as well as the differential stress displayed significant changes. This corresponds to the propagation of the micro-cracks. However, the lower flaw and the upper flaw did not coalesce as indicated by zero production from pump B. The latter part of the 2nd stage (240 to 340 seconds) reflected fracture coalescence where the flow rate of the pump B shows a continuous increase, and much larger deformations and stress drops are observed.

In this part, the two pre-existing flaws have coalesced through the induced crack(s) allowing the injected water to flow from the lower flaw to the upper flaw. At the end of this stage, the production flow rate was identical to the injection flow rate, indicating that the dominant flow path/fracture network connecting the lower and upper flows has been created and all injected water was produced by the upper flow. In the

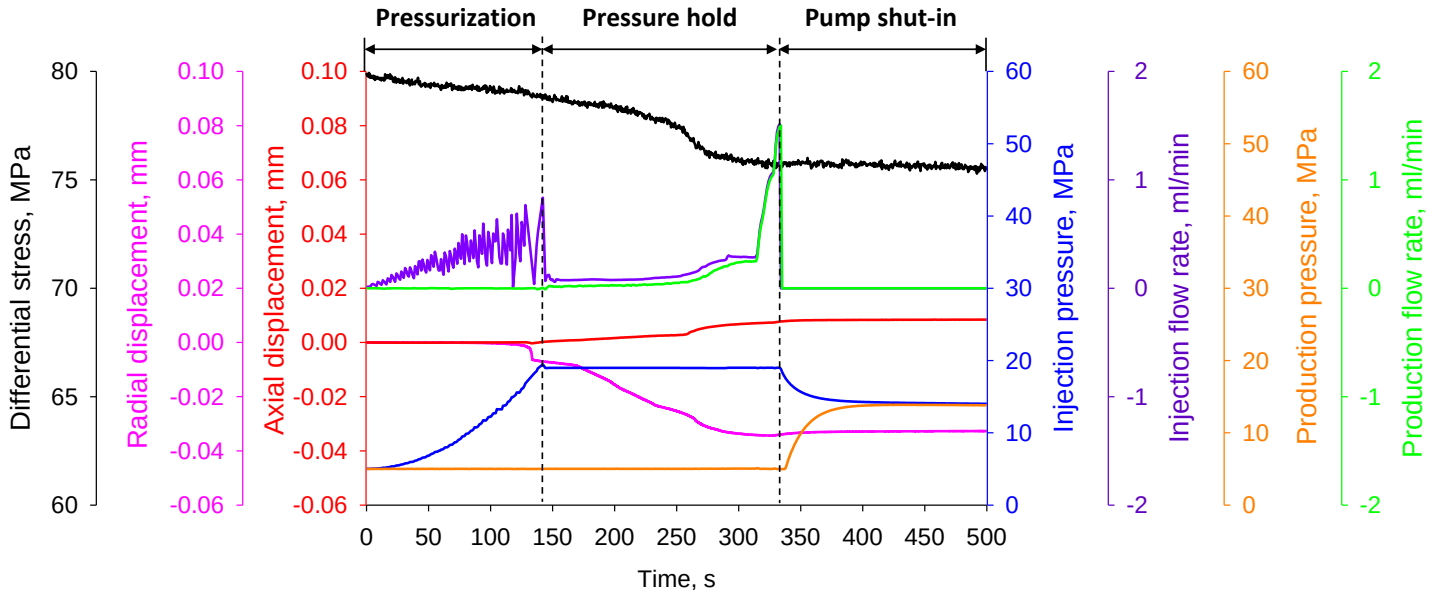

Figure 6. The temporal evolution of the differential stress (black), the radial displacement (pink), the axial displacement (red), the injection pressure (blue), the injection flow rate (purple), the production pressure (orange) and the production flow rate (green) during the injection-induced fracture propagation and coalescence test on an Eagle Ford shale sample.

3rd stage (340 to 500 seconds), the two pumps were shut-down so the pressure in the upper flaw gradually increased while the pressure in the lower flaw continually decreased until both approached the same value. As shown in Figure 5(c), a pair of wing cracks have emanated from the two tips of the lower flaw. The wing crack initiated from the inner tip of the lower flaw propagated upward and connected with the inner tip of the upper flaw, and then a conductive fracture network was generated to produce water from the top of the sample. It is also noticed that the lower wing crack intersected with the injection hole at the bottom end of the sample, indicating this wing crack may occur with a planar shape.

The important question addressed in this test was the possibility of flow enhancement due to the fracture network generation at pressures below the minimum in-situ stress. The test results show the production flow rate in pump A was zero before the coalescence of the two pre-existing flaws but increased significantly once the propagation and coalescence of the flaws formed a connected network. Thus, in addition to dilatant shear slip, propagation and coalescence of pre-existing fractures can significantly contribute to permeability creation during low pressure injection into fractured rocks or when fluid leaks-off into the rock from a main hydraulic fracture. The formation of tensile or shear cracks from natural fracture tips in response to pressurization can explain the observation of non-double-couple events in microseismic studies of injection (Julian, et al., 2007; Julian, et al., 1998; Miller et al., 1998; Staněk & Eisner, 2017).

4.3 Slip on discontinuities by a hydraulic fracture

Many investigations have studied the interaction between a natural fracture and a hydraulic fracture to better understand the potential for crossing and arrest of the hydraulic fracture. However, discontinuity slip caused by an approaching hydraulic fracture has not received much attention aside from a few modeling studies (Koshelev and Ghassemi, 2003; Dobroskok and Ghassemi 2004). It was shown for a given stress condition, the discontinuity inclination and frictional characteristics -- as well as the conditions on the fracture surfaces -- are the most significant factors that influence the trajectories of an approaching hydraulic fracture. Recent investigations of Moment Tensor Inversion (MTI) of microseismic data recorded during hydraulic fracturing (Kahn et al., 2017) show a large number of events to have moment tensors consistent with either vertical or bedding plane slip. Hu et al. (2019) have endeavored to assess the occurrence of bedding plane slip events using analog experiments on the mechanical interaction between a hydraulic fracture near a discontinuity under triaxial stress and hydraulic fracturing conditions. Analysis of the data clearly shows the occurrence of slip on the joint in response to the approaching hydraulic fracture. Expectedly, the degree of shear slip varies with natural fracture dip, and friction angle. The slip is accompanies by a stress drop and increased AE activity.

The tested samples were 101.6 mm (4.0 in) in diameter, 152.4 mm (6 in) long cylinders (Figure 7) with a polished, inclined saw-cut joint (PMMA, granite, and

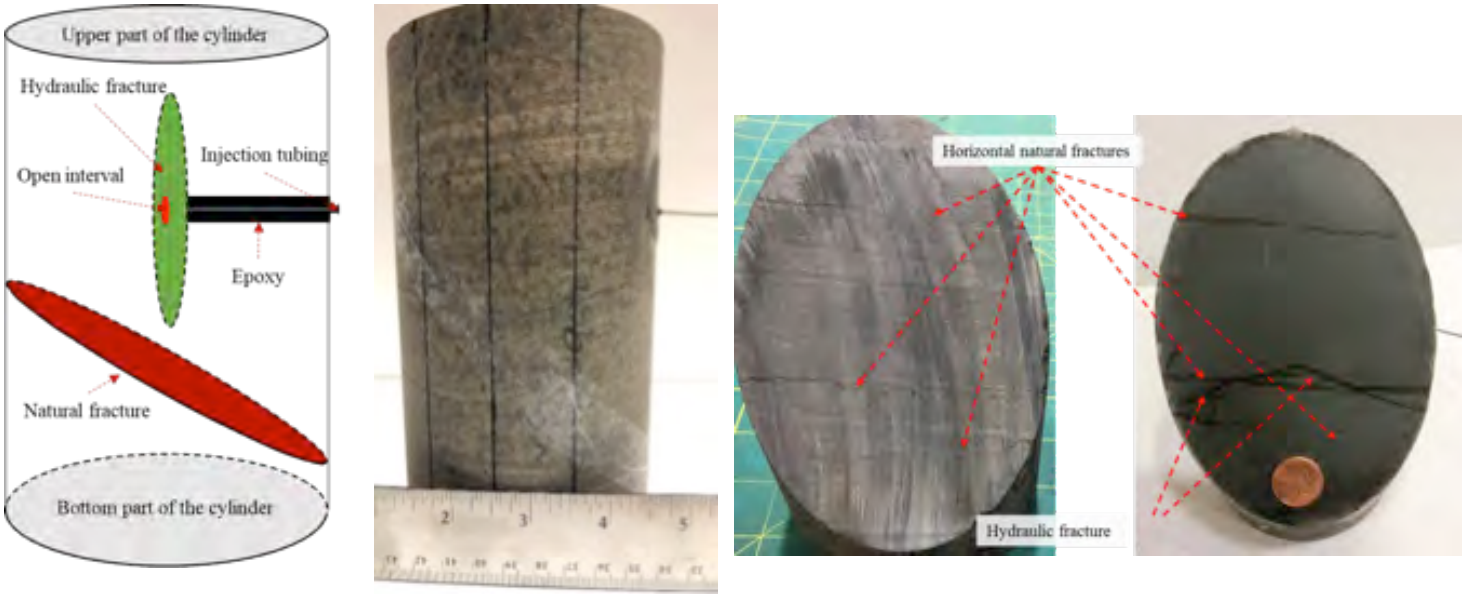

Figure 7. Schematic of the sample layout; (left), tested shale cylinder with a smooth joint (middle) before the test. On the right: the hydraulic fracture intersected the joint; also visible is the intersection and crossing of bedding planes by the hydraulic fracture.

shale specimens were tested but only the latter is reported herein). The shale sample had a 45° smooth saw-cut joint serving as a proxy for a natural fracture. Strain gauges were glued across the joint and on the upper part of the cylinder across the potential hydraulic fracture trace.

Before the test, a constant confining pressure of 3.4 MPa (500 psi) and a constant deviatoric stress of 2.1 MPa (303 psi) were applied to bring the system to a near critical condition (the friction angle of the smooth joint is around 14.8 degrees). During fracturing, a constant injection rate of 1.5 ml/min was employed. The recorded stress, injection pressure, AE activity, calculated slippage and the fracture opening are plotted in Figures 8 and 9. The test record is divided into six stages. During Stage 1 is before fracturing with nearly constant deviatoric stress and displacement. Stage 2 corresponds to fracture initiation and stable propagation. The hydraulic fracture propagated a small distance from the notch at the wellbore. Even though the hydraulic fracture has not reached the joint, the displacements show an increase with a larger value for the displacement across the joint (slip) accompanied by a stress drop of 0.14 MPa (20 psi). The horizontal deformation (across the potential hydraulic fracture trace) of the cylinder remained small in Stage 2. In Stage 3, the hydraulic fracture propagated to reach the joint while still being contained in the sample's top piece, causing both displacements to show a large increase. The stress dropped to a stable level at the end of Stage 3, so sliding stopped in Stage 4. The fracture reached the sample's top piece half-way through the Stage 4 with the horizontal deformation reaching its maximum and remaining nearly constant. More slippage is observed in Stage 5 in response to the pore pressure increase in the joint by the inflow of oil lowering the effective stress on the joint. During Stage 6 (injection termination), no further stress drop was recorded as the joint stress condition dropped to a stable condition during the previous stage.

In this test on shale, the slippage on the joint surface was about 0.11 mm with a stress drop of about 0.6 MPa before the hydraulic fracture reached the joint (close to the end of Stage 3). Also, as can be seen in Figure 8 and 9, the slip across the joint also caused increase in AE activities. The test results clearly illustrated the deformation and slip of a natural fracture or bedding plane by an approaching hydraulic fracture as suggested by moment tensor inversion of the field data (Kahn et al., 2017) and illustrated in the numerical study of Koshelev and Ghassemi (2003).

5. Modeling and Analysis of HF/NF Interaction and Network Complexity

As discussed above, shear displacement of natural fractures caused by induced stresses and pore pressure changes contributed to reservoir permeability. As a result, complex fracture modeling is useful for better estimating of the stimulated volume and to identify sweet spots to maximize productivity from unconventional naturally fractured reservoirs. However, current large scale hydraulic fracture models are either inherently incapable of handling complex hydraulic fracture and natural fracture interactions

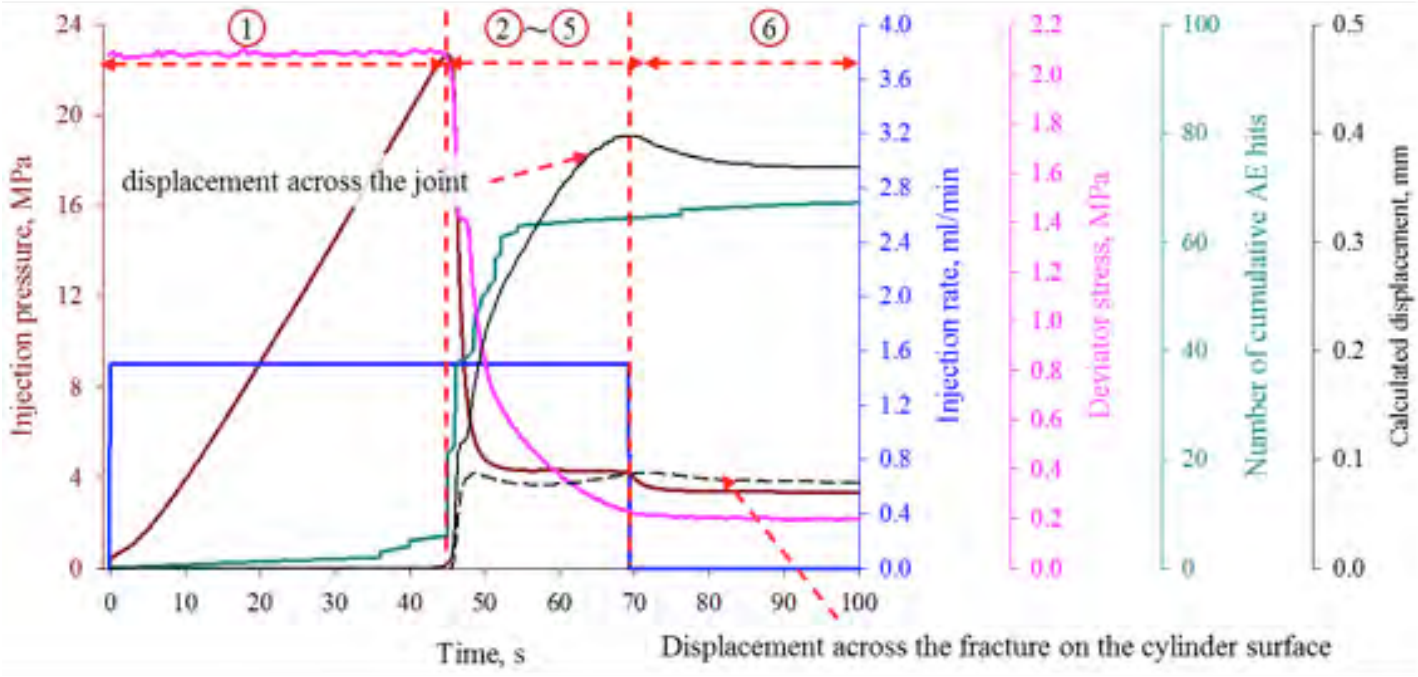

Figure 8. Recorded data during the test: AE activity jump and displacement jump was observed.

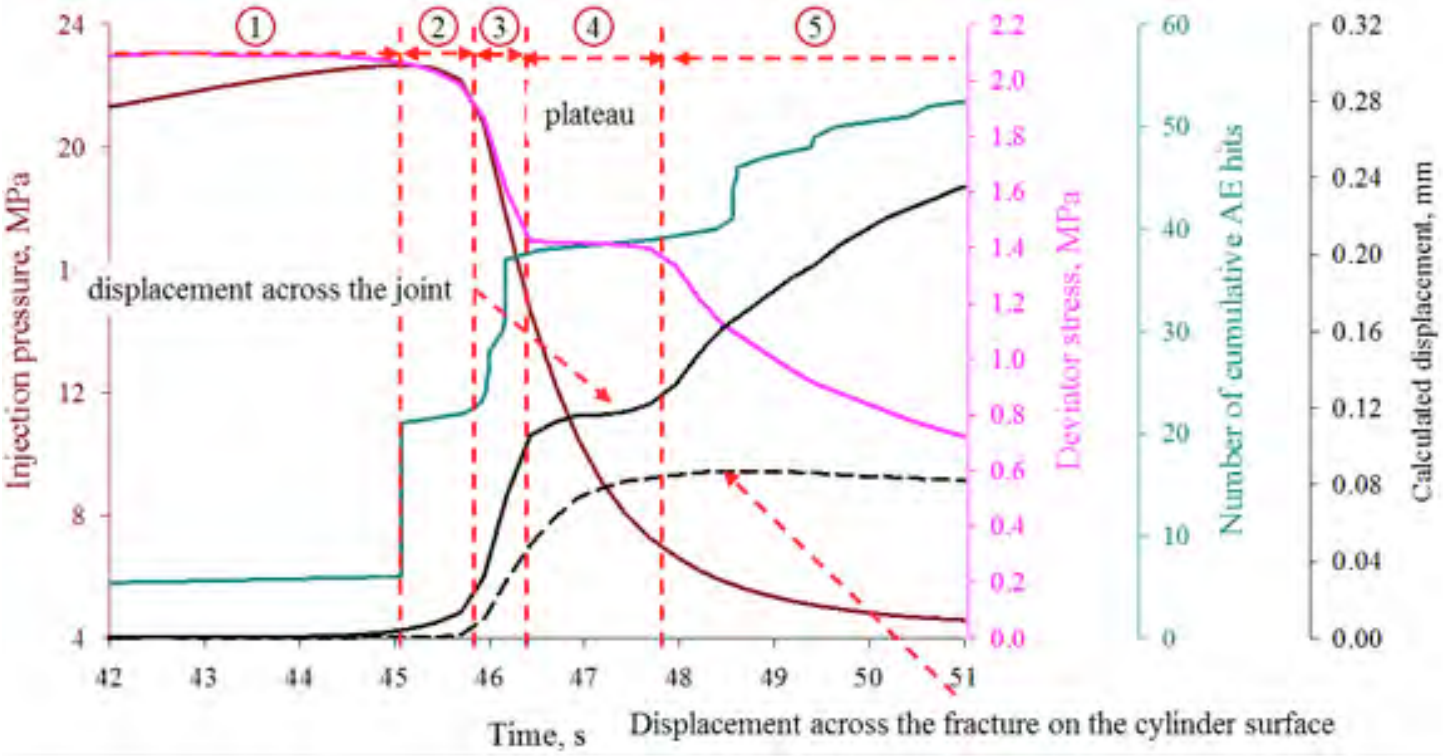

Figure 9. Recorded data and calculated displacement near the breakdown. The slippage of the joint was demonstrated with displacement increment across the joint, deviator stress drop and AE activities.

or are based on unsubstantiated heuristics with insufficient rigor. The uncertainty in the characteristics of natural fracture properties is an often cited reason for neglecting the relevant physical processes in hydraulic fracture simulations. However, the fundamental issue is that hydraulic fracture propagation in the presence of natural fractures is a complex phenomenon and poses significant challenges to numerical modeling. A hydraulic fracture tip approaching a natural fracture can become arrested, or it can cross the natural fracture along its own path or become deflected into the natural fracture, depending on the stress regime ahead of the fracture tip (Koshelev and Ghassemi 2003; Cook and Underwood 2001; Renshaw and Pollard 1995; Warpinski et al. 1987; Blanton 1982; Daneshy 1974). To properly account

for such behavior it is necessary to analyze the stress field near the fracture tip accurately. Fracturing fluid flowing into a natural fracture can cause it to slip and dilate or to mechanically open. Also, as it was shown above, continued fluid injection into natural fractures can result in formation of wing cracks.

A numerical model that fully couples fracture mechanics with fluid flow and considers all aspects of hydraulic/natural fracture interaction at field scale can be quite challenging in terms of numerical stability and computation time even in two dimensions (2D). To our knowledge, most of the current literature (see Zhi et al. 2018) on complex fracture networks is limited to the investigation of hydraulic fracture arrest/crossing behavior with natural fractures. And often, the injection pressure response, stress distribution around fractures, and the shear slip evolution are not reported. In this work we present a complex fracture model based on 2D DDM with a height correction factor that is capable of simulating large scale hydraulic/natural fracture interaction. The natural fractures are modeled using linear joint displacement discontinuity (DD) elements. Fluid flow inside the fractures is modeled using the lubrication equation and is fully coupled with fracture deformation. An inelastic slip model allows slip reversal and transition of natural fracture elements between slip and stick states. Based on LEFM, quasi static fracture propagation is considered where propagating fracture's mixed-mode equivalent stress intensity factor is always at equilibrium with fracture toughness of the rock. Higher order elements are used to calculate stress intensity factors accurately. Fracture crossing/arrest criterion (Gu and Weng 2010; Renshaw and Pollard 1995) are extended and implemented for cases where hydraulic fracture tip is not aligned with principal stresses. The model is first used to present a detailed analysis of the interaction of a single hydraulic fracture with two inclined natural fractures to study the formation of wing fractures. Then, large scale numerical examples are considered using a randomly generated natural fracture network.

First, we consider the behavior of a hydraulic fracture approaching two inclined natural fractures in impermeable rock matrix to closely examine the resulting network using induced stress and pressure distribution plots. The natural fractures are equidistant from the injection point (shown by red circle in Figure 10). The natural fractures are initially mechanically closed with a pore pressure of 25 MPa. However, they are hydraulically conductive due to an assumed residual opening (0.01 mm). A constant fracture height (along Z-axis) of 30 m is assumed for all fracture elements and the XY plots show a top view. The input parameters used are from Zhi et al. (2018). And the horizontal in-situ stress contrast is 5 MPa with the orientation of natural fractures 270 w.r.t the X-axis. The network geometry, net pressure, element status after injecting water for 110 sec at 10 bpm (neglecting leak-off) are shown in Figure 10. The net injection fluid pressure vs time plot from Figure 10b initially shows a decreasing trend from point A as the hydraulic fracture propagates in the direction of the maximum far-field principal stress. The hydraulic fracture arrest at the two natural fractures is indicated by point B where the fluid pressure starts to rise. The net injection pressure rises to point C where one of the tips of natural fractures meets the propagation condition due to slippage (see Figure 10c). The injection pressure drops as the natural fractures re-orient towards the direction of local maximum principal stress and eventually stabilized at around 170 psi. The drop in injection pressure resulted in transition of natural fracture elements from slip to un-slip state (note that according to Zhang and Jeffery (2006), the increase in injection pressure after HF/NF intersection is also function of friction coefficient and distance between injection and fracture intersection locations). Figure 10d shows that at 110 sec, both natural fractures remained mechanically closed. Only the main hydraulic fracture and natural fracture wings which are now aligned with the maximum far-field principal stress are mechanically opened. Also notice that slippage occurred only on the high angle sections of the natural fractures. The low angle sections of natural fractures never experienced slip.

Figure 11a indicates induced tensile σ_{xx} stresses near the high angle sections of both natural fractures due to their slippage. Induced σ_{yy} from Figure 11b indicates increase in compressive stresses on the low angle sections of the natural fractures. As a result, the low angle sections of the natural fractures neither mechanically open nor slip. On the other hand, the high angle sections of the natural fractures experience a decrease in the compressive stresses acting on them due to the induced tensile stresses. This means mechanical slippage on high angle sections of the natural fractures can occur at pressures lower that normal stresses acting on the fracture segment. This is the reason for eventual slip (Figure 10d) of all high angle natural fracture elements.

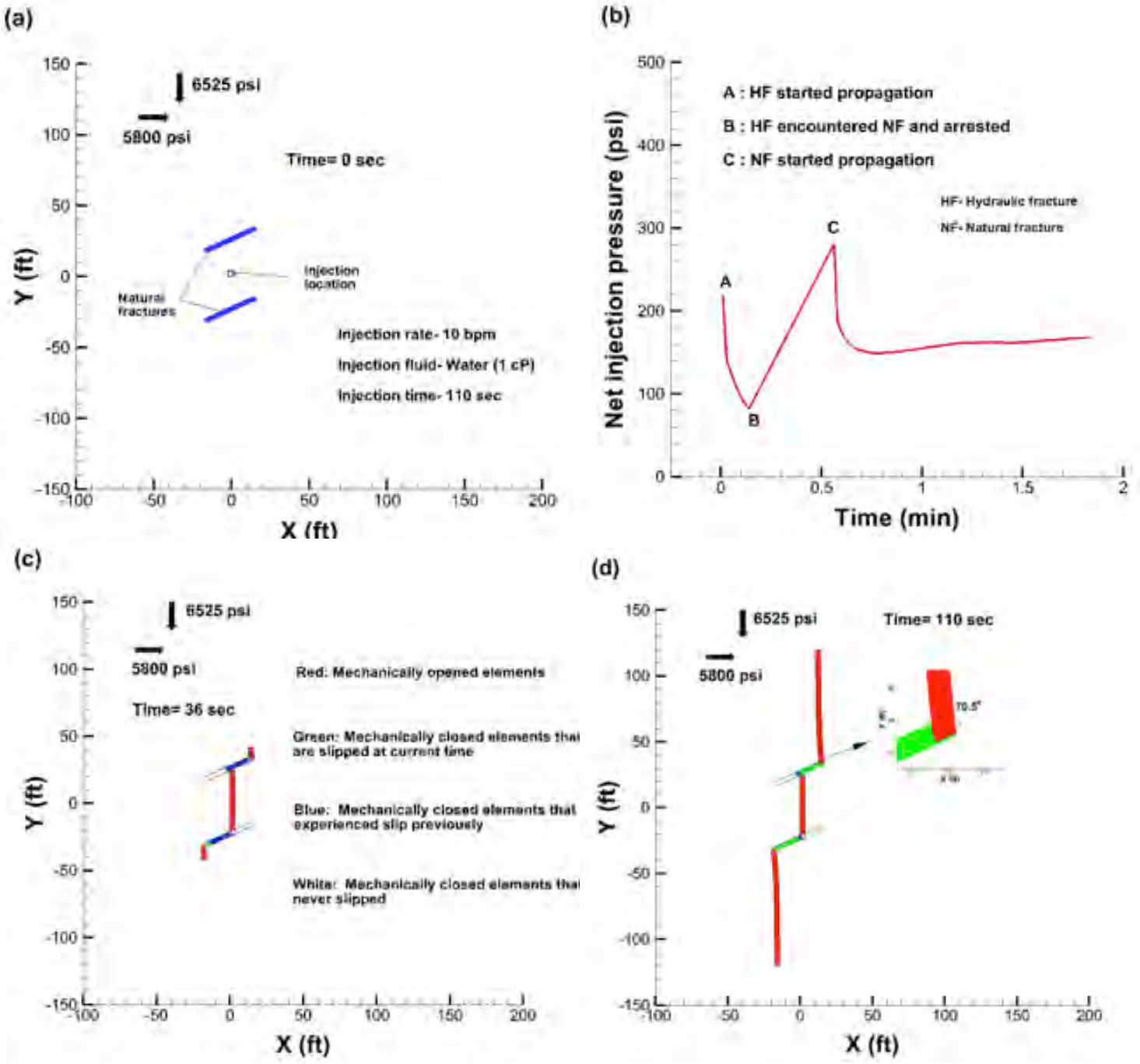

Figure 10. (a) location of natural fractures and injection point with input parameters, (b) net injection pressure profile vs time, (c) status of each fracture element at 36 sec, (d) status of each fracture element at 110 sec (inset showing propagation angle at natural fracture tip).

5.1 Complex fracture network by hydraulic fracturing

Next, fully coupled simulations of hydraulic fractures propagating from three perforation clusters in a network of natural fractures (Figure 12a) are presented. The height of all natural fractures is fixed at 30 m. along the Z-axis. The natural fractures are shown by blue lines oriented 60º-80º with respect to the X-axis. Water is injected at a constant rate of 30 bpm into three perforation clusters simultaneously until hydraulic fractures go beyond the boundaries of the fractured zone. Perforation properties can be found in Figure 13. Other input parameters used in simulator are given in Zhi et al. (2018). Assuming all natural fractures are initially mechanically closed (hydraulic aperture of 0.01 mm and maximum closure of 0.2 mm) with 25 MPa initial pore pressure, and neglecting leak-off and the related pore pressure changes, the effect of far-field horizontal stress contrast on complex fracture network evolution is studied. Figure 13 shows a comparison of the fracture networks

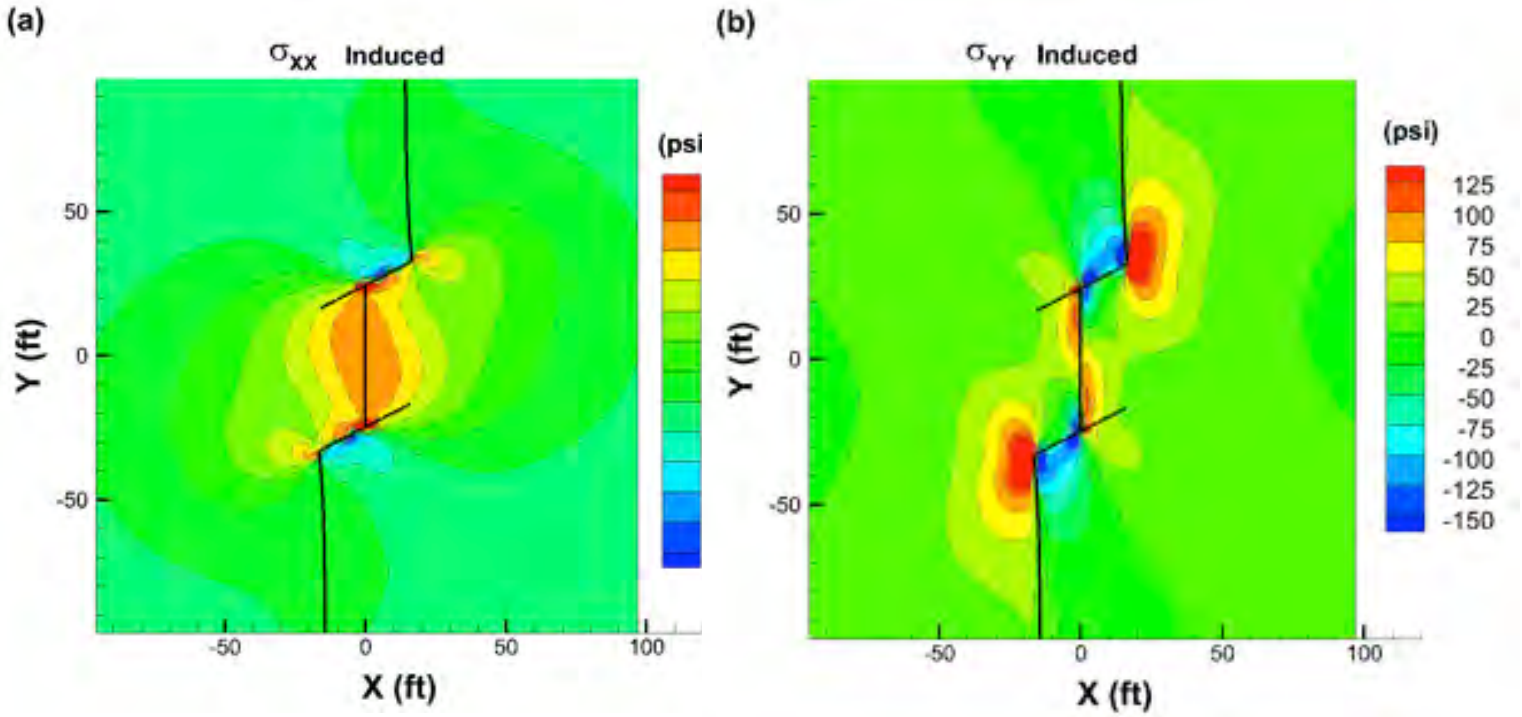

Figure 11. Distribution of induced stress components σ_{xx} and σ_{yy}. Compressive (positive) stresses are induced over the low-angle sections of natural fractures hindering their slip and mechanical opening.

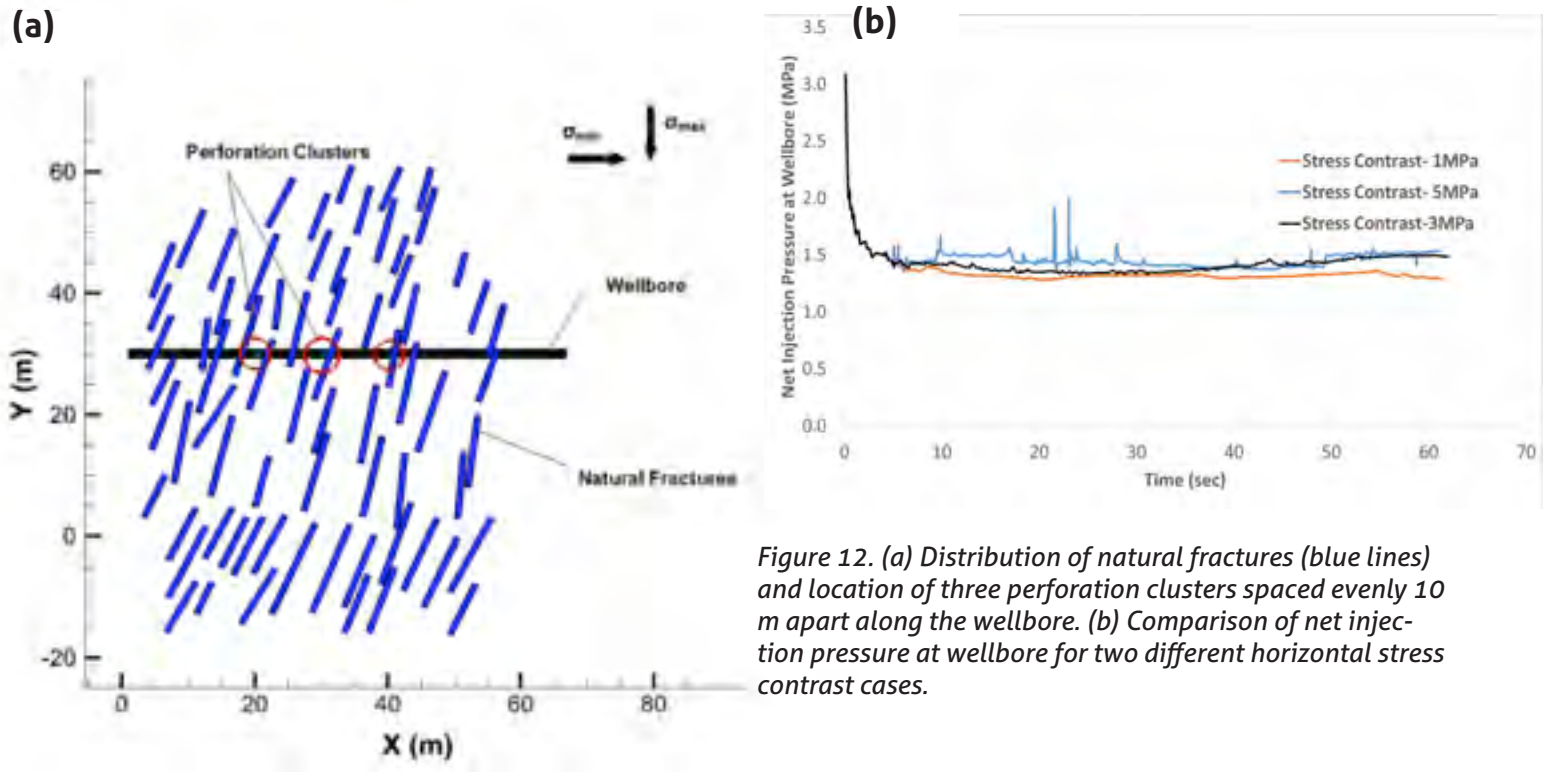

Figure 12. (a) Distribution of natural fractures (blue lines) and location of three perforation clusters spaced evenly 10 m apart along the wellbore. (b) Comparison of net injection pressure at wellbore for two different horizontal stress contrast cases.

obtained under low (1 MPa) and high (5 MPa) in-situ stress contrast situations. Results show asymmetric growth in fracture lengths from all clusters. There is a notable variation in fracture geometry between low and high stress contrast cases. Under the high in-situ horizontal stress contrast all the natural fractures intersected by hydraulic fractures experienced bi-wing propagation (i.e., fracture propagation initiated from both tips of fracture). This is due to higher shear stresses acting on the inclined natural fractures causing sufficient slip to initiate fracture propagation from the tips. The indication is that in some cases a higher complexity may result under a high stress contrast contrary to conventional thinking. Aperture distribution shows high variability along the length of the fractures especially for the cases

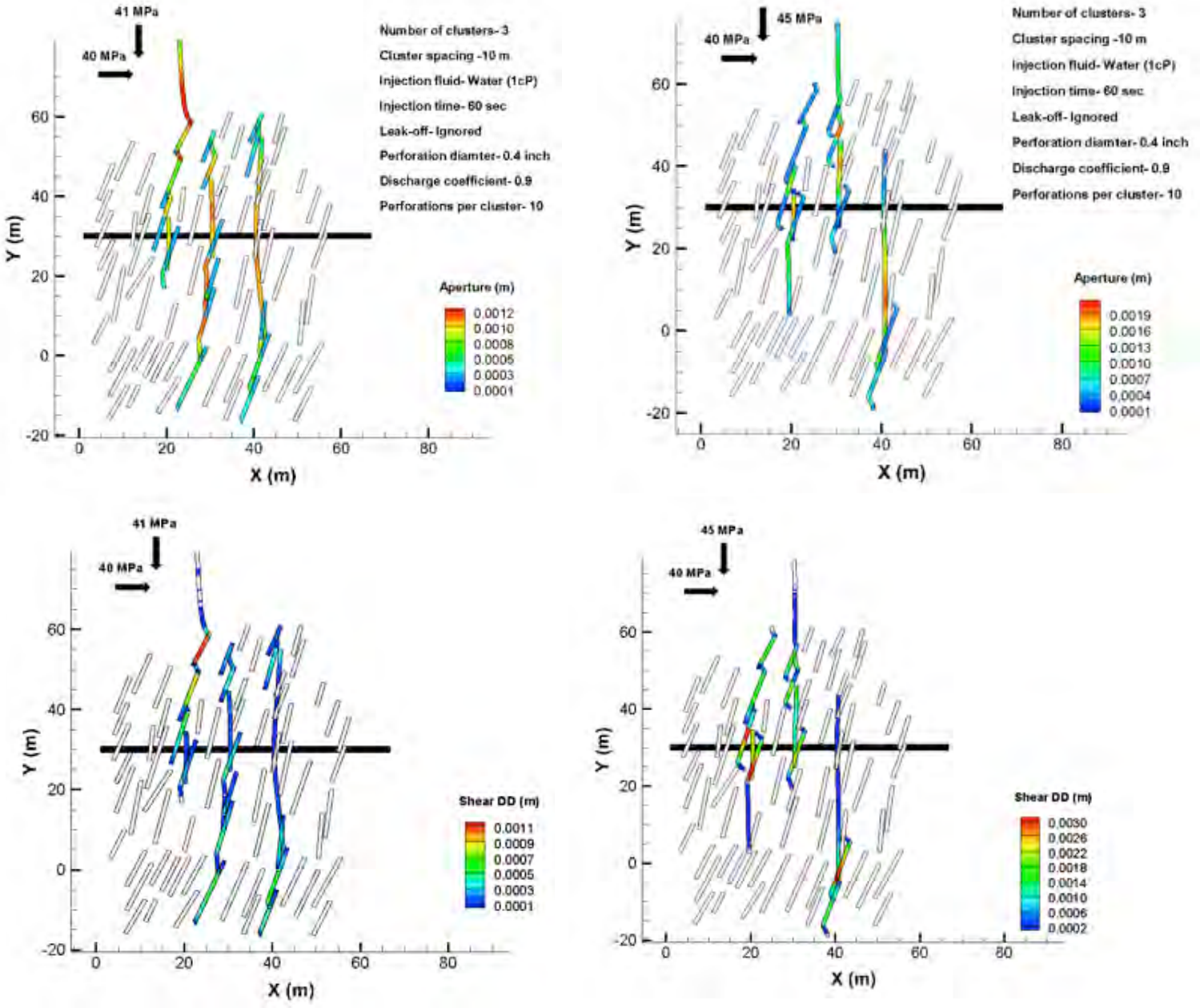

Figure 13. Fracture network, aperture and shear DD distribution obtained after injecting slick water (1cP) into 3 clusters simultaneously at the rate of 30 bpm for 60 sec for different horizontal stress contrast values of 1 MPa and 5 MPa. Results show asymmetric growth in fracture lengths from every cluster. Comparison with Figure 2 shows that stress contrast significantly influences fracture network outcomes (Note that uniform contour scale is not used due large variation in values.)

with high stress contrast. The fracture intersection locations where abrupt change in fracture width is observed can adversely affect proppant placement. The results also indicate almost a threefold increase in shear DD magnitude on natural fractures for high stress contrast case compared to the low stress contrast case. Slippage of natural fractures can enhance fracture permeability, thus increasing the productivity from tight reservoirs. Figure 12b shows a comparison between the net injection pressures obtained for low and high in-situ stress contrast cases. Injection pressure is characterized by initial decreasing trend in both cases. Peaks observed in the injection pressure profile for the high stress contrast cases are due to the change in pressure requirements to cause sufficient slippage on natural fractures to initiate propagation from their tips. (For the low stress contrast case, the pressure change is very subtle.) In this example, a significant difference between injection pressures for high and low in-situ stress contrast cases is not observed (this is not always the case; for cases where natural fracture orientation is closer to the minimum stress, large variation in injection pressures can be observed between low and high stress contrast cases (see Zhi et al. (2018)).

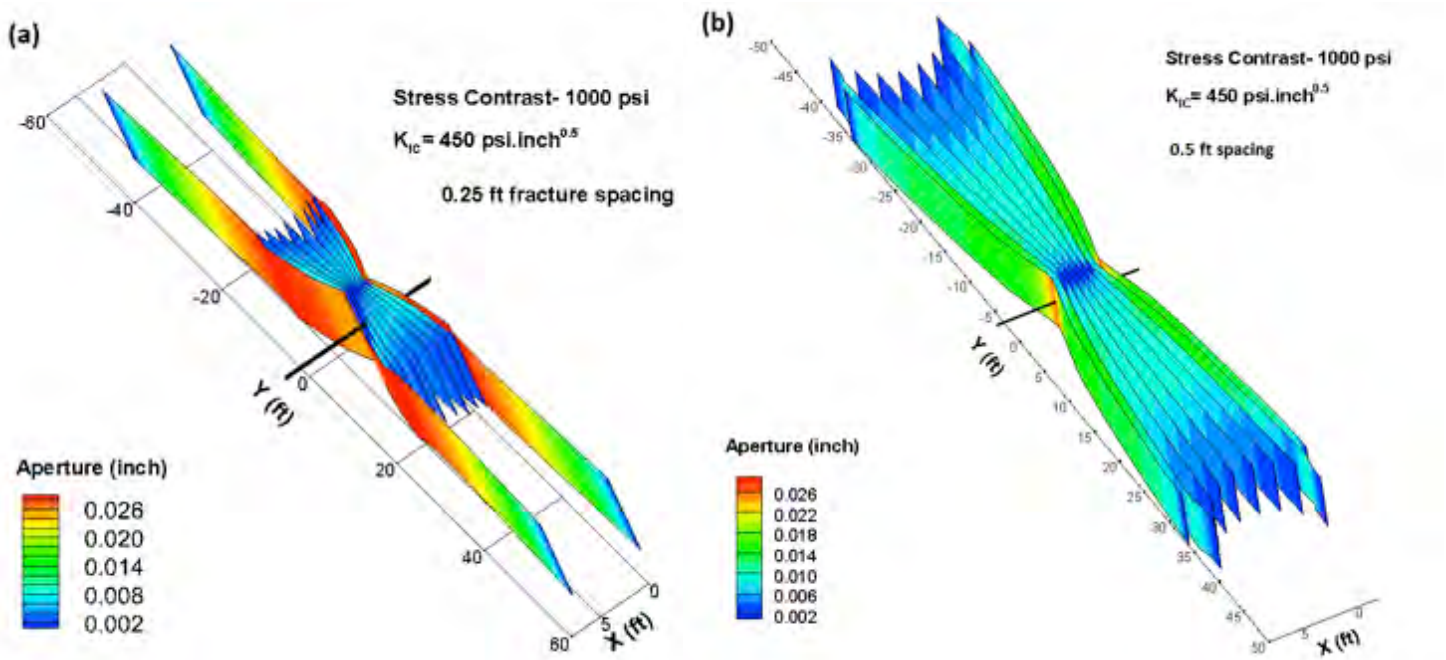

Figure 14. Hydraulic fractures emanating from a cluster of 20 perforations with 1800 phasing. Two perforations constitute one fracture for the case (a) with cluster span of 2.5 ft and with (b) cluster span of 5 ft.

5.2 Fracture clusters or swarms

The current hydraulic fracture models are based on the assumption that a single fracture emanates from each perforation cluster. However, laboratory experiments (van de Ketterij and de Pater, 1999) performed on a perforated wellbore indicated multi-strands rather than a single fracture. Multi-stranded fracture propagation far from the wellbore is also evident from mine-back experiments and cored intervals of hydraulically fractured rock. Warpinski et al., (1993) observed 30 hydraulic fractures over a span of just 4 ft. along the cored interval, far exceeding the number of perforation clusters which is two. Mine-back experiments in coal seams (Jeffrey et al., 1993) also indicated multiple fractures with spacing of just 1 ft. Core samples from hydraulic fracturing test site (HFTS) (Gale et al., 2018) and the Eagle Ford field test (Raterman et al., 2017) indicated hydraulic fractures occurring in dense clusters. In the Eagle Ford field test, fracture clusters of densities up to 60 fractures per 50 ft. of the cored interval are observed. Physical observation of cores and image logs revealed that most of the fractures occurring in swarms are parallel to each other.

Figure 14 shows fracture networks obtained from a single perforation cluster that has a span of 2.5 ft and 5 ft. respectively. Each cluster has 20 perforations with 180 degree phasin, constituting 10 fractures per cluster. Near wellbore effects on fracture growth are ignored. Elastic properties of Eagle Ford shale are assumed. The fracture toughness is 0.5 MPa.m0.5 and in-situ horizontal stress contrast is 7 MPa. Water is injected at a rate of 20 bpm. Fracture height is fixed at 30 ft. but height effect is considered in the 2D solution using a height correction factor. The results show that inner fractures achieved growth of up to 35 ft from the wellbore for spacing of 0.5 ft. while only 20 ft. for the case with 0.25 ft. spacing. Aperture distribution indicates opening of the inner fractures is extremely impeded. Under extremely close spacing, the illustrated numerical examples indicate cluster lengths much less than that suggested by the field evidence pointing to the limits to the simulation that may be found in the assumption of fixed height. This issue is explored further below.

Field data also suggest that hydraulic fracture segmentation along the height also occurs. Coring experiments and outcrops indicate vertical fracture stepping at planes of weakness or bedding planes. Natural fracture height measured (Gale et al. 2014) in cores from various shales is observed in the range of 1 cm to 1.8 m. Spacing between vertical natural fractures is observed to be a strong function of bedding plane thickness. Since height is the parameter controlling the stress shadow, it is expected that fractures with smaller height can accommodate closer spacing. In the 2D simulations (see Figure 14), a height of 30 ft. was used, overestimating the stress shadow effect between the fractures and resulting in the early termination of fractures. Segmentation of fractures both vertically and laterally along the wellbore could mean the formation of hundreds of

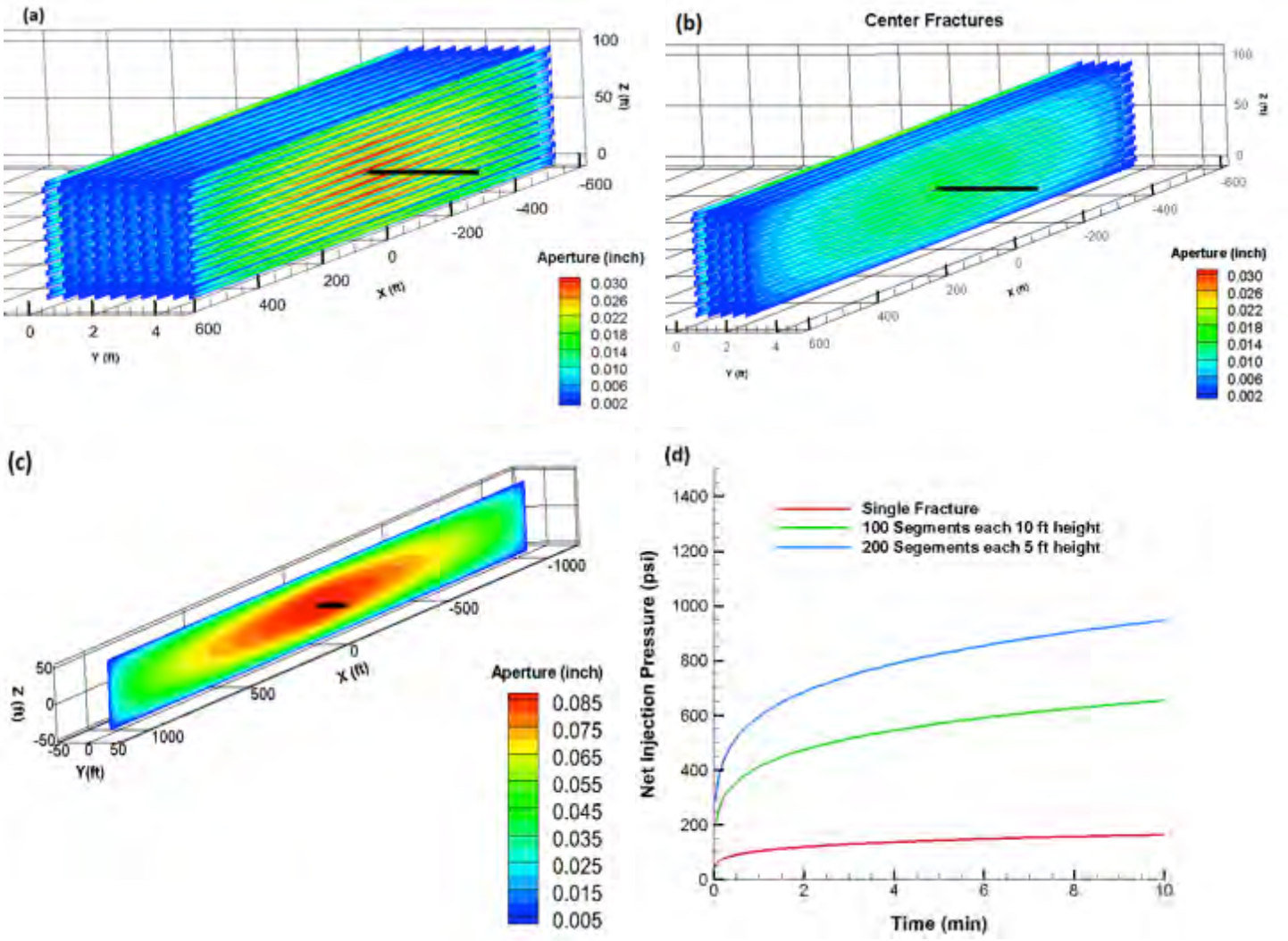

Figure 15. (a) Aperture distribution and geometry of a multi-segmented fracture emanating from a cluster of perforations. A total of 200 segments is assumed with segment height of 5 ft, (b) aperture distribution among the inner segments, (c) aperture distribution and geometry of a single fracture emanating from a perforation cluster with same input as multi-segmented fracture, (d) comparison of injection pressure profile between the single fracture model and multi-segment fracture model.

fractures instead of a single planar fracture during stimulation. Modeling propagation of thousands of fractures is impractical with current computational resources as the size of the grid or element (e.g., boundary element) in a numerical model cannot exceed the spacing between the fractures. As an alternative we use a semi-analytical P3D (Planar 3D) model where multi-stranded fractures are treated as a single equivalent fracture while at the same time accounting for the stress shadow effects between the closely spaced fracture segments.

Figure 15a shows the fractures geometry and aperture distribution obtained after injecting water at 20 bpm into a single perforation cluster for 10 min (ignoring leak-off). For illustrative purposes we consider 10 fracture segments in the lateral direction and 20 fracture segments along the vertical from one perforation cluster. Assuming each segment has a height of 5 ft., the offset between the vertical segments is taken as 2% of the segment height, underlap is 5% of segment height, and spacing between the segments is taken as 10% of the segment height. Fractures are assumed to be contained within the payzone of thickness 105 ft. Uniform segments height and spacing is used in the simulations for illustration, and is not a model limitation. Fluid communication between the fracture segments is assumed to occur through bedding planes or natural fractures not explicitly modeled. Results show uneven distribution of fracture aperture among the outer segments due to fracture stepping. The majority of the inner fractures (Figure 15b) have opening less than 50% of value observed for the outer most fractures. Fracture half-length is 560 ft. For the same input parameters we now assume propagation of a single fracture from a perfora-

tion cluster instead of multi-strands. Comparing the results for this case (Figure 15c) with multi-segmented model results (Figure 15a) indicate that single fracture model overestimated the fracture aperture by three times and the half-length by two times. Figure 15d shows the net injection pressures. Results indicate the net pressure increases significantly with increase in the number of fracture segments vertically for a fixed payzone thickness. The analysis presented here is consistent with the high net injection pressures (often exceeding 10 MPa) observed in the field that cannot be explained by other existing fracture models (planar and non-planar complex fracture models). As a remedy the conventional fracture models rely on calibration which requires significantly altering the fluid and rock properties to match field observed injection pressures and fracture lengths. Such calibration measures might remedy the error in the fracture length calculation, but the apertures of individual fracture strands cannot be obtained which is a critical parameter for proppant transport.

6. Poroelastic Processes in "Frac Hits"

The importance of refracturing of horizontal wells or infill wells in the unconventional reservoirs is well recognized in oil and gas industry. The refracturing technique can restore or increase well productivity, and fracturing of infill wells provides additional reserves by draining rock volume not previously stimulated. The latter situation is often referred to as stimulating a "child" well near the "parent" well. The production from the parent well fractures creates a "pressure sink" and associated poroelastic stress reduction zones (e.g., Safari et al., 2016; Kumar et al., 2018a &2018b, Ghassemi and Zhang, 2006; Perkins and Gonzalez, 1985; Siebrits et al., 1998; Elbel and Mack, 1993). If another well is drilled nearby this zone and is stimulated, its hydraulic fractures would tend to get attracted to the depleted zone where the reservoir stresses resisting propagation are lower. This would potentially promote communication between the "parent" and "child" wells, which is termed a "frac-hit". The "frac-hit" may lead to reduced productivity of the parent wells or its complete damage. Re-fracturing or re-pressurization of the parent well has been suggested as a means of mitigating "frac-hit" risks.

To investigate the reservoir pore pressure and stress changes, consider a hydraulic fracturing stage with three fracture clusters spaced 25m apart (with one propagating fracture each cluster) in a normal faulting stress regime. (The in-situ stresses and mechanical properties of the reservoir rocks can be found in Kumar et al. (2018a)). The production and the infill wells are drilled parallel to the x-axis along the minimum horizontal stress, and the hydraulic fractures have formed perpendicular to the wellbore axis. The fractures' half-length is equal to 90 m with a height of 60 m. The hydraulic fractures are assumed to be propped having a uniform initial fracture aperture of 2.0 mm. The reservoir is depleted at a constant production pressure of 10.5 (MPa) for 2 years.

A 3D visualization of the reservoir pore pressure and the stress changes after 2 years of production are shown in Figures 16a-d, respectively. An ellipsoidal pressure depletion zone has formed around the production fractures where the pore pressure is lowered to 12 MPa (from 50.6 MPa). The effect of the pore pressure reduction on the horizontal stress component σ_{xx} is shown in Figure 16b where it can be seen its value has decreased to 45 MPa (from 54.30 MPa). The distribution of the σ_{yy} component is shown in Figure 16c; it has decreased to 46 MPa (from 57.72 MPa). The vertical stress component, σ_{zz}, also experienced a reduction from 73.16 to 64 MPa. A plan-view (the central xy-plane) of the reservoir pore pressure distribution and the difference between the horizontal stress components (i.e., $\sigma_{yy} - \sigma_{xx}$) is shown in Figure 17. The dark blue regions show negative values of the stress differential indicating a stress reversal.

Now consider that after two years of depletion, the infill well is to be hydraulically fractured. For this purpose we simulate the infill well fractures without considering poroelasticity. A fracture cluster with a single propagating fracture is simulated in this case. It is assumed that water (0.001 Pa.s viscosity) is injected at a constant rate of 0.1 m3/s (an initial fracture radius of 2 m is assumed to simulate the perforations). The fracture geometry before and after re-pressurization of the "parent" well fractures is shown Figure 18. The "child" well fracture shows asymmetric growth towards the "parent" well and in the vertical direction (i.e., along z-axis) due to vertical stress gradient. This is because the infill well fracture experiences a reduced stress zone near the production well which can potentially lead to communication with the parent well and "frac-hits" problems. However, when parent well fractures are re-pressurized, the child well fracture shows symmetric growth with respect to the wellbore axis. Nevertheless, height growth possibility exists which can lead to communication with a parent well above the child well. (Note that as we have pointed out previously (Kumar and Ghassemi, 2017, Kumar et al., 2018a & 2018b) 2D modeling cannot capture this effect.)

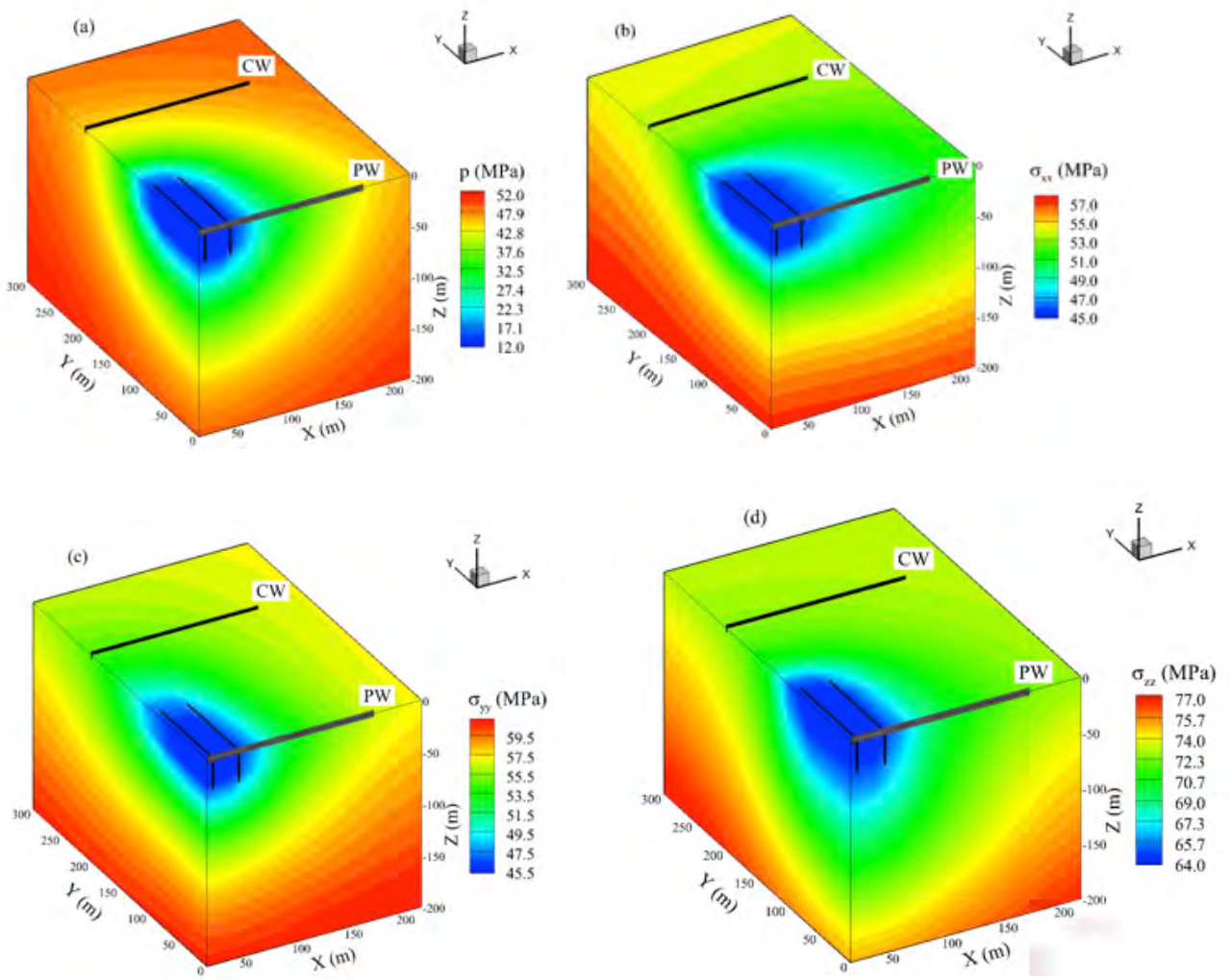

Figure 16. A 3D visualization of reservoir pore pressure and the total stresses after 2 years of production, (a) reservoir pore pressure, (b) minimum horizontal stress, (c) maximum horizontal stress, (d) the vertical stress. The far-field minimum horizontal (σ_h)and maximum horizontal (σ_H) in-situ stresses are acting along x- and y-axes, respectively. The vertical in-situ stress (σ_V) is acting along z-axis. Note that by symmetry it occurs only for 1/4th of the reservoir volume.

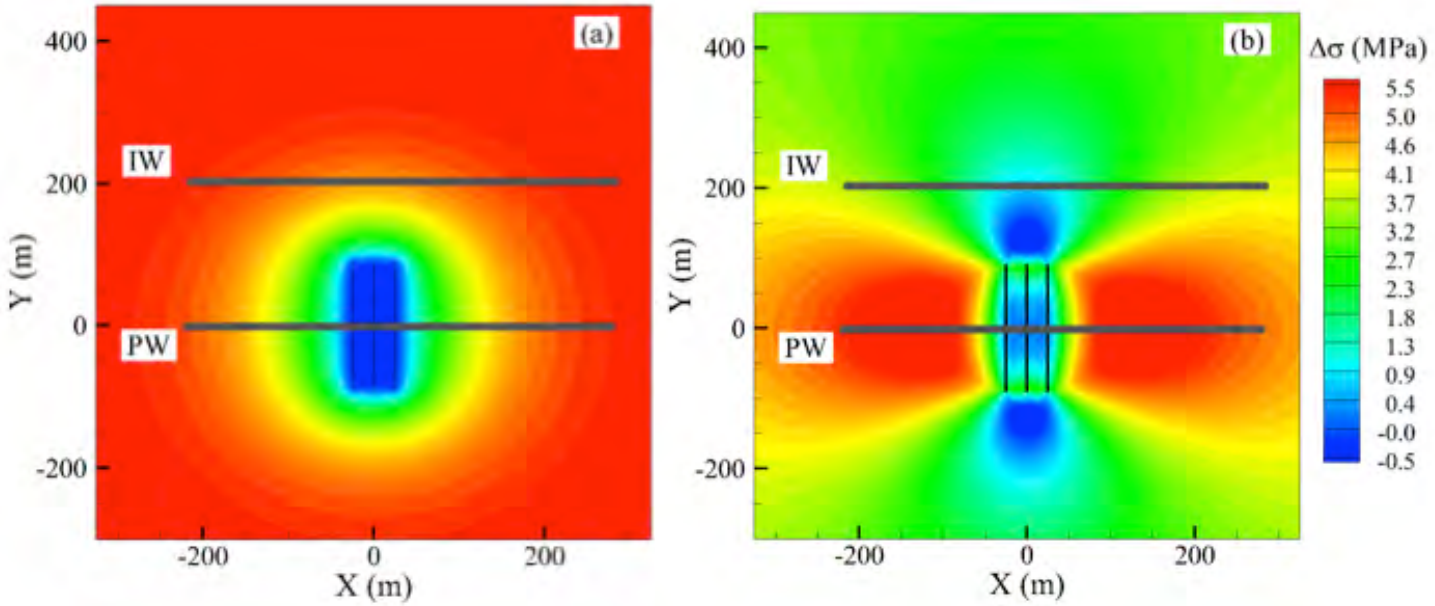

Figure 17. Plan-view of (a) reservoir pore pressure, (b) the horizontal stress contrast distribution after 2 years of production in the central xy-plane. The negative values of the horizontal stress contrast show the stress reversal zones.

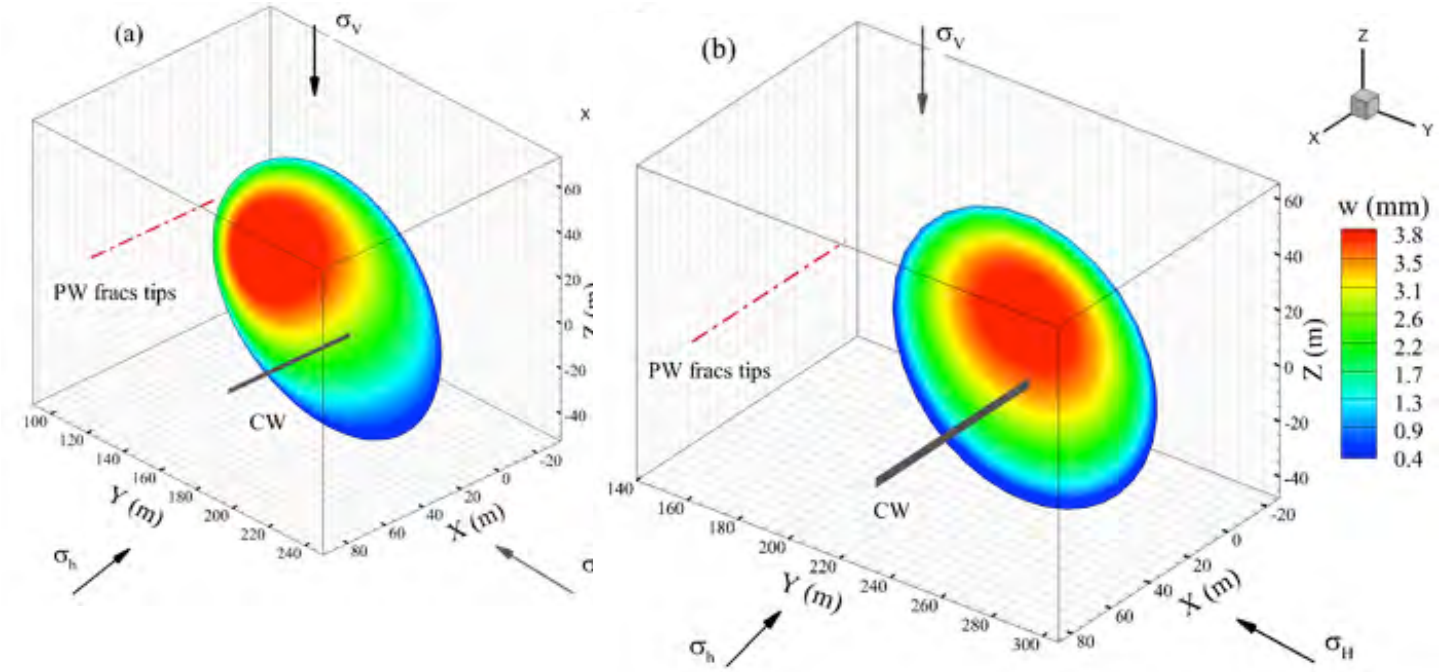

Figure 18. Fracture geometry and apertures of "child" well fracture propagation; (a) before re-pressurization the "parent" well fracture, (b) after re-pressurization of the "parent' well fractures.

7. Conclusions

In this work, new experimental results were presented to quantify rock brittleness and to reveal different stimulation mechanisms (slip and mixed-mode propagation) and their impact on permeability enhancement. In addition, it was shown that natural fracture can experience slip by stress perturbation caused by an encroaching hydraulic fracture. The numerical analyses presented in this paper capture some of the fundamental physics of HF/NF interactions by rigorous modeling of the natural fracture constitutive behavior and fracture mechanics involved in hydraulic fracturing. Such modeling is not only a useful tool for gaining insights on the role of in-situ stress contrast and induced stresses on evolution of fractures networks but also for optimizing cluster spacing, and for better interpretation of micro-seismic signals. It was also shown via advanced modeling that field-observed phenomena such as clusters of closely-spaced hydraulic fractures can occur and their evolution controlled via manipulation of geomechanical parameters. An alternative approach to explaining the frequently observed high net pressure during hydraulic fracturing was also described by modeling and analysis of multi-segmented P3D fractures. Finally, the role of poroelastic mechanisms in the so called "Frac-Hit" issue was illustrated in 3D using a fully coupled approach with real fracture propagation. It was shown that re-pressurization of the "parent well" can lower the risks of well-to-well interference during infill-well fracturing. The results also underscored the need for 3D simulation.

A key assumption made in this paper is rock anisotropy. However, as we have shown previously (Sesetty and Ghassemi, 2016; 2018) rock anisotropy (both modulus and strength) can have a significant influence on hydraulic fracture geometry. Preliminary analysis indicates that mechanical interaction between hydraulic fractures is enhanced in VTI (vertical transversely isotropic) rocks due to an increase in stress shadow effect. This can result in early termination of fractures from inner clusters and exacerbate the condition of heel bias. Also, it is found that treating VTI rocks as isotropic results in significant overestimation of fracture height growth (Sesetty and Ghassemi, 2018b). Fracture re-orientation and steering models developed to date are unable to account for rock heterogeneity which impacts the stress shadow and the stress reversal patter (Gao and Ghassemi, 2017). Also, the issue of fracture containment in layered rock systems is of critical importance to unconventional stimulation and requires special treatment (Gao and Ghassemi, 2019ab). Improved numerical modeling strategies are needed to more efficiently account for fracture complexity related to rock texture and fabric. In addition, better tools for prediction and analysis of MEQ activity, and stress-dependent permeability models are necessary to better assess the stimulated rock volume and its dynamics with production. Finally, sustaining the conductivity of generated fracture networks requires a better understanding of proppant pack diagenesis while considering rock and fluid interactions.

References

Andreev, G. E. (1995), Brittle failure of rock materials: test results and constitutive models, Taylor & Francis.

Blanton, T. L. 1982. An experimental study of interaction between hydraulically induced and pre-existing fractures. In SPE unconventional gas recovery symposium.

Cipolla, C.L., Warpinski, N.R., Mayerhofer, M.J. et al. 2008. The Relationship between Fracture Complexity, Reservoir Properties, and Fracture Treatment Design. Paper presented at the SPE Annual Technical Conference and Exhibition, Denver, Colorado, USA. SPE, 115.

Chipperfield, S.T., Wong, J.R., Warner, D.S. et al., 2007. Shear Dilation Diagnostics: A New Approach for Evaluating Tight Gas Stimulation Treatments. Paper presented at the SPE Hydraulic Fracturing Technology Conference, College Station, Texas USA. Society of Petroleum Engineers 106.

Cooke, M. L., & Underwood, C. A. 2001. Fracture termination and step-over at bedding interfaces due to frictional slip and interface opening. Journal of Structural Geology, 23(2-3), 223-238.

Cornet, F. H., Berard, T., Bourouis, S. 2007. How close to failure is a granite rock mass at a 5 km depth? International Journal of Rock Mechanics and Mining Sciences, 44(1), 47-66. doi: 10.1016/j.ijrmms.2006.04.008.

Daneshy, A. A. 1974. Hydraulic fracture propagation in the presence of planes of weakness. In SPE European Spring Meeting.

Elbel, J.L., and Mack, M.G.1993. Refracturing: Observations and Theories. SPE 25464, the Production Operations Symposium, Oklahoma City, OK, USA, 21-23 March.

Gao, Q., and Ghassemi, A. 2018. Parallel finite element simulation of 3D hydraulic fracture propagation using a coupled hydro-mechanical interface element. 52th US Rock Mechanics/Geomechanics Symposium, San Francisco, CA, USA, 17 June-20 June.

Gale, J.F., Elliott, S.J. and Laubach, S.E., 2018, September. Hydraulic Fractures in Core from Stimulated Reservoirs: Core Fracture Description of HFTS Slant Core, Midland Basin, West Texas. In Unconventional Resources Technology Conference, Houston, Texas, 23-25, 1340-1357.

Gale, J. F., Laubach, S. E., Olson, J. E., Eichhubl, P., & Fall, A. 2014. Natural fractures in shale: A review and new observationsNatural Fractures in Shale: A Review and New Observations. AAPG bulletin, 98(11), 2165-2216.

Gao, Q., Ghassemi, A., 2017.Pore pressure and stress distributions around a hydraulic Fracture in heterogeneous rock. Rock Mech. Rock Eng. 50(12), 3157–3173.

Gao, Q., Ghassemi, A. 2019a. Height Growth in Layered Unconventional Reservoirs: The Impact of Modulus, Bedding Planes and Natural Fracture Properties. Urtec, Denver, CO.

Gao, Q., Ghassemi, A. 2019b. Hydraulic fracturing in unconventional reservoirs: the impact of layering and permeable frictional interfaces. SPE ATCE, Calgary, CA.

Ghassemi, A., and Zhang, Q. 2006. Poro-thermoelastic response of a stationary crack using the displacement discontinuity method. ASCE J. Engineering Mechanics, 132(1), 26-33.

Gu, H., & Weng, X. 2010. Criterion for fractures crossing frictional interfaces at non-orthogonal angles. In 44th US rock mechanics symposium and 5th US-Canada rock mechanics symposium.

Huang, K., Zhang, Z., & Ghassemi, A. 2013. Modeling three-dimensional hydraulic fracture propagation using virtual multidimensional internal bonds. International Journal for Numerical and Analytical Methods in Geomechanics, 37(13), 2021-2038. doi: 10.1002/nag.

Jin, X., Shah, S. N., Roegiers, J. C., & Zhang, B. 2015. An integrated petrophysics and geomechanics approach for fracability evaluation in shale reservoirs. SPE Journal, 20(03), 518-526.

Jung, R. 2013. EGS — Goodbye or Back to the Future. Paper presented at the ISRM International Conference for Effective and Sustainable Hydraulic Fracturing, Brisbane, Australia.

Jeffrey, R.G., Enever, J.R., Phillips, R., Ferguson, T., Davidson, S.C. and Bride, J., 1993. Small-scale hydraulic fracturing and mineback experiments in coal seams.

Kahn et al., 2017. Integrating Microseismic and Geomechanics to Interpret Hydraulic Fracture Growth, Unconventional Resources Technology Conference (URTEC).

Koshelev, V. and Ghassemi, A., 2003. Hydraulic fracture propagation near a natural discontinuity. Pro-

ceeding of the 28th Workshop on Geothermal Reservoir Engineering Stanford University, Stanford, CA.

Li, Y., and Ghassemi, A., 2018, August. Rock Failure Behavior and Brittleness under the Confined Brazilian Test. In 52nd US Rock Mechanics/Geomechanics Symposium. American Rock Mechanics Association.

Mayerhofer, M.J., Richardson, M.F., Walker Jr., R.N., Meehan, D.N., Oehler, M.W., Browning Jr., R.R., 1997. Proppants? We Don't Need No Proppants. SPE Annual Technical Conference and Exhibition, San Antonio, Texas. 38611-MS.

Min, K. S., Zhang, Z., & Ghassemi, A. 2010. Numerical Analysis of Multiple Fracture Propagation In Heterogeneous Rock. Paper presented at the 44th U.S. Rock Mechanics Symposium and 5th U.S.-Canada Rock Salt Lake City, Utah.

Perkins, T.K., and Gonzalez, J.A. 1985. The effect of thermoelastic stress on injection well fracturing. SPE Journal 2: 78-88.

Raterman, K.T., Farrell, H.E., Mora, O.S., Janssen, A.L., Gomez, G.A., Busetti, S., McEwen, J., Davidson, M., Friehauf, K., Rutherford, J. and Reid, R., 2017, September. Sampling a stimulated rock volume: an eagle ford example. In Unconventional Resources Technology Conference, Austin, Texas, 24-26 July 2017 (pp. 937-954).

Renshaw, C. E., & Pollard, D. D. 1995. An experimentally verified criterion for propagation across unbounded frictional interfaces in brittle, linear elastic materials. Int. J. Rock Mech. & Min. Sci. & Gomech. Abst, 32, 3, 237-249).

Roussel, N.P., Florez, H.A., and Rodriguez, A.A. 2013. Hydraulic fracture propagation form infill horizontal wells. SPE 166503, SPE Annual Technical Conference and Exhibition, New Orleans, LA, USA, 30 September-2 October.

Rutledge, J. T., and Phillips, W.S. 2003. Hydraulic stimulation of natural fractures as revealed by induced micro-earthquakes, Carthage Cotton Valley gas field, East Texas, Geophysics, 68(2), 441-452.

Rybacki, E., Meier, T., & Dresen, G. 2016. What controls the mechanical properties of shale rocks?–Part II: Brittleness. Journal of Petroleum Science and Engineering, 144, 39-58.

Safari, R., and Ghassemi, A. 2015. 3D thermos-poroelastic analysis of the fracture network deformation and induced micro-seismicity in enhanced geothermal systems. Geothermics, 58: 1-14.

Safari, R., and Ghassemi, A. 2016. Three-dimensional poroelastic modeling of injection induced permeability enhancement and micro-seismicity. Int. J. of Rock Mech. and Mining Sci., 84:47-58.

Safari, R., Ma, Lewis, R., X., Mutlu, O., and Ghassemi, A. 2016. Infill well fracturing optimization in tightly spaced horizontal wells. SPE Journal. SPE-178513-PA.

Sesetty, V., & Ghassemi, A. 2018a. Effect of rock anisotropy on wellbore stresses and hydraulic fracture propagation. International Journal of Rock Mechanics and Mining Sciences, 112, 369-384.

Sesetty, V., Ghassemi, A., & Gil, I. 2018b. An Integrated Field and Numerical Study of the Impact of Formation Anisotropy on Stage Spacing in Horizontal Wells. Unconventional Resources Technology Cnference. doi:10.15530/URTEC-2018-2878152.

Sesetty, V., & Ghassemi, A. 2016.. Numerical modeling of hydraulic fracture propagation from horizontal wells in anisotropic shale. In 50th US Rock Mechanics/Geomechanics Symposium. American Rock Mechanics Association.

Siebrits, E., Elbel, J.L., Detournay, E., Detournay-Piette, C., Christianson, M., Robinson, B.M., and Diyashev, I.R. 1998. Parameters affecting azimuth and length of a secondary fracture during a fracture treatment. SPE 48928: SPE Annual Technical Conference and Exhibition, New Orleans, 27-30 September.

Van Ketterij, R.B. and De Pater, C.J., 1999. Impact of perforations on hydraulic fracture tortuosity. SPE production & facilities, 14(02), pp.117-130.

Warpinski, N.R., Lorenz, J.C., Branagan, P.T., Myal, F.R. and Gall, B.L., 1993. Examination of a Cored Hydraulic Fracture in a Deep Gas Well (includes associated papers 26302 and 26946). SPE Production & Facilities, 8(03), pp.150-158.

Warpinski, N. R., & Teufel, L. W. 1987. Influence of geologic discontinuities on hydraulic fracture propagation (includes associated papers 17011 and 17074). Journal of Petroleum Technology, 39(02), 209-220.

Zhang, X., & Jeffrey, R. G. (2006). The role of friction and secondary flaws on deflection and re-initiation of hydraulic fractures at orthogonal pre-existing fractures. Geophysical Journal International, 166(3), 1454-1465.

Zhang, D., Ranjith, P. G., & Perera, M. S. A. 2016. The brittleness indices used in rock mechanics and their application in shale hydraulic fracturing: A review. Journal of Petroleum Science and Engineering, 143, 158-170.

A Primer on Finite Difference Simulation of Unconventionals

Submitted by Vladimir Petunin, NITEC, LLC, Denver, Colorado.

Abstract

For hydraulically stimulated wells, a holistic methodology that combines a flow model with a rock fracture model in one simulation can be useful in ways that a strictly segregated model cannot. The hydraulic fracturing process cannot be modeled as a fully reversible one and needs hysteresis in the flow simulator. The model presented here takes the completion reports from the completed wells and introduces those volumes of injected fluids and rates along the well to simulate what was done in real life. The model estimates the production from that well during the simulation run. This model uses a one-second time step during stimulation. The time step increases to a day during the production period. Results related to how frac interactions, frac barriers, and depletion can interact are presented. At this time these techniques have been applied for many years. This model only uses a pseudo-stress solution; a fully integrated stress solution will be developed in near future.

1. Introduction

The primary challenge of modeling unconventional wells is the hysteresis that occurs after hydraulic fracturing is completed. Hundreds of thousands of barrels of water are injected into the wells and when they are opened within a week, the pressure in the wells may be a bit elevated or may be back to the initial reservoir pressure. Certainly the drainage volume of a well will dip below the initial reservoir pressure long before the hundreds of thousands of barrels that were injected are produced. From a material balance perspective, this is an interesting phenomenon.

Typically, the simulation process requires the user to estimate the size and shape of the Simulated Reservoir Volume (SRV). This estimate is typically assisted by the hydraulic fracturing simulators. Historical water production is ignored, as no water was injected into the model to create the SRV. Pressure is also ignored [1, 2]. The pressure aspect is interesting because by specifying the pressure in the simulator that the simulator should achieve without water injection raises questions on energy ignored. History match can be achieved in the process, but it is not going to predict more than what that specific well may do in the future. Hysteresis is ignored because material balance is ignored. Exploration of alternative development scenarios by varying well placement and fractured zone size cannot be done because changing these parameters invalidates the history match [3].

The approach presented here instead focuses on combining the stimulation and production into one model. By doing so, the questions of material balance must be addressed. Many paths of hysteresis created by the stimulation must be addressed. Fracture hits in more mature development scenarios have to be addressed. When all these physics are incorporated, then issues about well placement and spacing can be addressed.

In spite of the best attempts, simulation will always be imperfect. Models developed based on single well sections have been improved by results from multiple well sections. Those multiple well sections results have been further improved by exploration below or above the initial interval of interest.

2. Mechanism

The first assumption of the commercial simulator used in this work is that that the minimum stress is strength for the purpose of fracturing rock following Terzaghi [4]:

$$\sigma_{eff} = \sigma_{\min} - \alpha P_{pore}$$

Here, σ_{eff} is the effective stress, $\sigma_{\min}$ is the minimum stress (fracture gradient), α is the Biott's coefficient, and P_{pore} is the pore pressure. Each cell is assigned with a minimum stress to build the simulation model. Each cell also has an initial pressure. As water is injected into a cell its pressure increases and, as per Terzaghi's equation, the effective stress decreases. Failure of each cell is controlled by a user-supplied table, which controls the failure of the cell as the stress continues to decrease. The same table also controls the cell closure as pressure eventually decreases.

2.1 Propagation

Dual porosity is used for this simulator. In the dual porosity model, a grid block is divided into a matrix (isolated) and fracture (connected) [5, 6] simulation cells. The matrix cell can only communicate with the fracture cell it shares a grid block with. The fracture cells then can communicate with other grid blocks. Figure 1 shows that a fracture can propagate only through the fracture cells while improving the communication between the fracture and matrix cells.

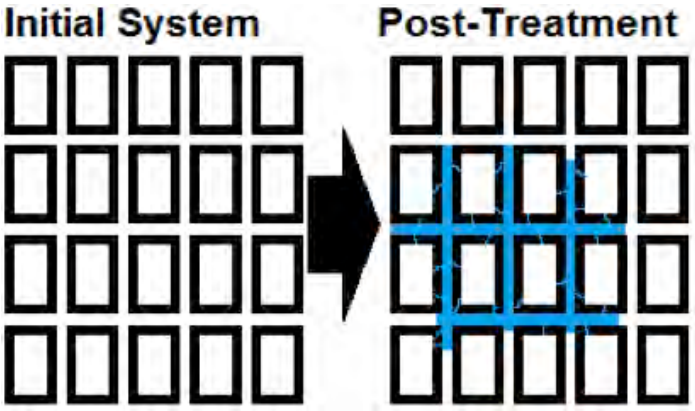

Figure 1: The hydraulic fracture (represented in blue) grows through the fracture cells (represented by gaps between the black boxes). The fracture can also improve communication between the matrix and fracture cells sharing a grid block (represented by the blue cracks formed in black boxes).

Each cell is assigned the permeabilities, kx, ky, and kz, in the X, Y, and Z directions. Permeability values of a cell can increase by the user as a function of the effective stress of the cell. As water is injected into a cell, the permeability values can increase in the simulation.

The fourth property that can be increased during hydraulic fracturing is sigma. Sigma is a mathematical representation of fracture density. Although a fracture cell in a simulation has enhanced directional permeability, it may not appropriately drain the matrix cell it is attached to. Sigma controls how well that fracture cell will drain that matrix cell.

With the directional permeabilities and sigma, it is possible to control the extent and intensity of a hydraulic fracture treatment independently. Because of this, independent control mechanism of the dual porosity approach is favored in this simulator.

2.2 Shear and Tensile Failure

The ability to control independently the extent and intensity of a hydraulic fracture separately allows for setting up a model that can simulate a combination of simple (tensile failure) and complex (tensile and shear failure) cells in an SRV after stimulation. Figure 2 shows a large number of small fractures and would be represented by a high sigma value but not much increase of the directional permeability. Figure 3 shows a large tensile fracture breaking through the same rock and would be represented by a large increase in directional permeability but would not increase significantly the sigma value.

The relative number of cells undergoing complex failure compared to simple failure in the SRV that a well generates has significant implications for its long-

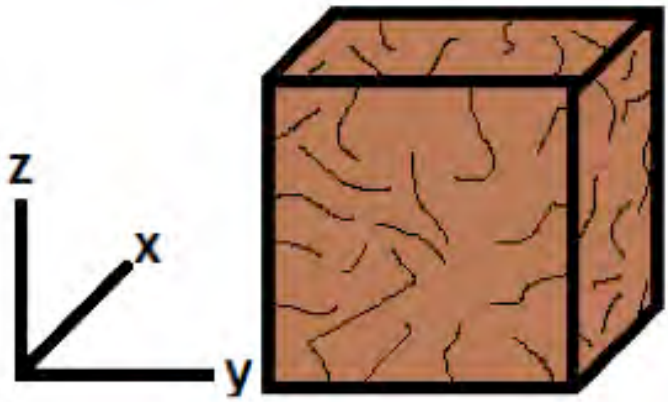

Figure 2: Shear failure in a cell can be thought of as a large number of smaller breakages.

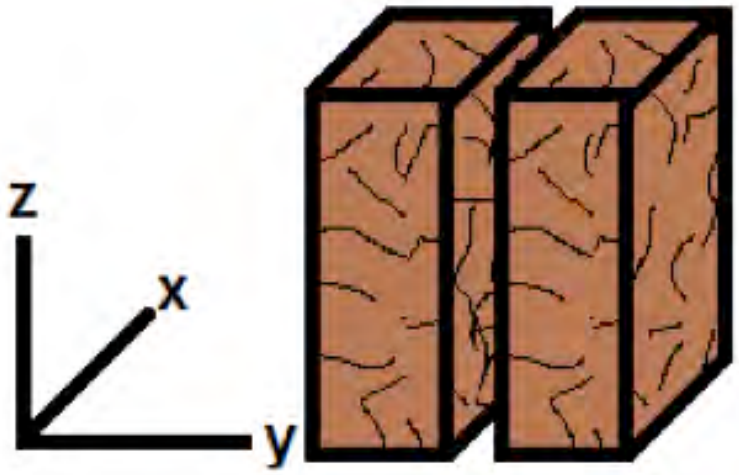

Figure 3: Tensile failure, or dilation, can be thought of as a few larger and planer breakages.

term production potential. Complexity generates long term production as the matrix cells contain the vast majority of the pore volume. The simple failures are only useful to act as highways for that production to get to the wellbore. A large shift to slick water and away from gels has been a result of the realization, because slick water promotes complexity.

2.3 Closure

Obviously, if every cell opens easily then it would be easy to work with unconventional reservoirs. After completion the hydraulic fracturing treatment has created a fracture system that is capable of absorbing 90+ bbls/minute of fluid per stage, but no well that required stimulation has ever been that productive. User can specify at least two paths to close the simulated fractures through the same user-specified table.

Depending on the complexity (the level of sigma) formed in each simulated cell and the placement of proppant, there can be multiple closure values for all four variables (kx, ky, kz, sigma). This allows simulation of very complex scenarios. Figure 4 shows a

simplified view of what one such table might look like in an easy to digest format. Note that the final permeability of the cell, in this case, is higher than the initial permeability whether it is propped or unpropped. This is a user choice. Curves in the figure may be extended further left into the depleted pressure, higher stress, area. The permeability would continue to decrease with pressure depletion. It should also be noted that the idea of closing sigma is a little strange. While fractures can close all the way in soft rock, usually there will be some remnant of the damage. It's more effective to instead assign the matrix (unconnected porosity) to its own closure table to reduce its internal permeability as a function of pressure. The transfer function between the fracture and matrix cells is only dependent on sigma and matrix permeability irrespective of whether the matrix cell is downstream or upstream in the flow sense. This prevents injection of gas or water from immediately re-opening the communication between the fracture and the matrix, as the gas has to get into the matrix to improve the matrix pressure and permeability to improve its communication.

2.4 Pore Volume

Porosity of the simulated cells is altered similar to the permeability. The porosity compressibility terms vary as a function of stress, not the porosity directly. The large tensile fractures are created if the pore volume compressibility reaches its maximum value. On the downward trend, the damage caused by hydraulic fracturing results in imperfect closure of porosity. The separation between the opening and closing pore compressibility curves results in residual porosity even if the ultimate compressibility values converge. Figure 5 illustrates these variations.

Both opening and closing tracks of pore compressibility can be varied at the cell level. This is also the term that controls how large the ultimate SRV becomes. It is helpful to think about two extreme every day materials: rubber and glass.

Figure 6 shows a hydraulic fracture grows long because the glass does not deform, and its brittleness favors growth of matrix fractures. Figure 7 shows how rubber easily balloons around the injected water and does not require the fracture to keep growing outwards. The glass will also not heal very well afterwards while the ductility of the rubber allows the cracks to close back up. Identifying which rock types in the reservoir act more like the glass and which more like the rubber helps select landing zones and vertical offsets.

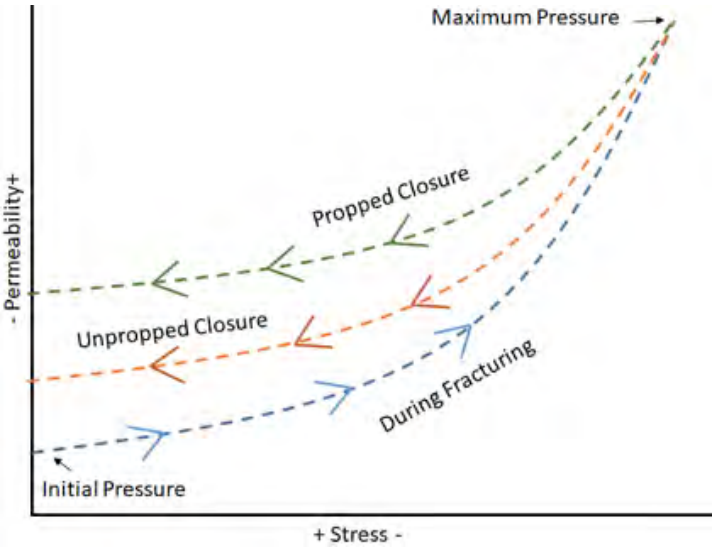

Figure 4: Opening and closure of a fracture and associated permeability during hydraulic fracturing.

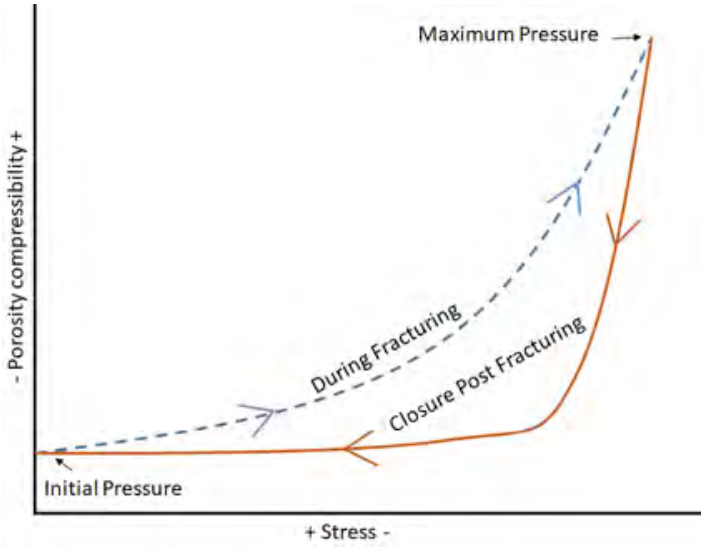

Figure 5: Pore compressibility varies as function of stress and whether the rock is opening or closing.

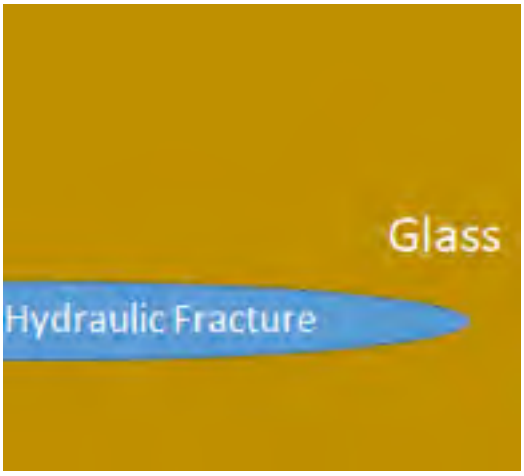

Figure 6: A hydraulic fracture is not accommodated by glass and has to grow large.

2.5 SRV Generation

The reported fracture treatment is converted into a simulation schedule deck along with the production data. During the injection part of the simulation run, the SRV is developed inside the simulator, as at initial time the model is effectively blank. If another well is drilled into the same section undergoing hydraulic fracturing, that treatment can also be incorporated into the simulation run. The frac hit, the impact of the existing well depletion, can be incorporated in the same model.

In the following figures, only the simulation cells with a sigma above the natural value are shown to represent an SRV. A filter in the post-processor ignores any cell blocks with a sigma below a user defined cut-off. Figure 8 shows the entire model after the first frac stage. Figure 9 shows the model with a filter for sigma values after the first frac stage. Figure 10 shows the model with a sigma filter after the final fracturing stage, but before production begins. This is a Three Forks well in which the well did not align with the primary stress directions, so the grid is inclined relative to the wellbore.

Figure 11 shows the SRV at the end of hydraulic fracturing from the top. Figure 12 shows the cross-sectional view of the SRV at the end of hydraulic fracturing. The extra bright circular zones more towards the heel represent the fracture growing into a brittle layer right above the target zones.

There is an important caveat here. This is just one way to look at what an SRV is. In this case, because we are looking at sigma, this is a snapshot of the complex SRV. One can also create an image of the SRV with the extent of the tensile failures, or, one can also let the model drain and show what the 'effective' SRV is both in the matrix and fracture cells. For the purposes of how ultimately productive a well ends up, the effective SRV in the matrix is the most important SRV. For understanding whether there is a frac hit, the tensile SRV is most important.

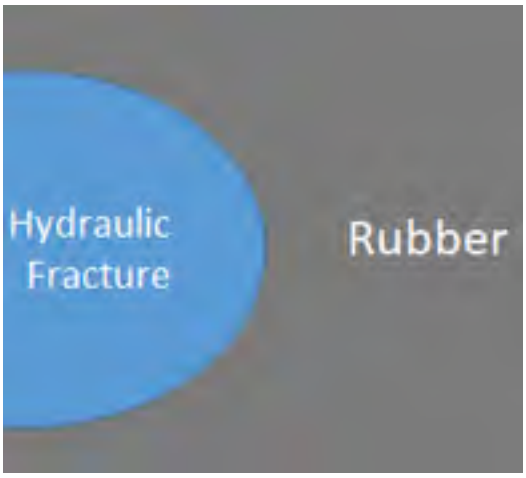

Figure 7: A hydraulic fracture is accommodated by rubber and does not have to grow large.

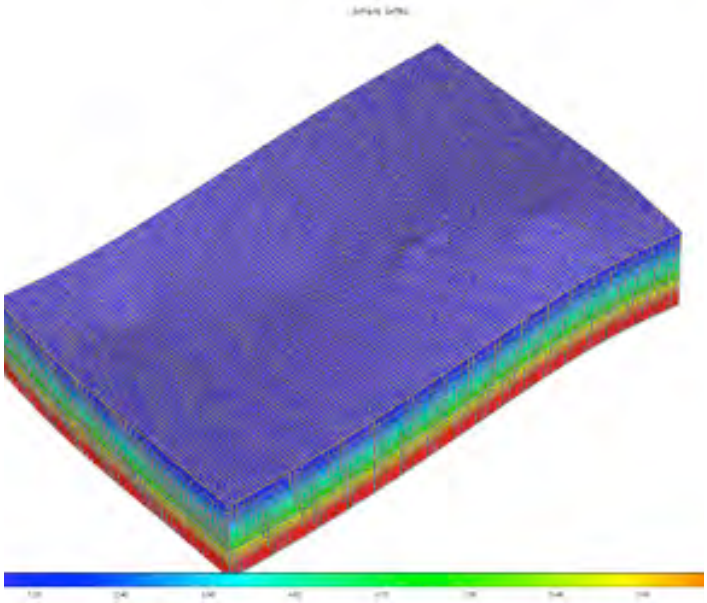

Figure 8: Simulation model after first stage with no filter

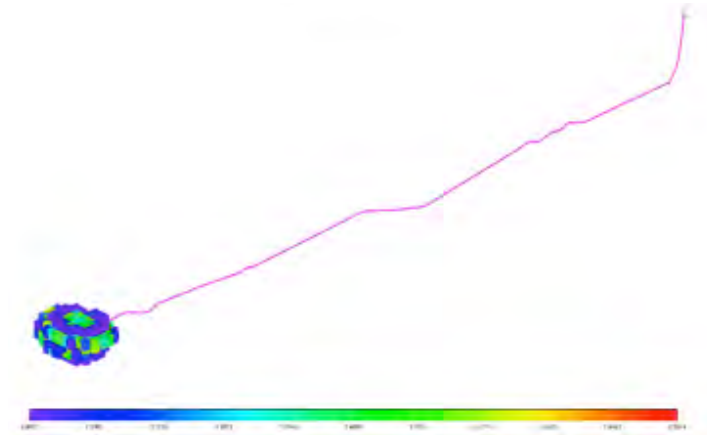

Figure 9: Simulation model after first stage with filter for minimum sigma value

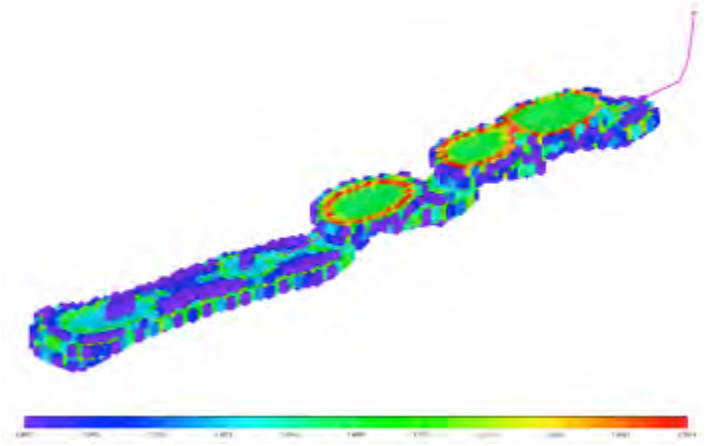

Figure 10: Simulation model after final stage with filter for minimum sigma value.

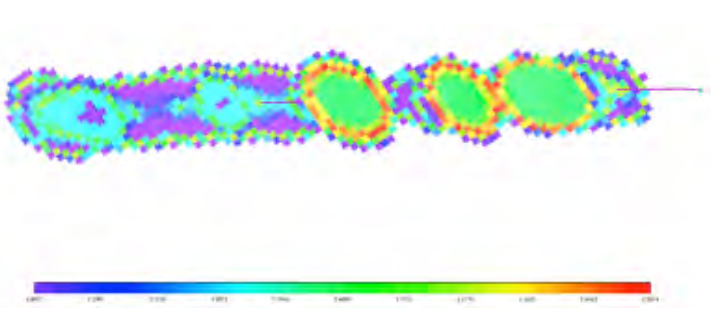

Figure 11: View of generated SRV from the top at end of hydraulic fracturing. Heel is on right.

3. Interference

One important point in the unconventional reservoir world has been how to avoid fracture interactions between wells, or frac hits. An attempt will be made here to show how the tools listed in here can be used to model these events.

3.1 Frac Hits

There has been a growing public understanding of fracture hits [7]. This is a term that has a rather ambiguous meaning when used casually because it represents a variety of events. At the most basic level, it is when an existing well sees a pressure increase or flush of liquid from a neighboring well being hydraulically fractured. Existence of these events has made some push the idea that the goal of completion design and well spacing should be to avoid these events entirely.

However, not all fracture hits are destructive to the well receiving the hit. Wells will typically have much larger tensile SRVs than complex SRVs. Rather, while simulating the well treatment, a large cloud of cells in the simulation shows enhanced directional permeability values but little to no sigma enhancement. The generation of this cloud in these cells will easily indicate the fracture hits observed in the field in the simulator. However, to space the wells based on this tensile cloud would leave matrix rock between the wells undrained. If the tensile fractures close, then the wells will not see each other after the fracturing treatment. If the tensile failures do not close then the wells may see some pressure communication in the future.

Now if the wells are close enough so that the complex SRVs overlaps, then it would indicate a negative impact on well productivity. There is a small caveat here that if the wells are vertically offset and there is a ductile layer between them, then the ductile layer may act as a drainage barrier. Hence, even if the wells do generate overlapped complex zones, they may not be able to fully drain individually what they generate. There will be further discussion on fracture barriers later in this paper.

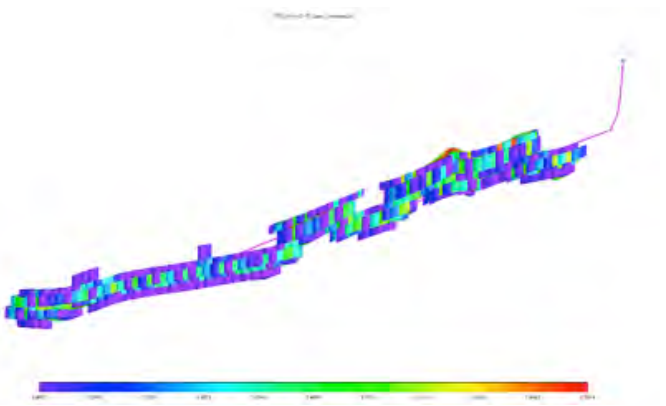

Figure 12: Cross sectional view of generated SRV at end of hydraulic fracturing. Heel is on right.

Between these two extreme—the overlapping complex SRVs or only the overlapping tensile SRVs—a number of physical scenarios may be happening.

If the tensile fracture clouds sufficiently overlap and the existing well has been on production, energy from the fracture treatment will escape into the depleted region. That energy goes to refilling the depleted zone instead of growing fractures. Hence, the treatment of the new well will be less effective. A numerical flow simulator almost by definition captures this. There are also a number of stress effects that can come into play here to further damage the new well.

Figure 13 shows three scenarios. One in which the wells are drilled far enough apart to not experience any frac hit is shown. They also do not properly drain a vast volume in between them. A second scenario with overlapping tensile clouds is shown that do experience frac hits but also do not significantly interfere with each other. Lastly, a case where the wells are drilled too closely and will have significant negative impact is shown.

If the fractures zone of a new well intersects the fractured zone of the original well, it may have enough pressure to dislodge proppant from the older well. A numerical simulator can also handle this as the proppants are treated as a tracer in the fracture cells with certain rules about when they can move. As discussed earlier, once a cell is unpropped it can experience more significant permeability closure.

When the pressure of a depleted existing well is spiked by the frac hit, it can force free gas back into the oil phase; in a sense, resetting the bubble point with a new composition based on the existing dead oil and what free gas was available. When gas-oil ratio (or GOR) drops following a frac hit, this is likely the culprit and is by definition modeled by a flow simulator. This effect is what they were designed to model in conventional water and gas flooding.

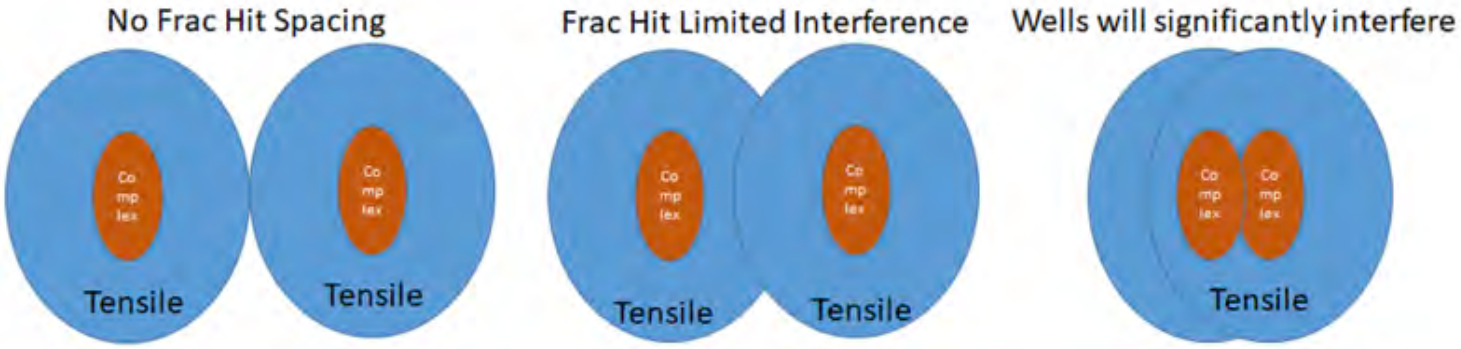

Figure 13: Gun barrel views of different spacing scenarios for two wells.

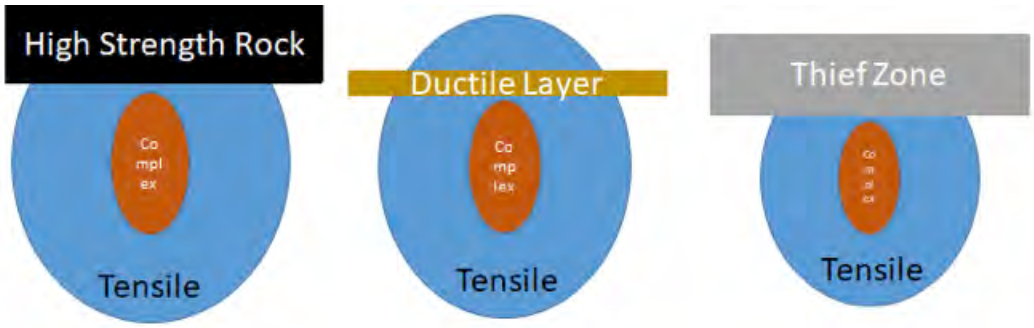

Figure 14: Three barrier situations

3.2 Frac Barriers

Barriers to fracturing, on its face, should be an easy to define term. However, in reality, several phenomena are loosely grouped together.

The most obvious definition of a frac barrier is a layer of rock that is strong and, therefore, fractures can't grow into them. For example, a layer of dolomite lying over a layer of mudrock would be a frac barrier. The fractures would rather continue growing into the mudrock. A numerical simulator with the options listed before the minimum stress of that dolomite layer would be increased to represent how hard it is to penetrate it. If such layers exist in your reservoir then planning well placement can benefit from that strong rock.

In practice, a ductile layer can be just as effective as a hard rock to act like a vertical flow barrier. The fractures may still penetrate through this ductile layer, but if they close after treatment is completed, then wells placed on either side will not be able affect each other. Fracturing energy will also not be wasted as if a fracture passes through this ductile layer. It will create a fractured zone on the other side for another well to possibly benefit from. These layers can be assigned high permeability closure values separately from the other layers to make them act as a tight seal in the simulator.

There can also be "thief" zones, not truly a frac barrier or a ductile layer. This may be a sandstone deposit that has been previously drained by a vertical well. The depleted high permeability rock can absorb the energy from the treatment and be difficult to pass through. These zones are the most difficult to identify, especially in playas with a long history of vertical development. Thief zones can be represented in a numerical simulator by either manually inserting vertical wells or by initializing the simulation with low pressure high permeability pockets.

Figure 14 demonstrates the three scenarios above. A thief zone will decrease the ability to generate large SRVs while a strong barrier transfers the energy to more useful places. A ductile layer does neither but instead locks away part of the SRV after treatment is complete. There may be other scenarios than the ones listed above but identifying which are important to a specific playa can help optimize the design.

Conclusions

A large variety of playas have been modeled successfully using the techniques above. This is still a developing work flow and technology; for instance, the stress solution has been recently added to further enhance the models. Landing zone studies, staggered spacing studies, and Enhanced Oil Recovery or

EOR studies have been completed with this simulator used in creative ways to capture the different hysteretic events that occur when there are a dozen of staggered wells interacting over several years. Lessons learned from these studies have been applied and with positive impact. No simulation is perfect and there is still a lot to learn and to do. But by simulating and trying to capture the events, it is possible to better understand the phenomena occurring to make better decisions.

References

1 Cipolla, C.L., E.P. Lolon, and M.J. Mayerhofer. 2009. Reservoir Modeling and Production Evaluation in Shale-Gas Reservoirs. International Petroleum Technology Conference, Doha, Quatar, 7 – 9 December 2009.

2 Yin, J., J. Xie, A. Datta-Gupta, and A.D. Hill. 2011. Improved Characterization and Performance Assesment of Shale Gas Wells by Integrating Stimulated Reservoir Volume and Production Data. SPE Eastern Regional Meeting, Columbus, Ohio, 17 - 19 August 2011.

3 Petunin, V.V. 2013. Finite Difference Approach to Modeling Geomechanics in Hydraulic Fracturing. 47th U.S. Rock Mechanics/Geomechanics Symposium, San Franscisco, California, 23 - 26 June 2013.

4 Carroll, M.M. and N. Katsube. 1983. The Role of Terzaghi Effective Stress in Linearly Elastic Deformation. J. Energy Resource. Tech., Volume 105, 509–511.

5 Warren, J.E. and P.J. Root. 1963. The Behavior of Naturally Fractured Reservoirs, Soc. Pet. Eng. J., Volume 3, Number 3, 245–255.

6 Kazemi, H., L.S. Merril, K.L. Porterfield, and P.R. Zeman. 1976. Numerical Simulation of Water-Oil Flow in Naturally Fractured Reservoirs. Soc. Pet. Eng. J., Volume 16, Number 6, 317–326

7 Daneshy, A. 2019. Horizontal Well Frac-Driven Interactions: Types, Consequences, and Damage Mitigation. Journal of Petroleum Technology¸ Volume 71, Issue 6.

Organic Maturity and Richness Impact on Geomechanical Anisotropy in Unconventional Reservoirs

Submitted by Azra N. Tutuncu and Binh Bui, Petroleum Engineering Department and Unconventional Natural Gas and Oil Institute (UNGI), Colorado School of Mines.

Introduction

Shale formations are highly sensitive to stress and fluids they are exposed to. Shales are heterogeneous and anisotropic formations. Moreover, their source rock characteristics also introduce further complexity with the organic matter and compositional variations across the area of the reservoirs. The level of maturity of the organic matter requires further understanding of the alterations introduced in the organic matter distribution and associated changes encountered in the deformation and flow characteristics of shale formations. One of the critical aspects of the presence of organic matter is the quantification of shale mechanical properties and their direction dependence, which is necessary for successful field development. The mineralogical composition of shale typically deviates from carbonate-rich to quartz-rich rock matrix, with clay and organic matter heterogeneously distributed in the reservoir. The layered structure introduced by the depositional history of the formation along with the heterogeneity in the distribution of organic matter results in anisotropic variation of associated reservoir properties. Consideration of these factors in exploration studies – in conjunction with seismic attributes, reservoir characterization, drilling and hydraulic fracture design and production optimization – is key to success in field operations. (Sondergeld and Rai 2011; Vernik and Milovac 2011; Tutuncu et al. 2016).

The organic matter in shale is typically highly heterogeneous at a submicron scale; this may result from the distinct differences in the deposited organic matter and local variations in the extent of thermal alterations. The SEM and FTIR nanoscale investigations provide high-resolution views of the pore structure and secondary pores created within the organic matter during the thermal processes. These investigations typically do not provide any information on the type, chemical composition, and mechanical properties of the organic matter. Rock evaluation analysis is a type of macro analysis that does not provide assessment of heterogeneity at small scales essential for better understanding of the coupled geomechanical and flow characteristics of the formation. Such analysis is important to an optimized production and to determine the sweet spot in the large extent of the reservoir area.

The natural processes creating these variations require millions of years to convert organic matter into oil and gas, with oil shale as the most immature source rock; it has been studied extensively to characterize unconventional resources and their production potential for several decades. For example, the variation in natural processes is seen in the Eagle Ford shale, which has oil, condensate, and gas windows resulting from taking the immature kerogen conversion to different levels of maturity of hydrocarbons in each window. Surface retort techniques have been utilized to convert kerogen into oil and gas in immature formations. The concentration and composition of organic matter during deposition and diagenesis in the source rock determine the hydrocarbon generative capacity of the shale. The amount of organic carbon is related to the total organic carbon (TOC) content of the formation, while the quality is attributed to the type of organic matter and its thermal maturity.

In this study, we present experimental results on the impact of organic matter and maturity. Core samples from several shale formations have been selected to study the maturity variation. The samples from all formations were measured under triaxial stresses at ambient temperature to 40°C to determine the static and dynamic moduli using simultaneous measurements of the geomechanical and acoustic properties. In addition, several Green River oil shale samples were heated to higher temperatures to determine the alterations of the geomechanical and acoustic properties and anisotropy at different maturity levels for an approximately fixed mineralogy. The well logs from the same wells from which the cores were obtained have been used to determine the dynamic and static properties and organic matter contents as a function of depth to investigate the role of organic matter on the mechanical and acoustic properties of the shale reservoirs. The effects of composition and fabric on the mechanical properties have also been included in this investigation.

Experimental Study

Core samples from the Eagle Ford, Niobrara, Bakken, and Green River shales were used in this study. The Eagle Ford formation is a Late Cretaceous age depositional system underlying much of South Texas, extending from outcrops in West Texas to North East Texas. The formation has rich carbonate with high shale content increasing from south to northwest. The Niobrara has higher clay content and contains natural fractures with cyclic-bedded chalk, marl, and calcareous shale, and limestone mixtures with varying organic matter distribution and reservoir quality in various sections of the formation. Thin bentonite beds clearly visible in the cores are deposited between shale and chalk layers (El Ghonamy and Sonnenberg, 2015), yet are difficult to detect in well logs. The swelling of the beds creates stability issues during drilling, hydraulic fracturing and production.

The Bakken formation overlies the Upper Devonian Three Forks formation.

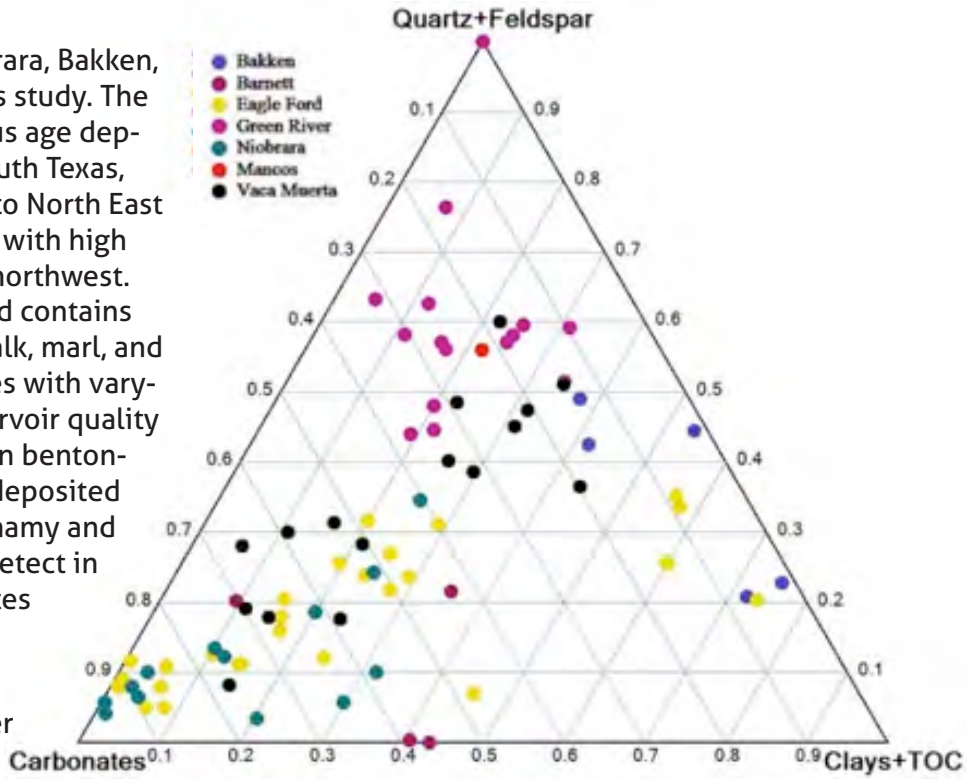

Figure 1: Mineralogical composition of the formations studied.

Near the center of the Williston Basin, the formation is commonly divided into three members: upper shale, middle siltstone, and lower shale.. Those three members can be correlated regionally, with most thickness changes taking place in the middle siltstone member, where core samples were collected for this study. The Bakken formation has very similar lithologies in the upper and lower members throughout the basin and consists of brittle, black-dark brown shale composed mostly of indistinct organic material with lesser amounts of clay, silt, and dolomite grains. The lower Bakken shale has less-organic content and more clay-rich, silty, and dolomitic near the flanks of the basin. The middle Bakken siltstone fluctuates between a medium-gray, dolomitic, fine-grained siltstone and a very-silty and fine-crystalline dolomite (Meissner 1991).

The Green River formation has been studied for many years for developing technologies to unlock the immature resources in the oil shale formation. The formation deposited in the Piceance Creek, Uinta, Greater Green River, and Washakie Basins extends to parts of Colorado, Utah, and Wyoming. The deposits in Piceance Creek basin have higher organic content than in other basins.

Mineralogical composition of the studied formations varies and impacts the measured properties.

The Eagle Ford formation has significantly higher carbonate content compared to the Vaca Muerta, Bakken, Niobrara, and Green River shale reservoirs.

TOC and clay content were combined as ductile component as shown in the ternary diagram (Figure 1) to emphasize the role of mineralogical content in the mechanical properties and strength.

The preserved core samples were measured at various stress conditions with coring direction vertical (0°) and horizontal (90°) to the bedding to investigate the influence of stress and lamination orientation on the mechanical and acoustic properties, porosity and permeability. Mechanical properties were measured at the in-situ stress from 6 to 24 MPa followed by failure tests to determine the strength. Two vertical and three horizontal core samples from the Green River oil shale with varying TOC were measured under confining stress state pre- and post-pyrolysis to study the maturation effect on similar lithology. The dry pyrolysis takes several hours under small pressure and elevated temperature. This was utilized for most samples while limited samples were also tested using hydrous pyrolysis. The difference between the pyrolysis processes is discussed in detail by Lewan and Cox (2008).

We initiated our experimental study at room temperature using the Green River immature cores. Both dry and hydrous pyrolysis were conducted at various temperatures to obtain specific maturity samples for testing their mechanical properties and strength at various maturity levels. These tests were conducted before conducting tests with other mature shales

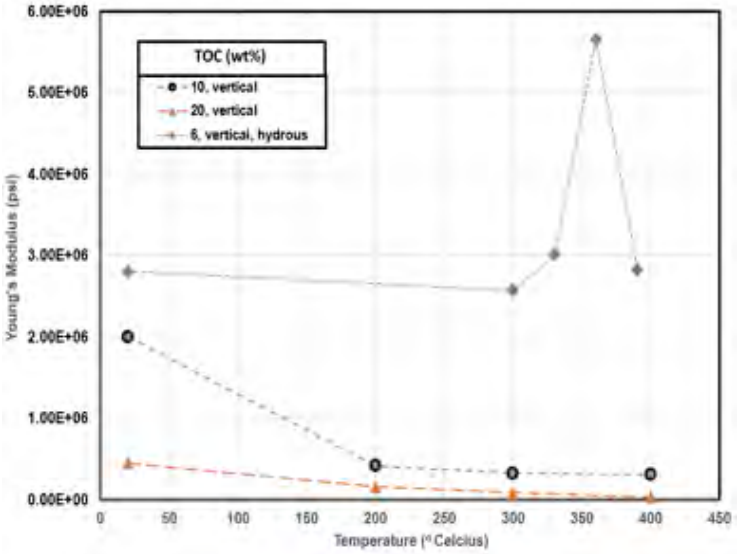

a. Static Young's Modulus.

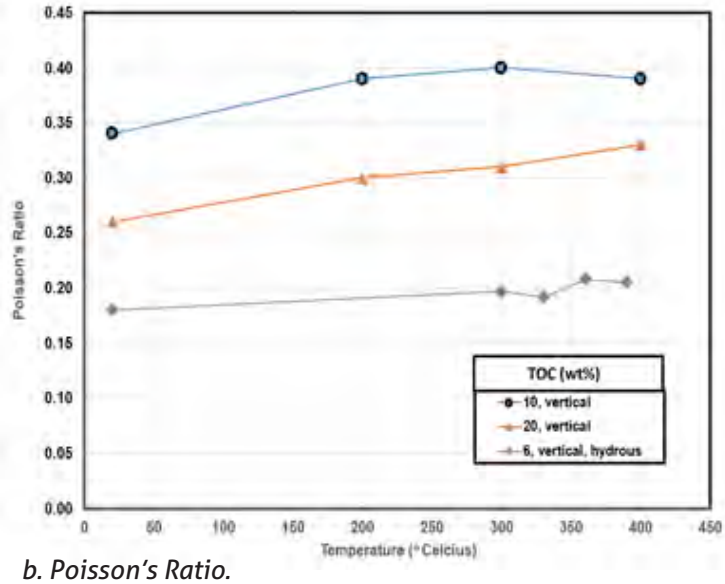

b. Poisson's Ratio.

Figure 2. Static Young's Modulus and Poisson's Ratio as a function of pyrolyzation temperature for the Green River immature shale samples.

from the oil windows of the Eagle Ford, Bakken and Vaca Muerta shales at 40°C. The variation in mechanical properties (Young's modulus and Poisson's ratio) as a function of increasing temperature from these measurements is shown in Figure 2. In a recent UNGI collaborative research study with the USGS, we had the opportunity to test the difference between hydrous and dry pyrolysis in oil shale core samples. Our analysis using multiple tests indicated that there was less impact of maturity in confined hydrous pyrolysis than in the dry pyrolysis with visible fractures present in post-pyrolysis samples and decreased mechanical properties and strength with maturation.

At constant confining pressure of 1000 psi (7 MPa), triaxial compressive strength at constant confining pressure of 1000 psi decreases as a function of increasing TOC (Figure 3). The Unconfined Compressive Strength (UCS) of the intact (unpyrolized) Green River samples were in the range of UCS reported by Tutuncu (2010). The Young's modulus indicates a significant reduction at high temperature before the failure occurs. The Poisson's ratio increases showing the softening of the samples at higher temperature.

Laboratory measurements of shale at different maturity and compositions indicate that deformation characteristics are strongly dependent on mineralogical composition, porosity, clay content and maturity. The impact of richness of organic matter on geomechanical properties depends on their thermal maturity. In immature shales, especially in the Green River shale investigated in our research, increased TOC results in a reduction of formation strength as the result of the ductility of the organic matter and the introduction of natural fractures at the early maturity stages. In higher maturity shale reservoirs, TOC effect on strength is reduced due to the expelled hydrocarbons, converted bitumen filling connected organic pore space reducing load bearing characteristics and the residual kerogen becoming stiffer. Therefore, the effect of organic matter on geomechanical properties in higher maturity shales is not apparent.

The distribution of clay and organic matter determines the level of elastic anisotropy in shale reservoir formations. The kerogen maturity and bedding orientation are among the key variables controlling mechanical anisotropy, stiffness, and strength. The local tectonic history also affects the elastic properties of shale formations. The relationship among elastic anisotropy, clay, and kerogen content indicates that as the amount of clay and kerogen increases elastic anisotropy increases. Presence of clay particles increases the directional stiffness of the formation especially in higher compressibility in the direction normal to bedding while stiffer response parallel to the bedding occurs. Kerogen also has a similar impact on the anisotropy with a strong dependence on kerogen maturity (Vernik and Nur 1992).

The chalk intervals in Niobrara are isotropic, on the contrary to be the fracture barriers. The marl intervals indicate strong anisotropy providing accurate determination of the critical minimum horizontal stress to be used for safe hydraulic fracturing operations. The significantly lower Poisson's ratio for the marl samples was also reported by other experimental studies (Maldonado 2011; El Ghonamy and Sonnenberg 2015). This is interpreted as large pore space filling by highly oriented clay minerals, causing stiffer matrix as also discussed by Revil (1999). For the D marl samples, the Poisson's ratio of vertical and

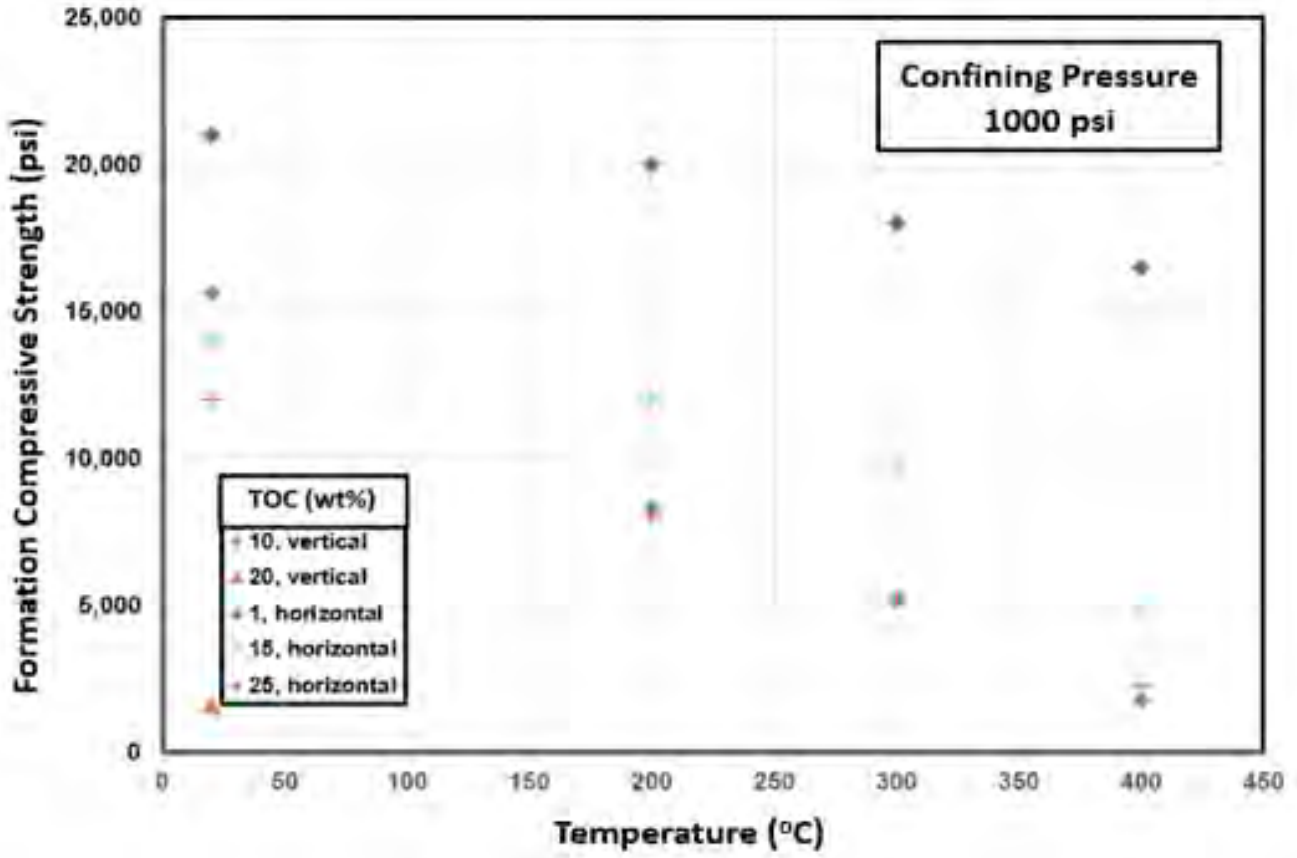

Figure 3: Formation strength as a function of increasing pyrolyzation temperature (different maturity) for Green River immature shale samples under 1000 psi (7 MPa) confining pressure.

45-degree samples ranges between 0.10-0.15 and 0.11-0.16, respectively when axial stress varies from 8 to 42 MPa. The increasing stiffness with respect to bedding angle is again observed as the horizontal Poisson's ratio ranges between 0.15-0.17 throughout the experiment.

Maturity Effect on Anisotropy

Increasing the temperature results in the transformation of kerogen into dead carbon, liquid, and gaseous hydrocarbons as reaction products. Maturation starts with the burial and compaction of sediments containing organic carbon, and occurs during this diagenesis. Methane is produced through biologic activity. When a formation is buried deep enough for temperature to reach 50°C to 150°C, catagenesis takes place for the oil and most of the wet gas windows of the reserves. With temperature increasing to 150° –200 °C, metagenesis produces dry gas (methane and CO_2) and graphite as byproducts.

The level of maturity impacts the porosity within the organic matter, resulting in the variation observed in the geomechanical, petrophysical and acoustic anisotropies as well as wettability. Anisotropy has a complex variation, with maturity first increasing from immature to early mature stage, then reaching the maximum value at peak maturity. Gas saturation increases as the result of the hydrocarbon converting into gas. In the post mature stage, a decrease in anisotropy is observed when hydrocarbons are expelled out of the macro and micro pore space and some level of nano-scale compaction takes place.

Passey et al. (1990) used porosity and resistivity logs to calculate TOC over the reservoir interval where separation of the two logs was observed. Sonic logs were preferred in their analysis due to the less effect of the borehole conditions compared to the neutron logs. The separation between the two curves has been empirically derived using Equation (1). Determination of TOC in the organic-rich zones depends on the Δlog R; the level of maturity of the organic matter (LOM) is also critical in this calculation as noted in Equation (2).

$$\Delta \log R = \log_{10}(R/R_{baseline}) + SF(\Delta t - \Delta t_{baseline}) \quad (1)$$

$$TOC(wt.\%) = (\Delta \log R) * 10^{(2.297 - 0.1688 LOM)} + \Delta TOC \quad (2)$$

where R is the resistivity in ohm-m; Δt is the measured transit time in μsec/ft., Rbaseline is the resistivity value corresponding to Δt values when the curves overlie and is baseline in an organic-lean zone. The scaling factor SF is defined based on the ratio of resistivity logarithmic cycles over the porosity log scale. ΔTOC is the TOC regional background level in the shale reservoir that is difficult to determine. Passey et al. (1990) used 0.8 wt. % as the minimum TOC in shale reservoirs. (See Figure 4.)

The Δlog R technique is an empirical methodology requiring validation using core calibration. Log-derived TOC has a relatively low correlation with core measurements in intervals of low and very high TOC. This technique requires a baseline selection that is subjective and requires some level of expertise. Heavy minerals including pyrite and high carbonate content may affect resistivity logs, and this variation can vary with maturity. Therefore, it should be used with caution.

We used TOC calculations using density logs and velocity correlations discussed in detail in Tutuncu and Bui (2019) as wells used did not show any borehole conditions due to the use of oil base mud during drilling. A strong correlation between anisotropy, TOC and level of maturity was observed where modulus C_{ij} from different maturity reservoirs was evaluated. The static and dynamic stiffness tensors were calculated using Equations (3) through (7).

Due to the presence of clay minerals within the matrix and in the pore space, shale wettability may change as the result of the operations, when varying fluid composition may alter the equilibrium and initiate osmotic reactions on clays. In organic rich shale reservoirs, clays and organic matter co-exist -- complicating wetting preferential in the pore surfaces that impacts the connectivity of the pore space, i.e. permeability anisotropy as well (Figure 5). The core measurements and log data collected in the associated intervals confirm that Young's modulus and Poisson's ratio present strong anisotropy in the form of an exponential decrease of Young's modulus with increasing TOC, which is also correlated to Thomsen's (1986) parameters describing elastic anisotropy as shown in Figures 6, 7 and 8 (Tutuncu 2010; Tutuncu et al. 2016).

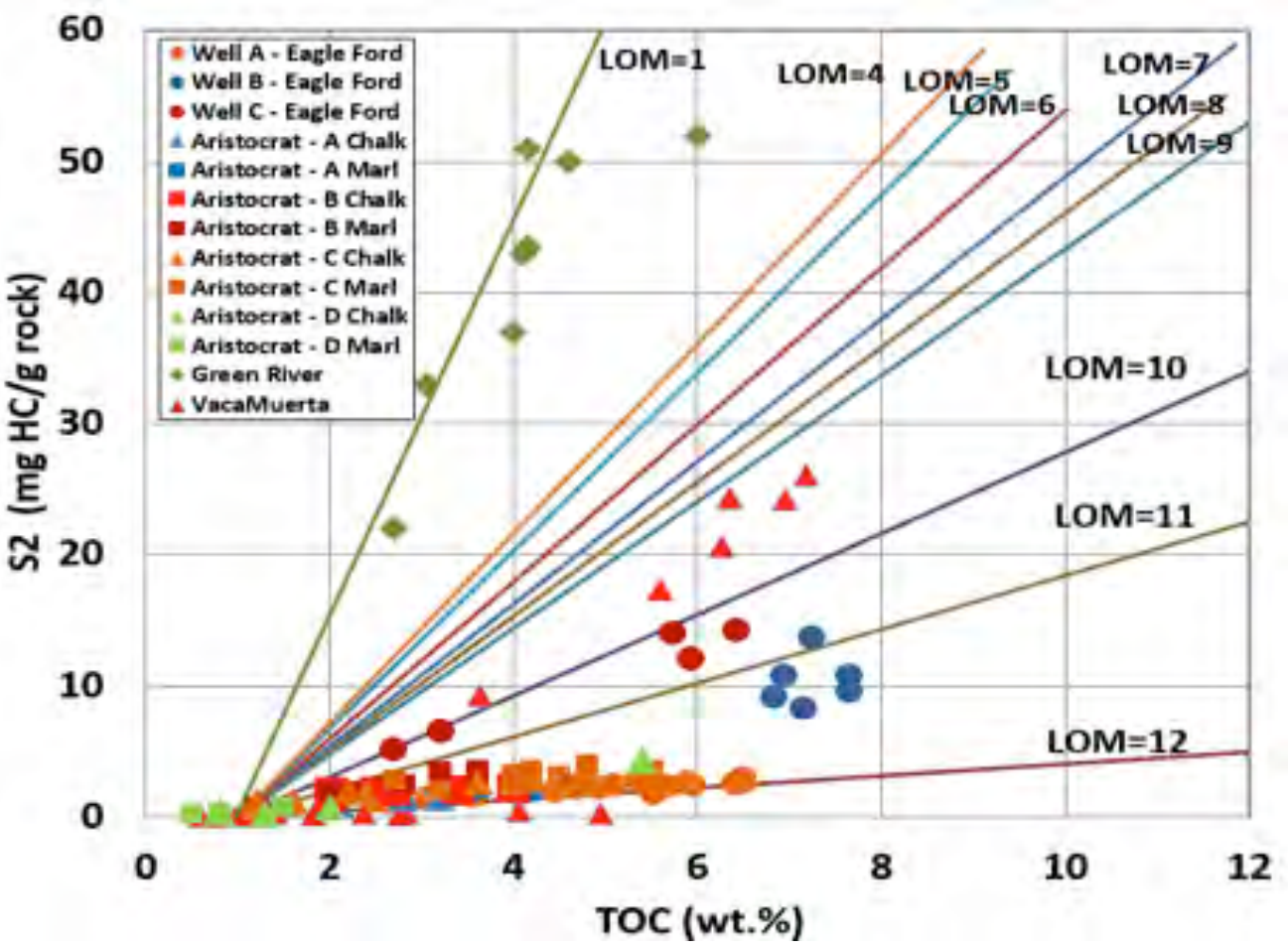

Figure 4: Level of maturity for Eagle Ford, Niobrara, Green River and Vaca Muerta wells using core measurements superimposed into the LOM diagram developed by Passey et al. (1990).

Static C_{ij}

$$C_{11} = \frac{E_h}{(1+\nu_h)(1-2\frac{E_h}{E_v}-\nu_v^2-\nu_h)}\left(1-\frac{E_h \upsilon_v^2}{E_v}\right)$$

$$C_{12} = \frac{E_h}{(1+\nu_h)(1-2\frac{E_h}{E_v}-\nu_v^2-\nu_h)}\left(\frac{E_h \upsilon_v^2}{E_v}+\nu_h\right)$$

$$C_{33} = \frac{E_v\,(1-\nu_h^2)}{(1+\nu_h)(1-2\frac{E_h}{E_v}-\nu_v^2-\nu_h)}$$

$$C_{44} = \frac{E_v E_h}{E_h(1+2\nu_v)+E_v}$$

$$C_{66} = \frac{C_{11}-C_{12}}{2}$$

$$C_{13} = \frac{E_v\,(1-\nu_h^2)}{(1+\nu_h)(1-2\frac{E_h}{E_v}-\nu_v^2-\nu_h)} \quad (8)$$

Dynamic C_{ij}

$$C_{11} = \rho_b V_{p11}^2 \quad (3)$$

$$C_{12} = C_{11} - 2C_{66} \quad (4)$$

$$C_{33} = \rho_b V_{p33}^2 \quad (5)$$

$$C_{44} = \rho_b V_{s31}^2 \quad (6)$$

$$C_{66} = \rho_b V_{s12}^2 \quad (7)$$

$$C_{13} = -C_{44} + \sqrt{4\rho_b V_{p45}^4 - 2\rho_b V_{p45}^2 (C_{11}+C_{33}+2C_{44}) + (C_{11}+C_{44})(C_{33}+C_{44})}$$

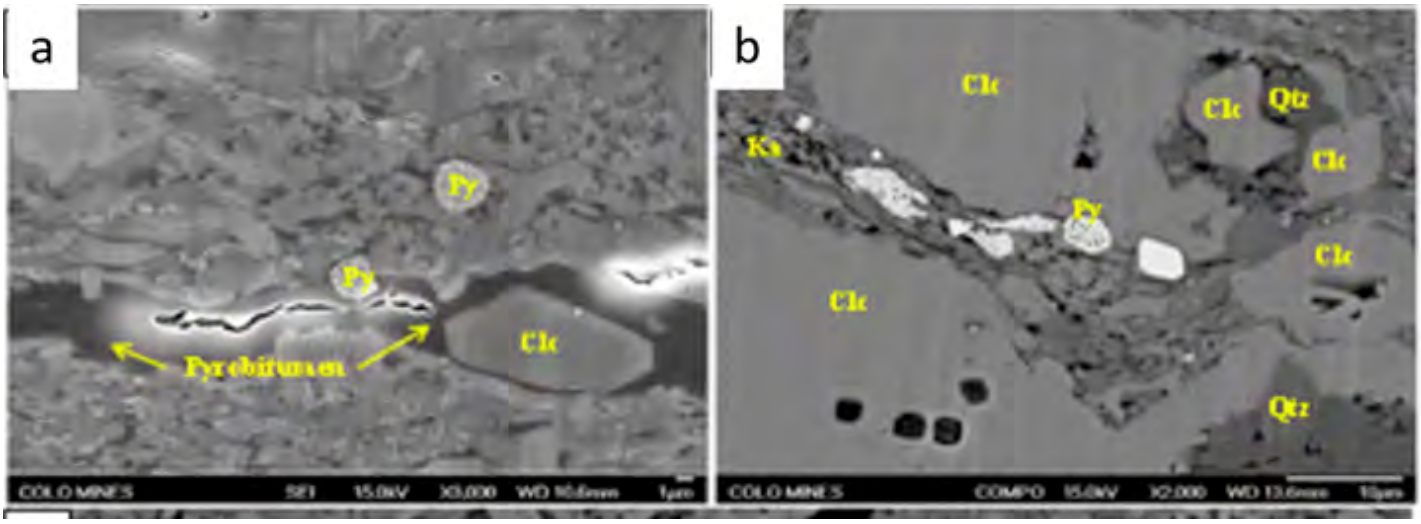

Figure 5: Organic matter distribution patterns in the upper Eagle Ford Formation. a) organic matter in a large accumulation; b) organic matter occupying the depositional pore space (Padin et al, 2014).

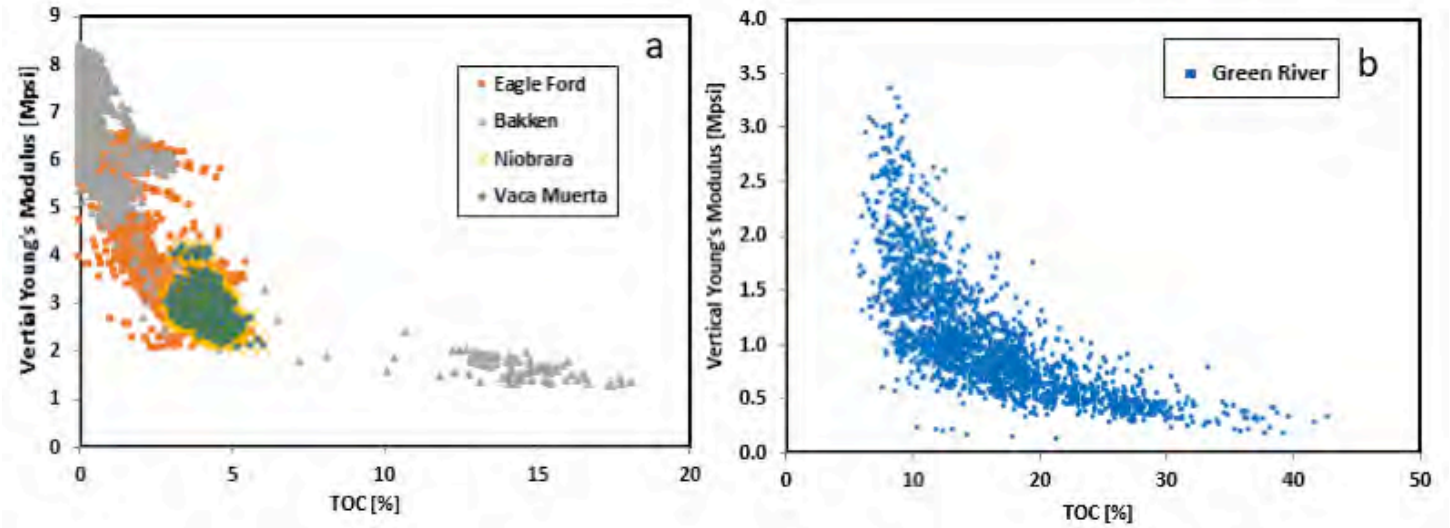

Figure 6: Vertical Young's Modulus as a function of TOC for a) mature and b) immature shale.

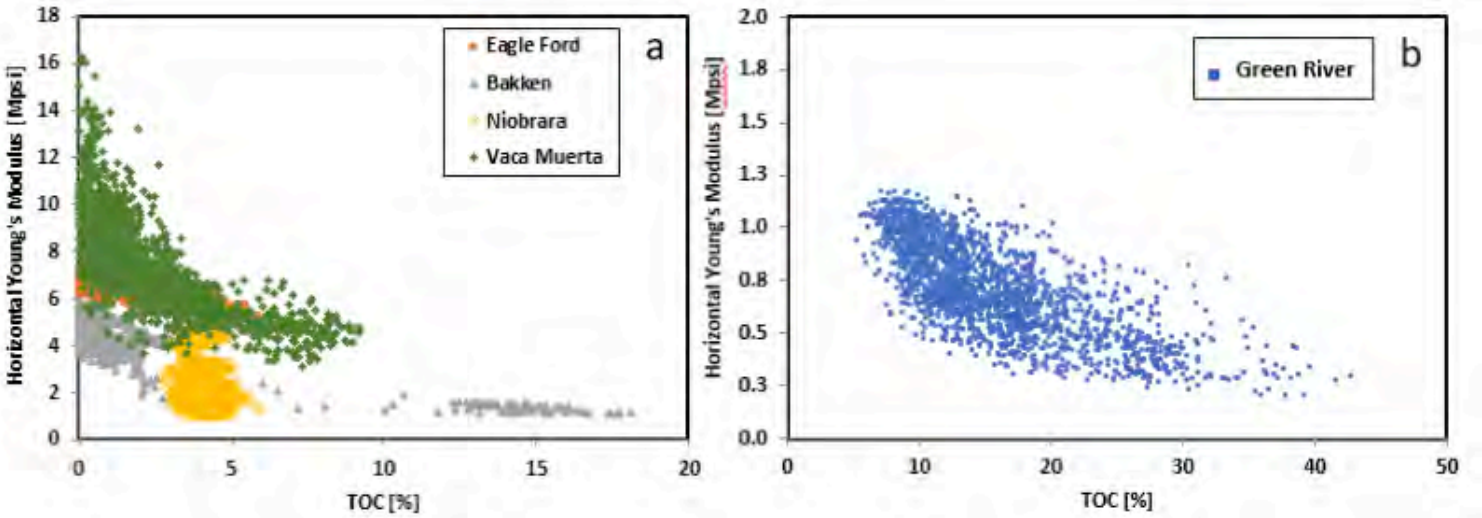

Figure 7: Horizontal Young's Modulus as a function of TOC for matured and immature shale.

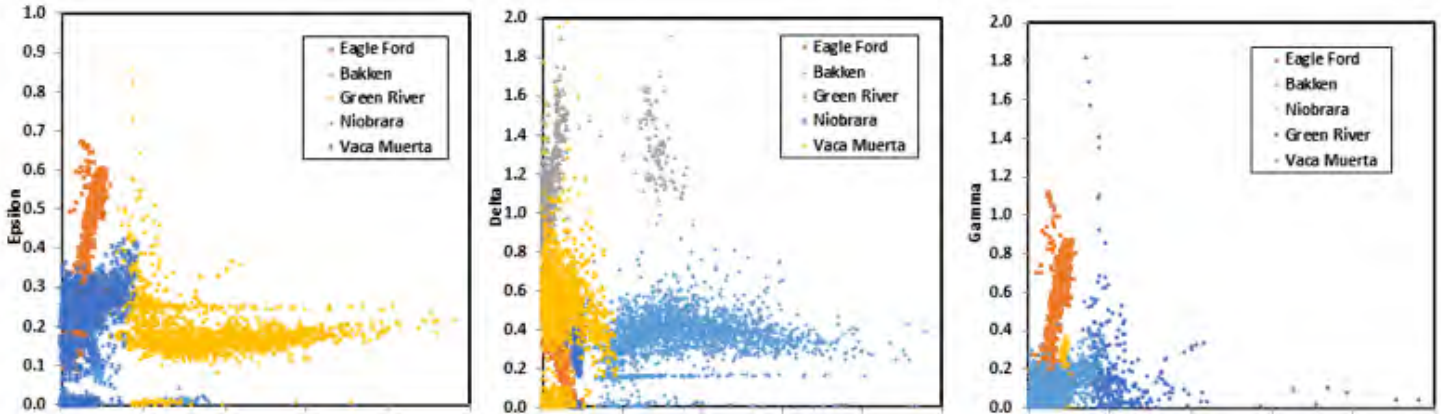

Figure 8: Thomsen coefficients for the studied shales.

Conclusions

Laboratory measurements on anisotropic shale samples with different maturity and composition show that the deformation characteristics are strongly dependent on mineralogical composition, porosity, clay content, and maturity. These parameters make a difference in the level of anisotropy observed. The impact of organic matter richness on geomechanical properties depends on their thermal maturity. In immature shales, especially in the Green River shale investigated in our research, increased TOC results in the reduction of formation strength as the result of the ductility of the organic matter and natural fractures introduced at the early maturity stages. In shale reservoirs with higher levels of maturity, strength reduction with TOC is because part of the organic matter is converted to bitumen that fills connected organic pore space and is no longer load-bearing. Some is cracked to hydrocarbon and expelled, and the residual kerogen has itself becomes harder. Thus, at high thermal maturities, the effect of organic matter on geomechanical properties is not evident.

Dipole sonic log and laboratory ultrasonic velocity derived C_{ij} coefficients indicate a strong dependence on the TOC and clay composition. Further research is in progress to enhance the understanding of nanopore structure and location of kerogen in the pore space and in matrix to the level of anisotropy, particularly for geomechanical property and strength anisotropy. We also observe that the stiffness of the studied shales significantly decreases as TOC increases. The typically used Thomsen coefficients show much weaker correlation than C_{ij} correlations to TOC. Therefore, we recommend considering C_{ij} to determine the level of maturation from acoustic data and seismic base interpretations.

References

El Ghonamy R.S. and Sonnenberg S. 2015. Statistical Methods of Predicting Source Rock Organic Richness from Open-Hole Logs, Niobrara Formation, Denver Basin, CO. SPE-178487, Proc. Unconventional Resources Technology Conference, San Antonio, Texas, USA.

Lewan M. and Cox D. 2008. Applying Hydrous Pyrolysis to In Situ Oil Shale Retorting. Proc. 28th Oil Shale Symposium, Colorado School of Mines, Golden, Colorado, USA.

Maldonado A. 2011, Elastic and Mechanical Properties of the Niobrara Formation with Application to Hydraulic Fracture Design, M.S. thesis, Colorado School of Mines, Golden, Colorado, USA.

Meissner F.F. 1991. Petroleum Geology of Bakken Formation Williston Basin, North Dakota and Montana, Montana Geological Society Publication.

Padin A., Tutuncu A.N., and Sonnenberg S. 2014. On the Mechanisms of Shale Microfracture Propagation, SPE-168624, Proc. SPE Hydraulic Fracturing Technology Conference, the Woodlands, Texas, USA.

Passey Q.R., Creaney S., Kulla J.B., Moretti F.J., and Stroud J.D. 1990, A Practical Model for Organic Richness from Porosity and Resistivity Logs: AAPG Bulletin, Vol. 74, 1777-1794.

Gouge Formation during Fracture Shearing and the Impact to Flow

Submitted by Magdalena Gill and Johnathan Moore, United States Department of Energy, National Energy Technology Laboratory, and Leidos Research Support Team, National Energy Technology Laboratory; and Dustin Crandall, Leidos Research Support Team, National Energy Technology Laboratory, (Morgantown WV).

Abstract

Gouge formation frequently occurs in fractures during shear due to the grinding of rock surfaces to small particulate matter. Recent studies at the National Energy Technology Laboratory (NETL) utilized a unique apparatus to look inside of fractured core undergoing shear deformation and evaluate the fractures' geomechanical evolution, while measuring changes to the permeability through the fracture. Two examples of these studies are described in detail illustrating the impact of sample heterogeneity on the creation of gouge in fractures. It is hypothesized that microfabric variation of rocks has a significant impact on gouge formation.

Introduction

Unconventional shale reservoirs are characterized by extremely low matrix permeability, hence fractures play a critical role in oil/gas migration from the reservoir to the well. Fractures are localized flow pathways with permeabilities that are orders of magnitude higher than the surrounding rock matrix. Subsurface engineering activities, such as hydraulic fracturing, create a significant number of fractures in stimulated formations, but also induce imbalances in the local stress regime that can cause shear slippage of existing fractures.

Shear deformation of fractures can drastically influence their permeability. As the opposing rough-walled fracture faces translate against each other, asperities can touch, increasing the mean aperture and permeability of the fracture. Conversely, asperities can break during this shear translation, creating dislodged material that gets ground down during further shearing and forms low permeability gouge inside the fracture. Understanding the relationship between rock properties and permeability in fractures that undergo shear translation is important to maintain flow in engineered subsurface systems.

Gouge creation in a fracture can reduce its permeability substantially, as illustrated by the core scale transmissivity measurements presented here. While this small-scale behavior is significant, the permeability reduction does not reduce the permeability as low as the surrounding rock matrix. The decrease in the ability for a fluid to migrate through fractures with appreciable gouge formation will alter flow pathways significantly and reduce production rates through fracture networks.

Recent examinations of shear fracture creation using novel imaging techniques have been described in the literature. Work presented by Frash and Welch has used a Computed Tomography (CT) and shearing device to examine the nature and permeability of shales sheared under in-situ conditions (Welch et al. 2019, Frash et al. 2019). Frash et al. 2019 identified the generation of *en echelon*, or staggered fractures, as a common fracture generation property during shear fracture generation. Buckman et al. (2019) described the generation of shear induced fractures in small shale samples and has used a combination of scanning electron microscopy, CT, and numerical simulation to illustrate the combined dilating and constricting nature of fractures in shale created under shear. The complex nature of fractures created in shear was shown to have high and low capillary resistances, while maintaining high permeabilities (Tudisco et al. 2019). Our work differs in several aspects. As described in the following section, our samples are pre-fractured using a modified Brazilian technique prior to shearing the fractures. Full three-dimensional images of the fractures are obtained after discrete step-wise shearing, and a stable permeability is measured through the samples after each shearing event. Our focus is to understand the impact of additional shearing on the fracture structures, and how that impacts fluid migration through these fractures.

We present recent examples of observed fracture shearing behavior in two different samples: a homogenous Marcellus Shale and a heterogeneous Eau Claire shale/sandstone. These tests provide a visualization of the behavior we are observing in a larger suite of experiments. Further experiments on additional samples and under various conditions will be performed to more thoroughly examine this phenomenon, but the observations described here provide evidence of variation in gouge formation during

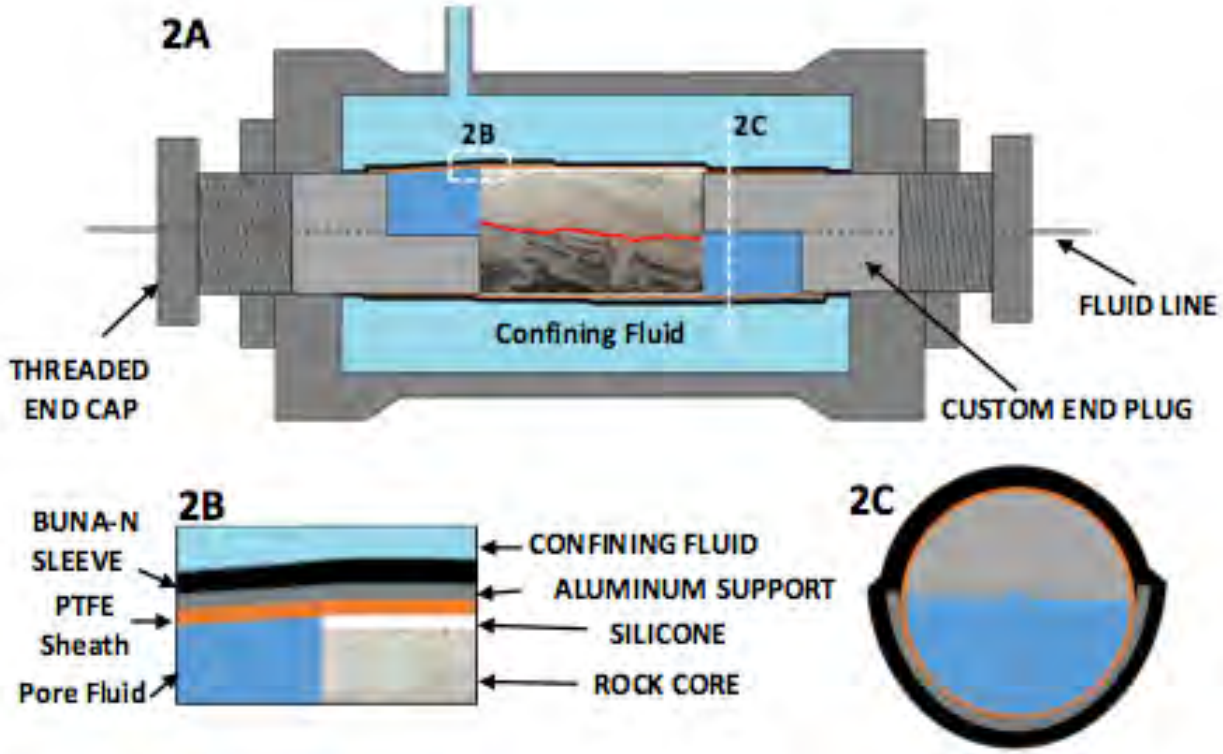

Figure 1. A) Modified Hassler style core holder designed for shearing of geomaterials. The threaded end caps are not fully seated and allow for motion, expressed as shear here, while the geomaterial is under a confining load. B) Close up of the sleeve and shield system that is placed around the core to prevent fluid bypass and keep the sleeves from collapsing. C) View parallel with long dimension of core holder showing configuration of aluminum supports. Figure is not to scale and exaggerated to illustrate small scale detail. Modified from Moore et al. 2018.

fracture shearing, and the importance of understanding this behavior when describing fracture permeabilities in stimulated reservoirs.

Experimental Apparatus and Materials

The experimental apparatus consists of an aluminum Hassler-style core holder installed within a Northstar Imaging Inc. M-5000 industrial CT scanner (Crandall et al. 2017, Moore et al. 2018, Gill et al. 2019). The shearing design is non-trivial, required significant modifications to the traditional core holder, and the operational procedure (Figures 1 and 2). The core-holder was modified to enable translation between two core halves using custom machined (half moon shaped) aluminum end plugs. A 3.8 cm diameter sample is fractured using a modified Brazilian technique (Moore et al. 2018), placed into the core holder apparatus, and the end plugs are inserted. The end caps of the core holder are then manually threaded into the body of the core holder until flush with the machined aluminum plugs. The system is placed vertically in the CT scanner, connected to fluid distribution lines, and CT scanned. After initial CT characterization, the top end cap is threaded downward to force the custom-made piston to push against one half of the core. The core is then forced to slide over the opposing end plug. As with most core flow studies using a Hassler style core holder, a rubber membrane (Buna-N) was used as the isolating material between the confining fluid and sample. However, the gap between the half-moons causes the membrane to collapse under elevated confining pressures. Mitigation of this required the implementation of aluminum shields, which propped the membrane open but also allowed translation of overburden forces to the core. Flow bypass around the supports was prevented by introduction of RTV silicone and shrink wrap PTFE on the perimeter of the core. (For full details on experimental design please see Moore et al. (2018)).

The CT data was collected at a resolution of 26.8 and 27.3 mm for the Marcellus and Eau Claire Shale samples, respectively. Reconstructed images were exported as 16-bit tiff files. The image stacks were segmented into the constituents of interest which included the fracture, lithological components (sandstone, shale), and heavier minerals using *ilastik* where appropriate (Sommer et al. 2011). Gouge material was not isolated during this process since the CT signature of this material was identical to the surrounding rock. Further image analysis was completed using ImageJ (Rasband, 2019).

Figure 2. Aluminum Hassler style core holder mounted inside of M-5000 CT scanner.

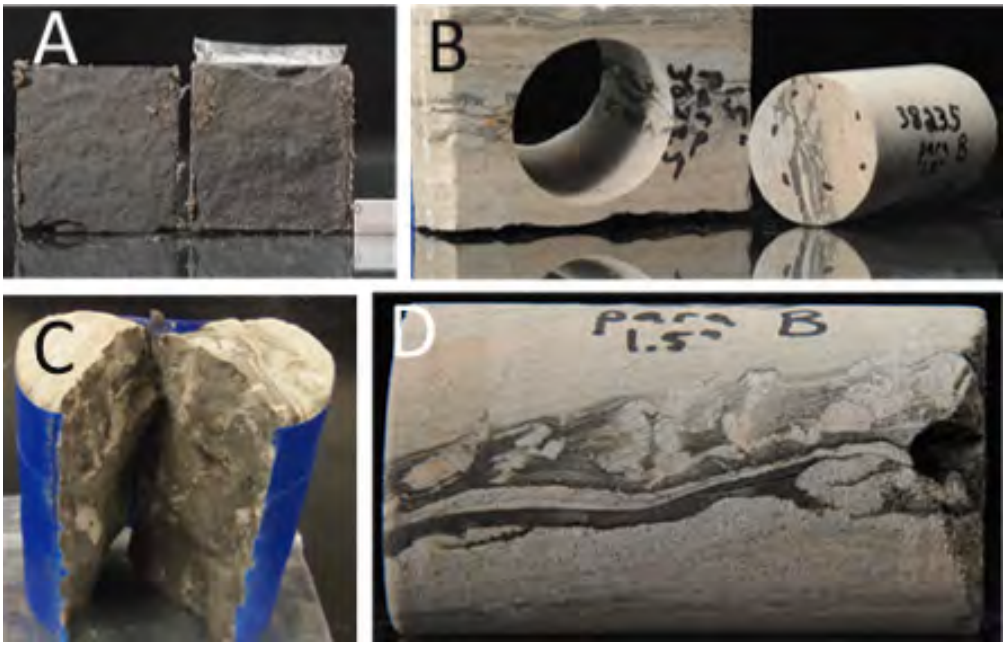

Figure 3. A) Fractured Marcellus sample, B) Eau Claire prior to shearing with parent material, C) fractured Eau Claire Shale, and D) Eau Claire Shale sample before fracturing.

Procedure

Two samples, a Marcellus Shale and an Eau Claire Shale (Figure 3), were cored at a diameter of 3.8 cm with a nominal length of <5 cm. Samples were then fractured using the Brazilian fracturing technique to produce an irregular, roughly planar fracture. Samples were mated together to create a tight fracture pairing and loaded into the core holder system as previously described. Confining pressure was applied at 6.89 and 21.37 MPa for the Marcellus Shale and Eau Claire Shale, respectively, using deionized water. Internal pore pressure was set to a base-line of 0.07 and 0.69 MPa for the Marcellus Shale and Eau Claire Shale, respectively, using a 0.5M NaCl brine (Crandall et al. 2017). These pressures resulted in an effective confinement stress of 6.82 and 20.68 MPa for the Marcellus Shale and Eau Claire Shale, respectively.

Shearing was done in sequential steps, with each step resulting in 0.8 mm of applied displacement; this measured displacement was not always 1:1 indicative of stress accumulation. At each step, brine was injected at varying flow rates, with the differential pressure (ΔP) across the core recorded by Rosemount 3051CD pressure transducers (span of 2.06 MPa and an accuracy of +827 Pa). The ΔP was used to determine transmissivity (T) by the following equation:

$$T = kA = Q\mu L/\Delta P$$

where A is the area of the core in m^2, k is the permeability in m^2, Q is the volumetric flow rate in m^3s^{-1}, μ is the dynamic viscosity in Pa*s, L is the length in meters, ΔP is the differential pressure in Pa, v is the fluid flow velocity in m^*s^{-1}. T was used in favor of k to describe fracture flow characteristics because it negates the need to determine precise fracture area, which was highly variable, and an appreciable flow in the tight matrix material was unlikely. A CT scan was also completed for each shear step to capture changes in geometry and directly measure displacement.

Observations

A central-cross sectional view of the CT scans reveals that the principal fracture in the Marcellus sample (Figure 4, top) is dominated by extensive zones of fracture dilation, as well as smaller, localized zones of closure, where rough asperities abut on the opposing fracture wall. The initial fracture is naturally rough, but overwhelmingly planar, following the sample bedding planes. In contrast, a more complex fracture

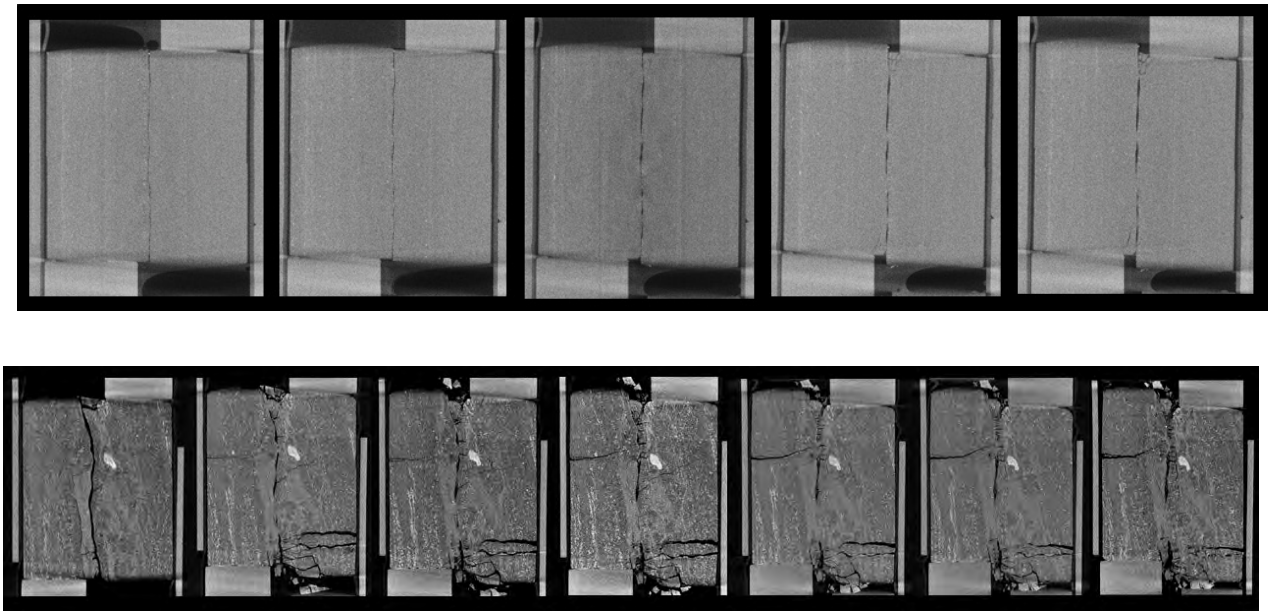

Figure 4. CT scans of unsheared Marcellus Shale (top) and Eau Claire Shale (bottom) core, followed by steps of fracture evolution due to shear.

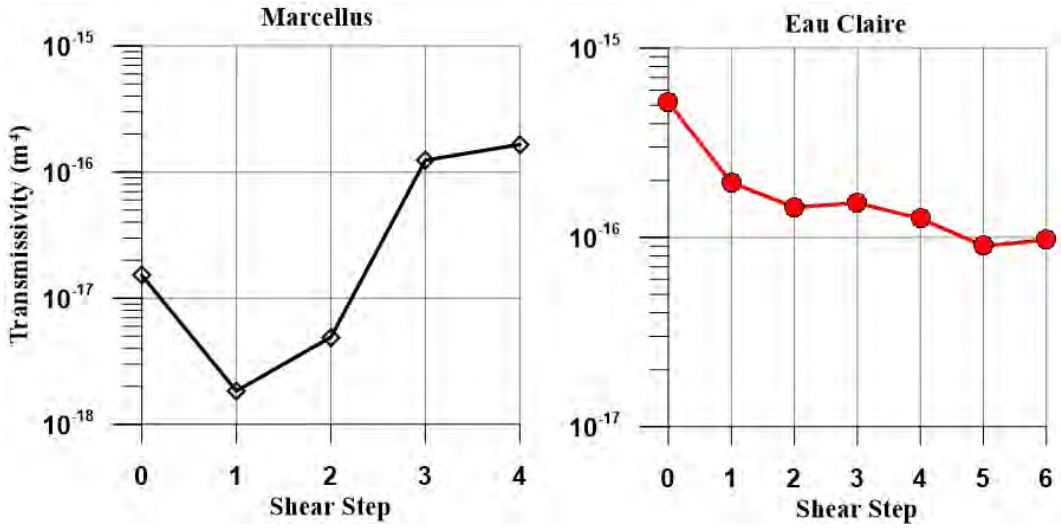

Figure 5. Transmissivity of the Marcellus Shale (left) and Eau Claire Shale (right) samples as a function of shear step.

evolution emerges from the analysis of Eau Claire Shale sample CT scans (Figure 4, bottom). While the initial fracture also follows a bedding plane, bedding planes in the Eau Claire Shale are complex and distorted by soft sediment deformation and bioturbation, and consequently, the fracture has a higher degree of roughness than that found in the Marcellus Shale. As with the Marcellus Shale, the fracture in the Eau Claire Shale core shows zones of dilation as asperities prop it open with increasing shearing. However, we see gouge development begin with shearing step two, and by the final shear step six, the fracture is dominated by accumulations of fine-grained rubble and gouge.

Transmissivity (T) measures observations of fracture evolution that are largely representative of the entire fracture. The fractured Marcellus Shale (Figure 5, left) experiences an initial drop in T with the initiation of shear, likely due to an imperfectly mated initial fracture, but then begins to increase with each successive shearing step, as the fracture begins to dilate. The mean fracture aperture (Figure 6, left) in the Marcellus Shale sample experiences a steady increase, rising from 64 mm prior to shearing to 164 mm after shear step four.

Conversely, during the fracture evolution in the Eau Claire Shale we see a steadily declining T despite the

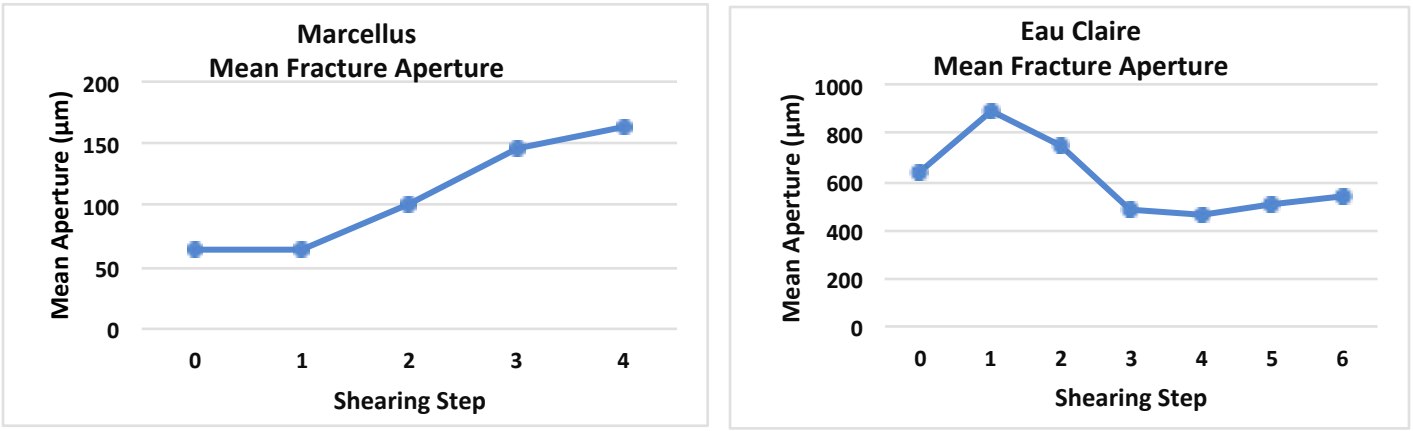

Figure 6. CT scans of unsheared Marcellus Shale (top) and Eau Claire Shale (bottom) core, followed by steps of fracture evolution due to shear.

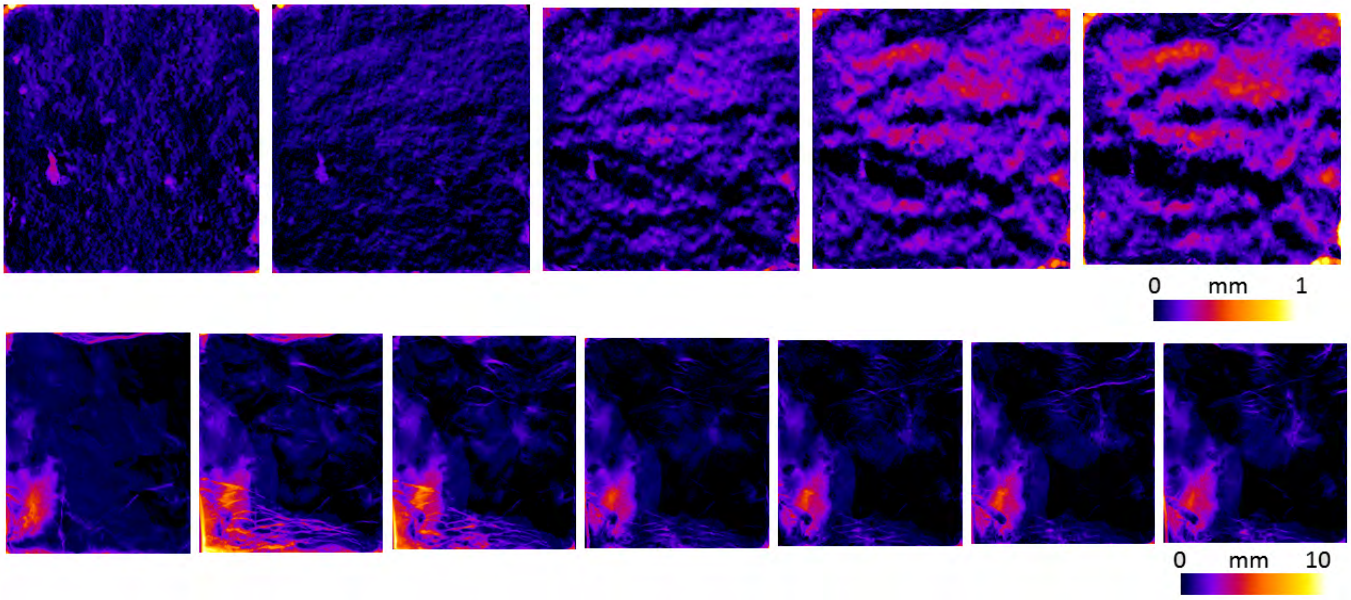

Figure 7. Aperture maps of Marcellus (top) and Eau Claire (bottom) Shales. (Note different scales for each fracture, with the Marcellus fracture tighter overall).

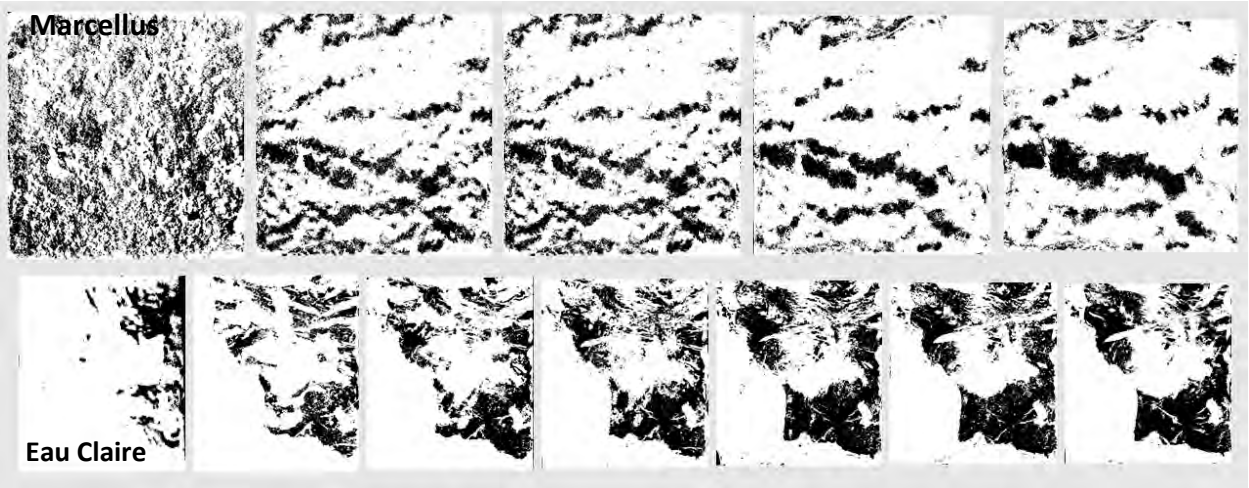

Figure 8. No-flow areas of aperture maps of Marcellus (top) and Eau Claire (bottom) Shales are shown in black.

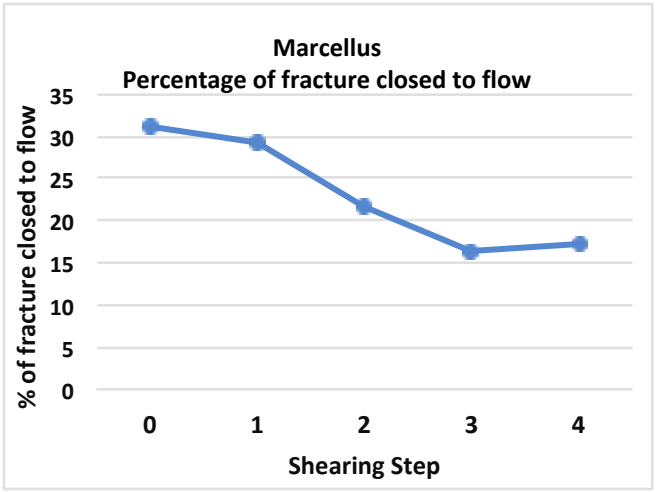

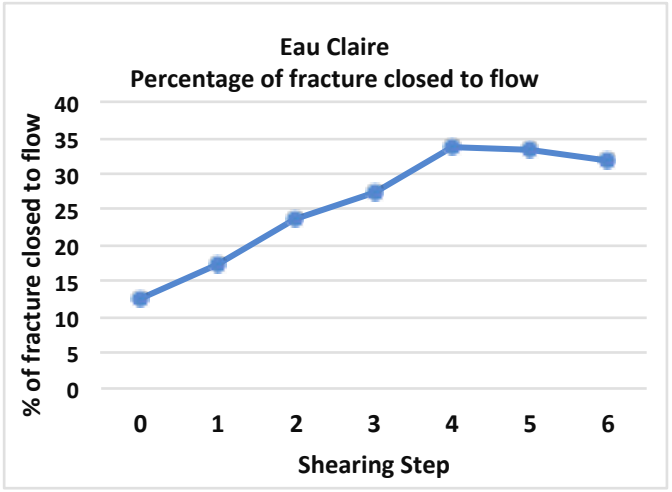

Figure 9. Percentage of fracture occupied by no-flow areas during successive scans of Marcellus Shale (left) and Eau Claire Shale (right).

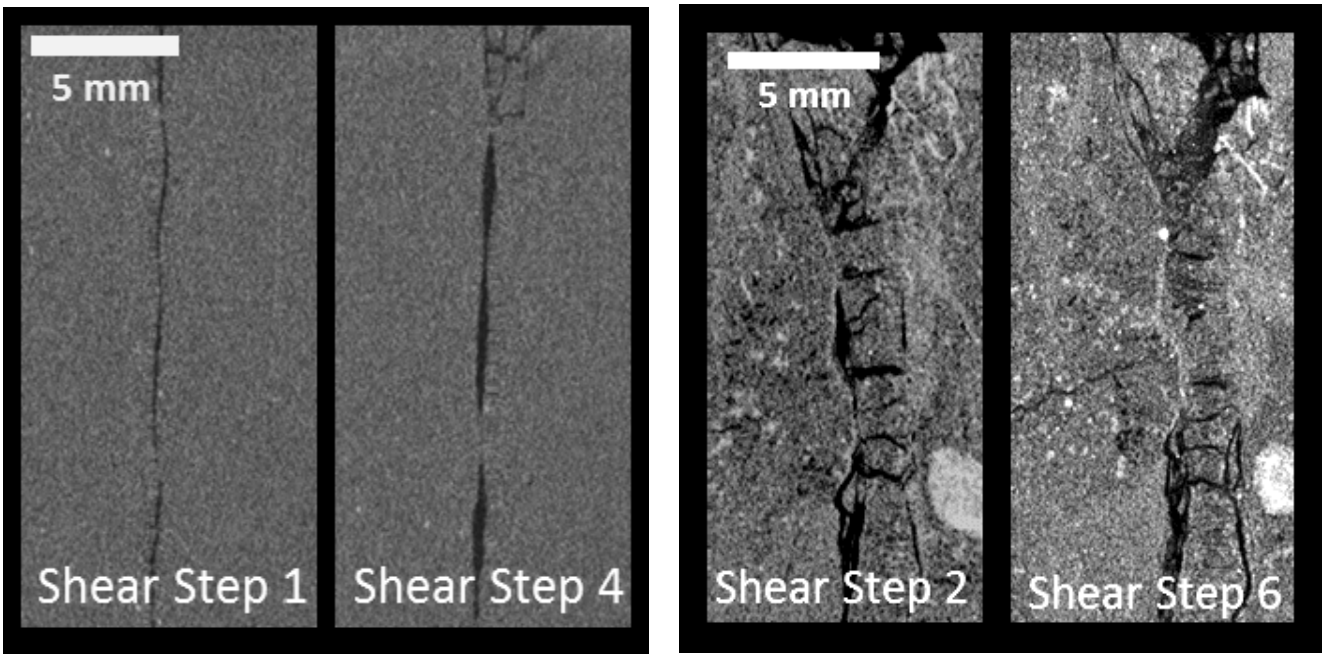

Figure 10. Detailed CT scans showing the open fracture in the Marcellus Shale (left) and the gouge-clogged fracture in the Eau Claire Shale (right).

presence of dilation zones (Figure 5, right), as gouge dominates the fracture and limits flow from the early stages of shearing. Mean aperture (Figure 6, right) experiences a slight initial rise with the onset of shearing in step one, but then declines rapidly by over 400 mm over the course of shearing steps 2 and 3. Mean aperture then remains fairly constant, as gains in aperture though dilation are offset by the increasing amount of gouge with further shearing.

Aperture maps of Marcellus Shale (Figure 7, top) likewise show zones of dilation in brighter shades, interspersed with low-flow and no-flow zones in dark purple and black where fracture apertures constrict to levels below the detection limit of the CT scans. No-flow zones, where no aperture was identified, were extracted (Figure 8, top) to gain an understanding of gouge accumulation throughout the fracture plane. No-flow zones in the Marcellus Shale fracture undergo a reorganization during shearing, conglomerating around areas where asperities abut on opposing fracture walls. While some minor damage to asperities is evident in CT scans, the amount of gouge creation is limited, and the percentage of the fracture occupied by no-flow areas decreases during the experiment (Figure 9), with the fracture experiencing an overall dilation.

The Eau Claire Shale presents a very different picture: zones of no flow are initially concentrated to one side of the fracture (Figure 8, bottom), but during shearing their size and extent grows rapidly as gouge begins to

clog the fracture, spanning almost the entire width of the fracture by the final shear step. The overall percentage of fracture that is closed to flow increases until it stabilizes at around one third of the fracture area in shearing step four. A detailed look at CT scan data (Figure 10) shows that in the Eau Claire core the disparate lithologies interact during shear such that the thin layers of weaker material fail. The resulting gouge accumulation plays a clear role in liming T in the Eau Claire Shale core.

Discussion

As discussed in Crandall et al. (2019) elemental analysis of this Eau Claire Shale sample revealed fairly high levels of calcium (Ca). It is hypothesized that this is related to calcite in the sample that manifests in zones of higher strength along certain regions of the core. Unpublished results indicate the additional presence of Fe oxide cements that create a similar material property difference between regions of the rock. Regardless of the minerals responsible, regions of high and low strength within the Eau Claire Shale do not have parallels in the homogeneous Marcellus shale sample presented. No gouge was observed in the Marcellus Shale sample and as the fracture dilates fracture transmissivity increases. The gouge creation in the heterogeneous sheared Eau Claire Shale sample offsets the fracture dilation and reduces the ability for fluids to flow freely through the bulk fracture.

While there is a difference between the effective overburden used in both experiments, ongoing research using the same effective stress and these sample types illustrates consistent behavior (Crandall, et al. 2019). These examples were used because the image fidelity was such that the asperities and gouge were easily resolved to explain the observed flow behavior. Further experiments on additional samples and under various conditions will be performed to more thoroughly examine this phenomenon, but the observations described here provide evidence of variation in gouge formation during fracture shearing, and the importance of understanding this behavior when describing fracture permeabilities in stimulated reservoirs.

Acknowledgement

The authors thank Bryan Tennant for outstanding laboratory effort and Alexandra Hakala and Grant Bromhal on research guidance in making this work possible.

References

Buckman, J, Couples, G, Lewis, H 2019. Textural characteristics of shale deformations, and associated distribution models: Implications for shale reservoir fluid flow, presented at the Unconventional Resources Technology Conference, Denver, Colorado, USA, 22-24 July 2019, DOI 10.15530/urtec-2019-591

Crandall, D, Gill, M, Moore, J, Brown, S, Mackey, P 2019. The influence of micro-fabric heterogeneity on sheared rock properties, presented at the Unconventional Resources Technology Conference, Denver, Colorado, USA, 22-24 July 2019, DOI 10.15530/urtec-2019-926

Crandall, D, Moore, J, Gill, M, Stadelman, M 2017. CT scanning and flow measurements of shale fractures after multiple shearing events, Int J Rock Mech Mining Sci. 100, 177-187. doi: 10.1016/j.ijrmms.2017.10.016

Frash, LP., Carey, JW, Welch, NJ 2019. Scalable en echelon shear-fracture aperture-roughness mechanism: Theory, validation, and implications. J. Geophys. Res. Solid Earth. https://doi.org/10.1029/2018JB016525

Gill, M, Moore, J, Brown, S, Mackey, P, Tennant, B, Crandall, D 2019. Complex influences on the behavior of sheared Eau Claire formation: insights from computed tomography, ARMA 19-1785, 23-26 June, New York, NY

Moore, J, Crandall, D, Gill, M, Brown, S, Tennant, B 2018. Design and implementation of a shearing apparatus for the experimental study of shear displacements in rock, Rev. Sci. Instrum.¸ 89(045107), doi:10.1063/1.5018419

Sommer, C, Strähle, C, Köthe, U, Hamprecht, FA 2011. ilastik: Interactive Learning and Segmentation Toolkit. In Proceedings of the Eighth IEEE International Symposium on Biomedical Imaging (ISBI), 230-233.

Rasband, WS 2019. ImageJ, U. S. National Institutes of Health, Bethesda, Maryland, USA, ttps://imagej.nih.gov/ij/.

Tudisco, E, Etxegarai, M, Hall, S, Charalampidou, EM, Couples, GD, Kardjilov, N 2019. Fast 4D imaging of fluid flow in rock by high-speed neutron tomography. J. Geophys. Res. Solid Earth. doi.org/10.1029/2018JB016522

Welch, NJ, Frash, LP, Menefee, AH, Carey, JW 2019. Triaxial direct shear fractured Marcellus (MSEEL) shale – Peak and residual shear strength, permeability, and hydroshear potential, presented at the Unconventional Resources Technology Conference, Denver, Colorado, USA, 22-24 July 2019, DOI 10.15530/urtec-2019-435